Polaritons in micropillars: from single-photon phase shift to spin-orbit interaction in photonic graphene

MR TOBY JOHN DOWLING

A thesis presented for the degree of
Doctor of Philosophy

Department of Physics and Astronomy
The University of Sheffield
United Kingdom
April, 2022

Abstract

Microcavities based on gallium arsenide are experimentally investigated and analysed, with polaritons in single and honeycomb micropillar geometries.

First, the single micropillar polariton energy structure is analysed. A pillar is selected with appropriate energy and phase matching conditions that satisfy parametric scattering. Parametric scattering is attempted but is not successful in our device. Pump-probe laser excitation is used to seed a final state population in the parametric scattering signal state. With appropriate incident power, stimulated scattering is seen in the idler polariton mode. The parametric blockade was the motivation for using the single micropillar device. The photon statistics of the central polariton mode were analysed, no evidence of anti-bunching was found.

The next part of this thesis uses two separate micropillar devices and explores the phase imprinted from one polariton mode onto another. The size of the phase shift is measured using a sensitive polarisation detection basis. The two devices have different exciton fractions in their respective modes, which changes the predicted and experimental phase shift, with the most significant phase value per polariton found to be 3mrad.

Finally, polaritons are confined within a period array of micropillars. The photoluminescence spectra from a honeycomb lattice have a TE-TM field akin to Dresselhaus spin-orbit coupling around the Dirac points. The pseudospin for polaritons found in non-resonant excitation is confirmed by resonantly exciting at the Dirac point energies in the S-band and P-band. The optical spin-Hall effect shows that the pseudospin pattern has two clear domains in the recorded real-space spectra.

“*Life is for living and not for practice, act on your instincts.*” ∼ *W.J.D*

List of Publications

“**Optical analogue of Dresselhaus spin-orbit interaction in photonic graphene**”, C. E. Whittaker, T. Dowling, A. V. Nalitov, A. V. Yulin, B. Royall, E. Clarke, M. S. Skolnick, I. A. Shelykh and D. N. Krizhanovskii. Nat. Photonics 15, 193-196 (2021)

“**Few-photon all-optical phase rotation in a quantum-well micropillar cavity**”, T. Kuriakose, P. M. Walker, T. Dowling, O. Kyriienko, I. A. Shelykh, P. St-Jean, N. C. Zambon, A. Lemaître, I. Sagnes, L. Legratiet, A. Harouri, S. Ravets, M. S. Skolnick, A. Amo, J. Bloch, D. N. Krizhanovskii. Nat. Photon. (2022)

Presentations

“**Observation of the optical spin Hall effect in photonic graphene**”, ICSCE10: 10. International Conference on Spontaneous Coherence in Excitonic Systems; Melbourne, VIC (Australia); 28-31 Jan 2020.

Acknowledgements

I want to express my deepest gratitude to my supervisor Prof. Dmitry Krizhanovskii, for allowing me to conduct research at the University of Sheffield and for his guidance and support during my PhD. I would also like to thank Prof. Maurice Skolnick, whose work ethic and dedication to the LDSD group is inspiring.

I express my sincere thanks to Dr. Paul Walker, who has been a source of knowledge over all aspects of my studies. I want to thank Dr. Charles Whittaker for introducing me to the lab and collaborating on experiments. Thanking also Dr. Tintu Kuriakose, the long evenings of measurements were as stressful as they were enjoyable, and I could not have asked for a better person to work with. Thank you also to Ivan Solevov, who taught me so many valuable things at the start of my PhD. Thank you to Lucy, Ruggero and Davide, who were always a supply of motivation during our long days in the lab. A special thank you to Prof. Rhoda Hawkins, who provided terrific support towards the end of my studies.

To my friends, Mr. Dr. Mahmoud, Joe, Jaz, George, Chris, Sajad, Russell, Will, Flo, Alex, Yusef, Sammy and Carys, who all supported and motivated me during different times of my PhD.

Finally, to my Dad, Mum, Aunts, Nan and Brother, whom without I would not have made it so far.

Contents

Chapter 1

Background

1.1 Introduction

Microcavity polaritons have shown novel analogue physics and the potential for far-reaching industrial application. The half-light half-matter quasiparticles allow numerous phenomena to be investigated, including Bose-Einstein condensation, superfluidity, topologically protected states, and emerging quantum effects. Since their discovery in 1992, the landscape of semiconductor technology has changed significantly. Growth technology and the etching of structures have allowed polaritons to be investigated in several new ways, improving the quality of existing effects and introducing newer research fields. All polariton effects investigated within this thesis will use III-V semiconductors, with devices using alloys of GaAs. Research is not limited to one material, with many past novel results first demonstrated on CdTd-based devices. Currently, GaAs-based devices allow for the highest control in the fabrication process.

The first chapter introduces the basic concepts of semiconductor microcavities, with particular focus on GaAs. Planar microcavities are introduced along with how the exciton and photons modes strongly couple, forming exciton-polaritons. Then the following novel phenomena in current polariton research are reviewed; *Bose-Einstein condensation*, *superfluidity*, *topological polaritons* and *polariton blockade* approaches. Polaritons' photonic and excitonic properties are described, giving physical insight into why certain phenomena are relatively straightforward to achieve compared to alternative solid-state systems.

The second chapter explains the sample fabrication process for the microcavity used in this thesis. The etching process for micropillars, along with the experimental details of non-resonant excitation and resonant transmission. Polaritons are imaged in the near and far-field, schematically showing the basic principles. The experimental details of turning a continuous wave laser into a pulsing laser is shown. The use of an electro-optical modulator allows for ultra-fast and controllable polarisation rotation of an incident laser on the device. Finally, the polarisation metrics used to describe the state of the polaritons inside the microcavity are shown, with tomographic scans showing the complete spatial profile of square polariton micropillars.

In the third chapter, a study into the parametric scattering of polaritons in a single micropillar structure is attempted. Pump-probe excitation is used to enhance scattering from the pump polariton state into the signal and idler modes. The photon statistics leaving the pump state are measured on an Hanbury-Brown and Twiss interferometer, attempting to see weak anti-bunching, as predicted by the Liew et al. [1] proposal. No quantum behaviour was observed, but the experimental design can be used to observe these effects on future devices.

The fourth chapter again uses single micropillar devices. Using pump-probe laser excitation on the two lowest excited states of the pillar, we study the phase shift imprinted from the lowest mode onto the upper mode; this is done by the process of *cross-phase modulation* (XPM). The experiment is performed in two configurations: 1) pulsed and continuous laser, and 2) using two pulsed lasers. Configuration 2 pulsed lasers allowed us to see phase shift as a function of the arrival time of the two lasers. We built up a convincing set of results on two separate devices with two different exciton fractions, showing that a larger exciton fraction provided larger phase shift values. A theoretical framework is put forward to understand why the mode's phase shift occurs and when we can expect it to be the largest. With the results also presented in Kuriakose et al. [2]

The fifth chapter looks at micropillars arranged in a honeycomb lattice geometry, which is an analogues to graphene. Polariton graphene has been used to reproduce similar bandstructure properties of electronic graphene. Using this system, we investigated the polariton polarisation around the Dirac points in the S- and P-bands. The direction of polarisation depends on the TE-TM field, which is revealed through the optical spin-Hall effect, where a Dresselhaus-like polarisation texture is seen at the $\mathbf{K}$ and $\mathbf{K}'$ points in the S-band and P-band. This feature was predicted by Nalitov et al. [3], and we were able to reproduce the results experimentally. The chapter is presented in paper format, refer to Whittaker et al. [4], ***Reproduced with permission from Springer Nature.***

1.2 Semiconductor microcavity

This section introduces the background physics of exciton-polaritons, introducing microcavity structures based on III-V semiconductors, with discussions on how light is confined in these devices.

1.2.1 Semiconductor band structure

An element such as galium has a periodic spatial arrangement of atoms, where unit cells fill all the available space in the crystal [5]. By incorporating arsenide, the crystal structure becomes a zincblende. A helpful way to look at the structure of semiconductors is reciprocal space, mapping the Brillouin zones of crystalline solids. The energy-momentum is the bandstructure, with different semiconductor materials having different features. GaAs is a direct band-gap semiconductor, being 1.42eV [6]. The minimum energy transition between the valence and conduction band takes place at the same momentum point in the Brillouin zone, shown in figure 1.1. Note that this if for an unstrained structure; therefore, there is energy degeneracy for the heavy and light hole valance band at $k = 0$. Introducing strain through tensile/compression will change the bandstructure, where the energy of the light and heavy hole bands change - lifting the degeneracy at $k = 0$.

In contrast, indirect materials like Silicon (Si) have indirect band gaps, which rely on phonon-assisted scattering to satisfy energy and momentum.

Alloying two semiconductors like GaAs and InAs (E_G=0.43eV) allows for control over the band-gap size. The contribution of each element $\mathrm{In}_x\mathrm{Ga}_{1-x}\mathrm{As}$, where $0 \leq x \leq 1$. The choice of material is essential; materials with a sizeable difference in lattice constant induce strain at the boundary between the materials.

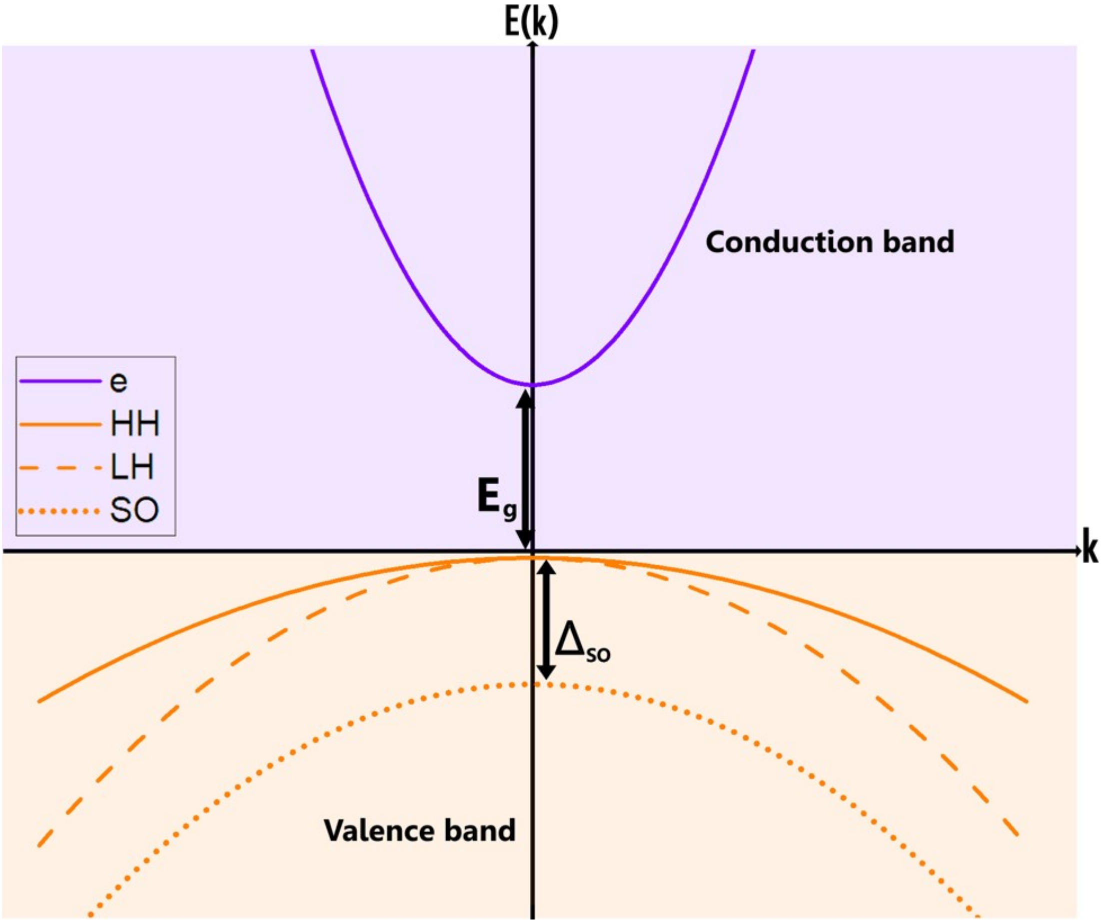

Figure 1.1: A zincblended unstrained semiconductor. The conduction and valence balance have a minimum energy separation E_g. The heavy hole (HH) and light hole (LH) bands have different masses. The split-off band (SO) lies below the valence band.

1.2.2 Semiconductor quantum wells

Prior to 1970, control over the bandgap energy relied on the aforementioned alloys. The invention of using heterostructure designs of semiconductors by Esaki and Tsu brought forward possibilities for designing new devices for industry and research [6].

Quantum Wells (QWs) exploit quantising a dimension of motion, the growth axis. The quantisation effects arise when the thickness of layers is similar to the de Broglie wavelength (λ_B) of the electron (or hole). Working from the Heisenberg uncertainty principle and kinetic energy of a free particle, the inequality can be derived:

$$E_{con} \sim \frac{\hbar^2}{2m(\Delta z)^2} > \frac{1}{2}k_BT, \tag{1.1}$$

rearranging to get the thickness of the QW Δz,

$$\Delta z \sim \sqrt{\frac{\hbar^2}{mk_BT}}. \tag{1.2}$$

Where E_{con} is the energy confinement in the z-direction, m is the mass of the particle, k_B is Boltzmann's constant, $\hbar$ is the reduced planks constant, and T is temperature. The layer structure of a GaAs/AlGaAs QW and the energy profile are displayed in figure 1.2.

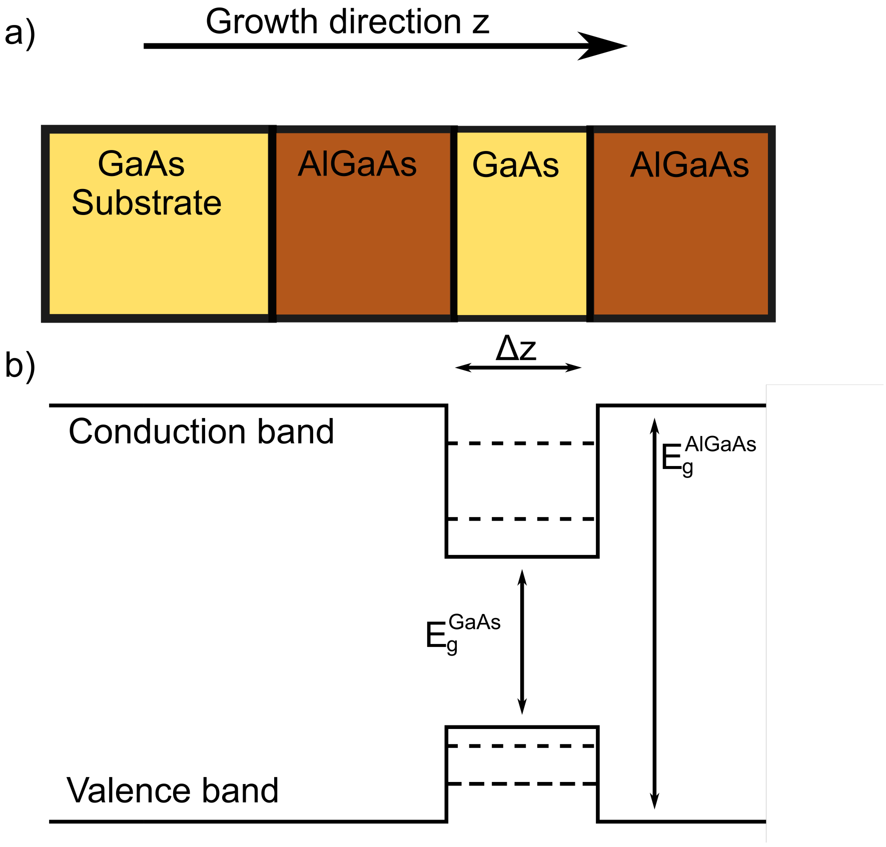

Figure 1.2: Heterostructure of AlGaAs/GaAs. a, the layer structure of a GaAs/AlGaAs QW. b, the energy profile of bands along with the formation of intersubbands of the QW.

Structures are grown via molecular beam epitaxy (MBE) or metal-organic chemical vapour deposition (MOCVD). These techniques allow for control with layer-by-layer atomic precision; the wafers used in this thesis were grown by MBE. Electrons of GaAs are trapped by the potential of the AlGaAs conduction band, while the valence band of the AlGaAs traps the hole. The particles are trapped in the z-direction but can move freely in the x-y plane.

1.2.3 Excitons

When an interband transition occurs in a semiconductor due to photon absorption, the excitation forms an electron-hole pair (e-h pair). The hole has an opposite charge, arising from the same position the electron occupies. The electron is excited from the valence to the conduction band in the semiconductor. The bound state of the e-h pair is called an *exciton*, a quasi-particle that has binding energy given by:

$$E(n) = -\frac{\mu R_H}{m_o \varepsilon_r^2 n^2}, \tag{1.3}$$

and radii $r(n)$

$$r(n) = \frac{m_o}{\mu} \varepsilon_r n^2 a_H. \tag{1.4}$$

Where R_H is the Rydberg constant for hydrogen, m_o is the electron rest mass, ε_r is the dielectric constant, n is the principal quantum number, μ the reduced mass of the exciton and a_H the Hydrogen Bohr radius.

The two types of excitons are Wannier-Mott and Frenkel excitons, characterised by localisation over the lattice of atoms in the semiconductor. Wannier-Mott excitons are delocalised, while Frenkel excitons are tightly bound over a unit in the crystal. The excitons will remain bound if the binding energy is larger than the phonon energy at the given temperature. For experiments performed in this thesis, the temperature of the sample is cooled to ~4-10K. To overcome the thermal effects, the value $k_B T$ need only be less than the binding energy E_B. In GaN and ZnO, the binding energy is more significant, allowing excitons to form at room temperature.

When introducing QWs, the confinement reduces e-h pair separation and increases the binding energy, leading to a larger oscillator strength. The exciton absorption coefficient can be enhanced by making smaller well widths [7],:

$$A = \frac{4\pi^2 e^2 \hbar f}{n_r m_o c \Delta z}. \tag{1.5}$$

Where A is the absorption coefficient, e is the electron charge, f is the exciton oscillator strength, n_r is the refractive index, and c is the speed of light. Excitons in QWs (2D systems) have binding energies that are four times that of bulk semiconductors [8].

1.2.4 Microcavity

So far, the matter component has been discussed, with photons being the other ingredient in forming exciton-polaritons. Devices that confine light have been studied for over half a century. A Fabry-Perot cavity consists of two mirrors placed at a distance L_C apart, with both mirrors' reflectivity R and Transmission T coefficients being the same. The electric field coefficients take value r and t, so considering an initial source E_{in}, the transmission after the first mirror is tE_{in} ($R = |r|^2$, $T = |t|^2$). Defining now the round-trip phase of the resonator ϕ, the phase accumulated by the photon as it goes from mirror one to two and then back to one. ϕ takes the form:

$$\phi = \frac{2L}{\lambda}2\pi, \tag{1.6}$$

each round trip accumulates $e^{i\phi}$, so it follows that

$$\frac{E_{out}}{E_{in}} = t^2 e^{\frac{i\phi}{2}}(1 + r^2 e^{i\phi} + r^4 e^{2i\phi} + ...), \tag{1.7}$$

which can be simplified to

$$\frac{E_{out}}{E_{in}} = \frac{(1-R)e^{\frac{i\phi}{2}}}{1 - Re^{i\phi}}. \tag{1.8}$$

If the round trip path fits multiples of λ (wavelength), the transmission tends to 100%. The cavity size is grown to allow for maximum transmission. The light is confined between the two mirrors, with the successive reflections forming a standing wave.

Samples in this thesis use distributed Bragg reflector stacks (DBRs); the refractive index contrast between alloys such as AlGaAs and GaAs makes a highly reflective interface. The electric field maximum position depends on the amount of DBR stacks on either side of the cavity. The QW is positioned where this field is maximum, enabling the best light-matter coupling for polariton systems. The QW can be referred to as an emitter or active material when talking about the interaction with photons. The following section discusses the *Weak* and *Strong Coupling regimes.*

1.3 Light-matter interaction

This section will discuss the weak coupling and strong coupling regimes, with the latter looked at in more detail as it pertains to the results in this thesis.

1.3.1 Weak coupling

In the weak coupling between light and matter, the interaction between the active material and cavity mode is dominated by incoherent decay processes [9]. When the spontaneous emission energy is resonant with a cavity mode, the emission rate is enhanced into the optical mode. If these energies are out of resonance, the rates decrease [9]. When discussing the weak coupling regime, it is helpful to use figures of merits to describe the effect the cavity is having on the emitter; this merit is known as the *Purcell factor*. First, consider a point-source inside a single-mode cavity. A Lorentzian function describes the photonic density of states:

$$\rho_c = \frac{2}{\pi} \frac{\delta w_c}{4(w - w_c)^2 + \delta w_c^2}, \tag{1.9}$$

where w is the frequency, w_c is the cavity frequency, δw_c is the cavity linewidth.

By taking the ratio of spontaneous emission rates inside and outside a cavity:

$$F_P = \frac{3Q(\lambda_c/n)^3}{4\pi^2 V_{eff}}. \tag{1.10}$$

This is the *Purcell factor*, where Q is the quality factor of the cavity, n the refractive index, λ_c the cavity wavelength and V_{eff} the effective volume. A maximum Purcell enhancement is quantified by Q/V_{eff}. Active materials like quantum dots are embedded in photonic crystals (PCs) to modify the dots' optical properties, decreasing the mode volume and concentrating the electric field profile on regions of the device. The QD lifetime is reduced due to the mode overlap between the PC and the emitter [10]. *Slow light* is another feature exploited in the weak coupling regime, the velocity of light resonant with an emitter is reduced, which leads to stronger interactions [11].

1.3.2 Strong coupling

The weak coupling regime describes the relationship between the emitter and photon, where the probability of escaping the cavity is greater than being reabsorbed by the emitter.

The cavity and emitter hybridise in the strong coupling regime, forming two new eigenfrequencies different from the original modes, referred to as the upper and lower polariton branches. The system discussed in this thesis uses polaritons based on excitons and photons, with the new states called exciton-polaritons. For brevity, exciton-polaritons will be referred to as polaritons.

The Fabry-Perot microcavity system described previously has an optically active semiconductor layer positioned where the electric field is maximum, as illustrated in figure 1.3.

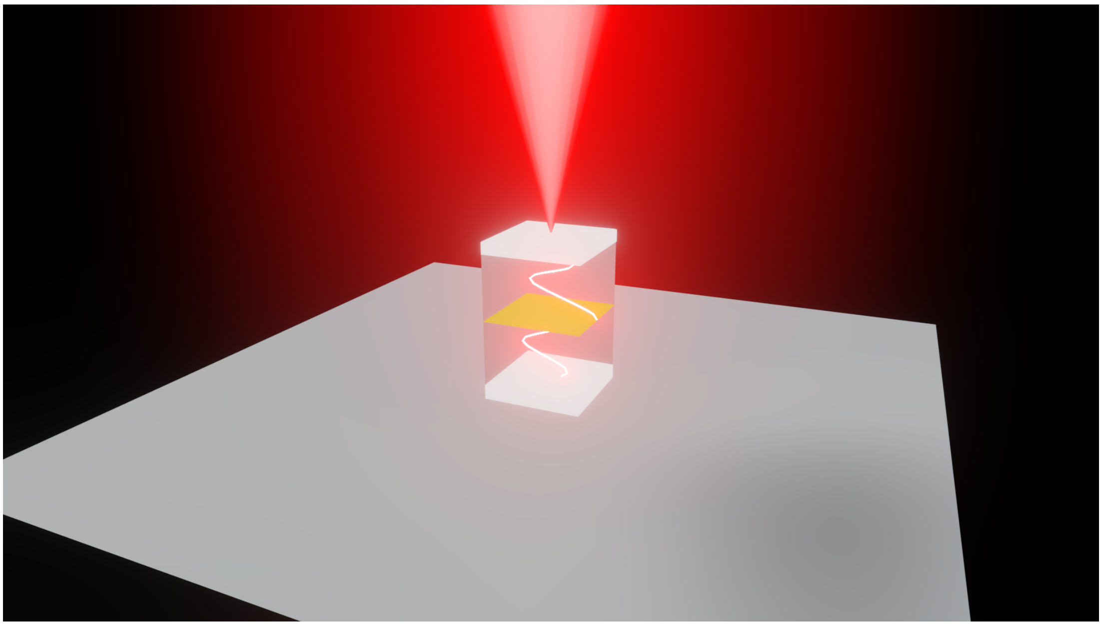

Figure 1.3: Illustration of light confined between two highly reflective surfaces. An optically active material placed at maximum field intensity.

The cavity resonance is modified by changing the mirror distance. When the separation is optimised to the exciton transition in the QW, the decay rate of the excitons can become the main scattering channel. The cavity selects a photon mode for the QW excitons to couple preferentially, in contrast to bulk semiconductors [12]. In the strong coupling regime, the vacuum Rabi-splitting separates the new eigenmodes. The splitting is observed in absorption and reflectivity measurements as a function of energy, resulting in an anti-crossing. This anti-crossing is shown in figure 1.4, taken from Weisbuch et al. (1992) [12].

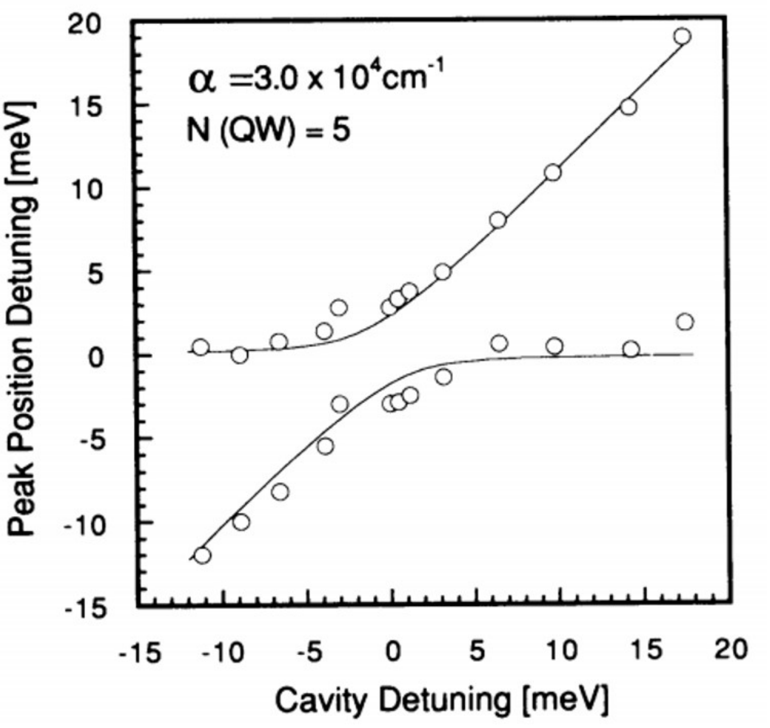

Figure 1.4: Anti-crossing between upper and lower polariton modes. Also referred to as the normal mode splitting observed in VCSEL Microcavity. Taken from ref. [12].

When considering a quantum well placed at the anti-node of the electric field, Ω_{Rabi} takes the form:

$$\hbar\Omega_{Rabi} = \sqrt{\frac{N_{QW}(\hbar e)^2}{2\epsilon m_0 L_{eff}} f_{osc}}. \tag{1.11}$$

Where N_{QW} is the number of QWs, e is the charge of an electron, ϵ is the permittivity of the cavity, L_{eff} is the effective length of the cavity after considering the penetration of light into the mirrors and f_{osc} is the oscillator strength of the QW[13]. Physically Ω_{Rabi} represents a coupling strength that is greater than the dissipation rates of the system, the energy is coherently exchanged between the emitter and cavity photon.

The equation below describe the eigenmodes of the upper and lower polariton branches:

$$E_{UP(k),LP(k)} = \frac{E_{ph(k)} + E_{X(k)}}{2} \pm \frac{1}{2}\sqrt{\Delta_k^2 + (\hbar\Omega_{Rabi})^2} \tag{1.12}$$

where $E_{ph(k)}$ and $E_{X(k)}$ are the photon and exciton energies for a given wavevector value and Δ_k is the detuning between the exciton and cavity mode, $\Delta_k = E_{ph(k)} - E_{X(k)}$. Equation 1.12 does not take into account the cavity or exciton lifetimes, γ_C is attributed to homogeneous broadening of the cavity mode, while γ_X is related to the inhomogeneous broadening of the exciton energy. When taking these broadening factors into account,

$$E_{ph(k)} \longrightarrow E_{ph(k)} + i\gamma_C,\ E_{X(k)} \longrightarrow E_{X(k)} + i\gamma_X. \tag{1.13}$$

Work by Savona et al. [14] details a rigorous treatment for calculating the Rabi-splitting, showing the conditions for strong and weak coupling. The splitting in absorption is given by:

$$\Omega_A = 2\sqrt{V^2 - \frac{1}{2}(\gamma_X^2 + \gamma_C^2)}, \tag{1.14}$$

where $V = \sqrt{2c\Gamma_0/(n_{cav}L_{eff})}$ and Γ_0 is the decay rate of the exciton amplitude in a single quantum well at $k_x = 0$ and n_{cav} is the cavity refractive index. When $V^2 > \frac{1}{2}(\gamma_X^2 + \gamma_C^2)$ the system is in the strong coupling regime, but when $V^2 < \frac{1}{2}(\gamma_X^2 + \gamma_C^2)$ it is in the weak coupling regime [9].

Equation 1.12 shows the eigenvalues for the upper and lower polariton branches, with polaritons being a mixture of the photon and exciton that strongly couple. To describe the contribution from the photon and exciton, the *Hopfield coefficients* are used, defined as:

$$|X(k_{||})|^2 = \frac{1}{2}(1 + \frac{\Delta_k}{\sqrt{\Delta_k^2 + 4\hbar^2\Omega_{Rabi}^2}}), \tag{1.15}$$

$$|C(k_{||})|^2 = \frac{1}{2}(1 - \frac{\Delta_k}{\sqrt{\Delta_k^2 + 4\hbar^2\Omega_{Rabi}^2}}). \tag{1.16}$$

Where $|X(k_{||})|^2 + |C(k_{||})|^2 = 1$, defining the the excitonic and photonic fraction of the polariton. Figure 1.5 shows a series of different exciton-photon detunings and how the Hopfield coefficients change for the respective polariton branches. The shape of the dispersions depends strongly on the detuning, which is readily seen in the three dispersion plots of figure 1.5. The upper polariton branch is strongly quadratic at positive detuning. In contrast, the lower branch is non-parabolic for all detunings—a more positive detuning results in a stronger excitonic fraction in the lower branch. The Hopfield coefficient values for both excitonic and photonic fractions become similar for a small in-plane wavevector value. As the lower branch goes to large $k_{||}$, polaritons become purely excitonic. The upper branch polaritons become mostly photonic at high $k_{||}$. Therefore, the exciton-photon coupling is effective over small $k_{||}$.

1.3.3 Microcavity materials

The microcavity materials used in this thesis are based on GaAs, AlGaAs and InGaAs alloys. A disadvantage of using microcavity based on III-V semiconductors is the light-matter coupling strength in the active material; because of this, the temperatures used are typically at the level of tens-of-kelvin. Many other materials are used to explore polaritons in microcavities.

The system leading room temperature polariton effects is Gallium Nitride (GaN), as discussed in Malpuech (2002)[15]; GaN excitons are stable at room temperature, the light-matter interaction is powerful with large Rabi-splittings observed [16]. Low threshold polariton lasing at room temperature was demonstrated by Christopoulos et al. [17]. Electrically pumped GaN polariton lasing has also been demonstrated [18] as well as conventional photon lasing.

A more recent system of interest are transition-metal dichalcogenides (TMDCs); these layered materials gained attention following the discovery of graphene. Much like GaN, TMDCs have tightly bound exciton states with binding energies reaching several hundred meV [19], and large oscillator strengths [20] enabling room temperature operations. Kerr-like nonlinearities have been studied [21].

Organic microcavities have realised the strong coupling regime [22], early results showed Rabi-splittings an order of magnitude larger than the inorganic counterpart. Typical Rabi-splittings observed in InGaAs QW structures at 5K give mode splittings typically around 3-5 meV [23]. In contrast, the first strong coupling result in the organic field was around 160meV, with an increased oscillator strength responsible for the more significant splitting. Polariton lasing has been observed in organic systems [24]. More recently, a room-temperature organic polariton transistor has been developed [25]. The device exploits a single step vibron-mediated channel to achieve a low condensation threshold. By seeding a population at $k_{||} = 0$ state with a control pulse, they were able to amplify the final state. Then, encoding the laser pulse sequences creates logical operations on the output signal.

Since the strong coupling of light and matter was demonstrated in microcavity polaritons, numerous phenomena have been observed: Bose-Einstein condensation [26], superfluidity [27], bright solitons [28], topological edge states in zero [29] and one dimensions [30] and evidence for polaritons as an antibunched source of light [31]. All of these effects exploit the light-matter nature of polaritons. The following section will discuss the polariton nonlinearity and how it gives rise to parametric scattering, amplification and bistability physics.

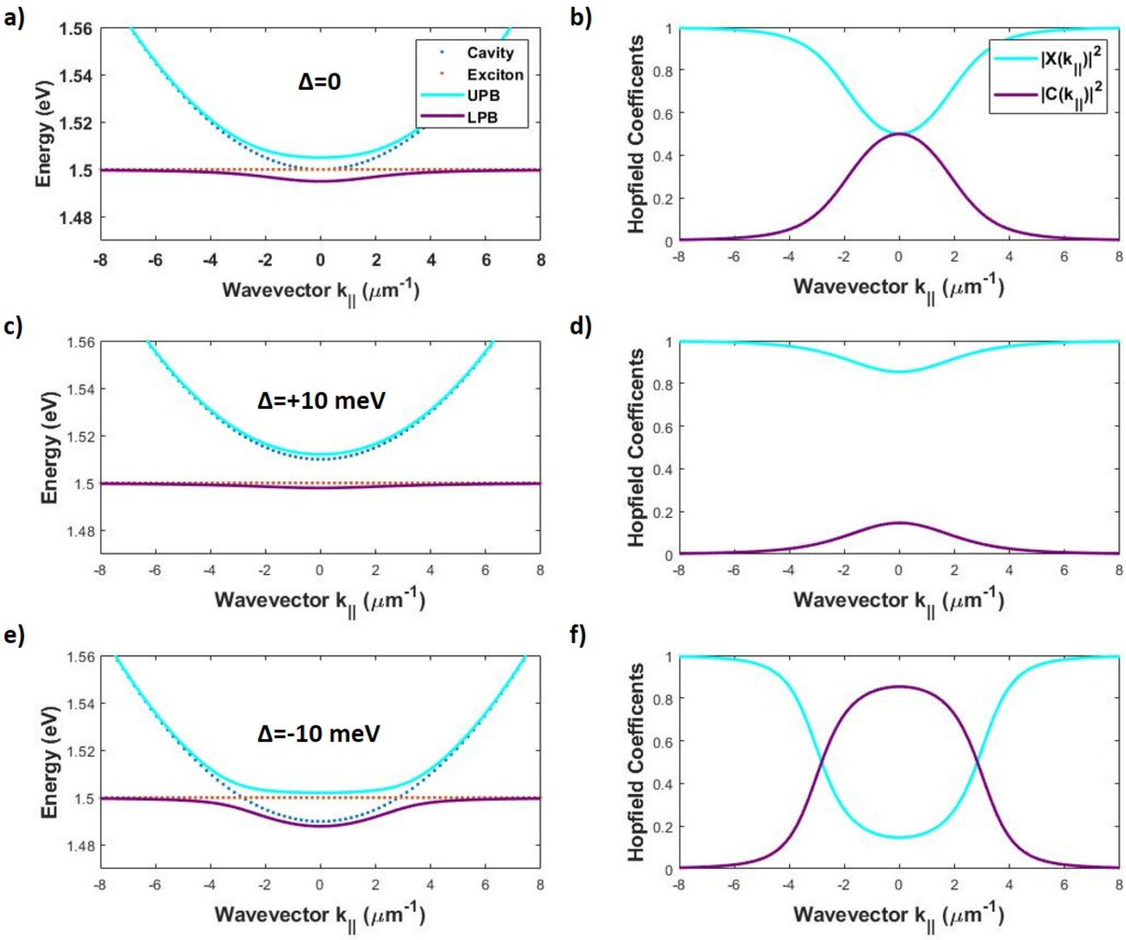

Figure 1.5: Dispersion of polariton branches for different exciton-photon detunings. Images of the left side (a, c, e) show branch energy vs wavevector at a) zero detuning $\Delta = 0$, c) positive $\Delta = +10$ meV and e) negative $\Delta = -10$ meV. Exciton and photon energies are shown as the dotted lines. The corresponding Hopfield coefficient lines are indicated in b ($\Delta = 0$ meV), d ($\Delta = +10$ meV) and f ($\Delta = -10$ meV).

1.4 Nonlinear polariton effects

1.4.1 Polariton-polariton interaction

Polariton-polariton interactions are mediated by their excitonic component; it is a Coulomb interaction and is strongly spin-dependent [32, 33]. For the same spin, the polariton-polariton interaction is repulsive. Tassone and Yamamoto [34] estimated the exciton-exciton interaction strength to be $g_X \sim 6E_B a_B^2$, where E_B is the exciton binding energy and a_B is the exciton Bohr radius. For GaAs, values of $g_X \sim 6\mu eV\mu m^2$ are expected for a_B ~10nm and E_B ~10meV [35]. One approach to estimate the polariton-polariton interaction strength is to monitor the blueshift of the polariton mode with increasing density [36]:

$$\Delta E = g_p \rho \tag{1.17}$$

Where ΔE is the energy change, ρ is the polariton density and g_p is the interaction strength for co-circularly polarised polaritons. Equation 1.17 is valid for polariton densities below Mott transition density [37]. Polaritons with opposite circular polarisation weakly attract, while linearly polarised polaritons repel approximately with the strength $\frac{1}{2}g_p$ [38, 39].

The polariton-polariton interaction is increased by reducing the mode volume, forcing closer proximity for the excitons [40], that is why 0D devices such as micropillars are an attractive platform. In micropillars, the interaction strength for co-circular polarised polaritons is $g_p = \frac{|X|^4 g_X}{\gamma_{LP} A}$. Where $|X|^2$ is the exciton fraction, γ_{LP} is the polariton linewidth and A is the mode area [40]. Numerous groups have measured the polariton-polariton interaction strength, figure 1.6, with values spanning four orders of magnitude [35].

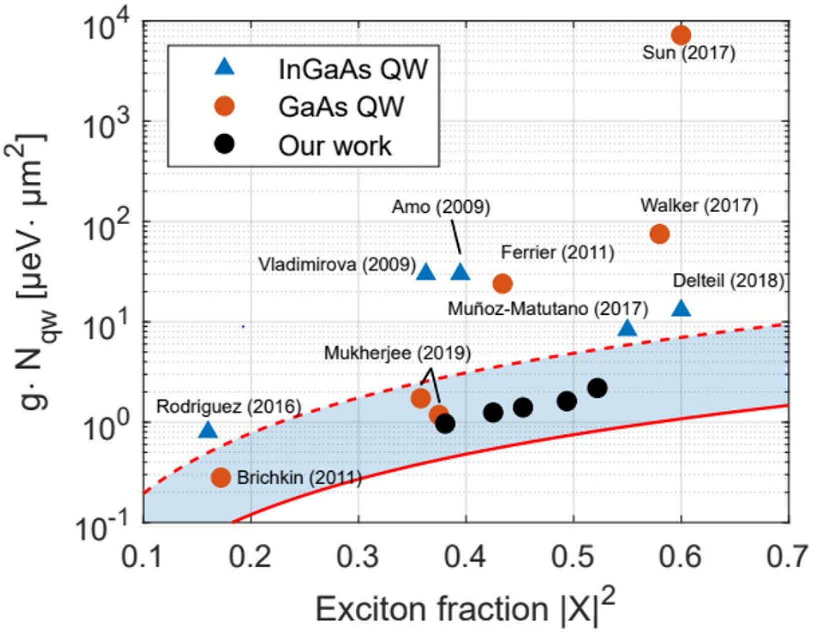

Figure 1.6: Comparison of reported values for the polariton-polariton interaction strength. Taken from [35].

1.4.2 Parametric scattering, optical parametric oscillations and optical parametric amplification

Exciting the lower polariton branch with specific energy and angle can result in two polaritons scattering to a *signal* and *idler* mode. The in-plane momentum for the two injected polaritons *pump*, and the new signal and idler modes must satisfy:

$$2k_{pump} = k_{signal} + k_{idler}. \tag{1.18}$$

Where k denotes the in-plane wavevector of the polaritons, this is a four-wave mixing process in nonlinear optics. This effect was reported by Stevenson et al. [41] where the excitation of the LPB at the point of inflection generated $k_{signal} = 0$ and $k_{idler} = 2k_{pump}$ states. Savvdis et al. [42] following this result, incorporated a second laser at normal incidence to the microcavity. This experimental scheme is called *pump-probe excitation*. Figure 1.7a shows the pair-scattering of polaritons into the new states, with the pump-probe setup shown in 1.7b.

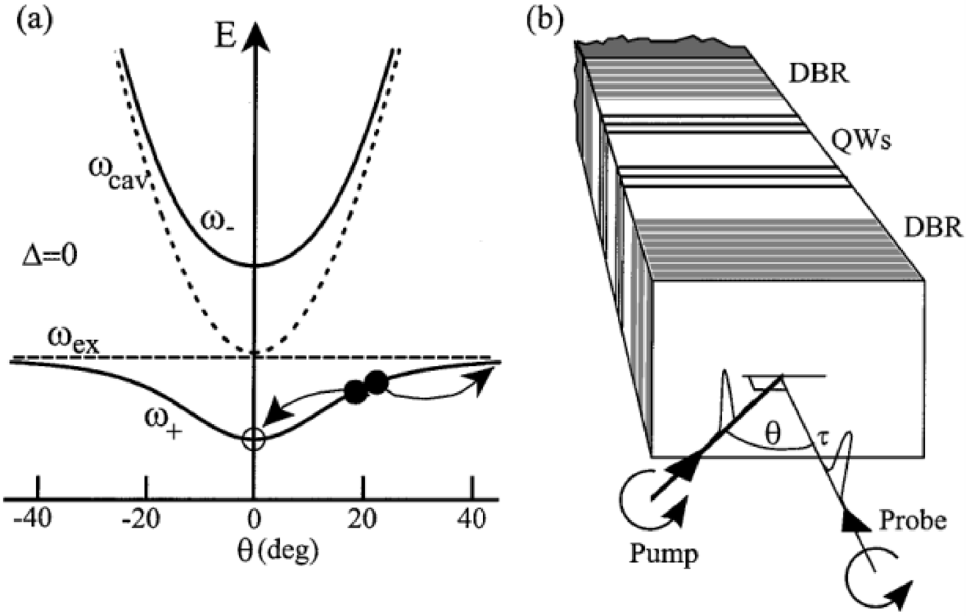

Figure 1.7: Pump-probe experiment performed on a planer microcavity. a) The LPB and UPB dispersion relations, with the angle of pump excitation matching the critical angle. (b) The microcavity structure and the angles for the circular pump-probe pulsed lasers. Taken from ref. [42].

The authors reported a significant increase in the $k = 0$ state when the pump is at the *critical angle*. For their zero detuned microcavity, the critical angle is 16.5°. The exciton-cavity detuning is shown by the dashed exciton and cavity lines in Figure 1.7a. The probe polaritons stimulate the scattering from the pump state; the effect is distinguished from four-wave mixing by the exponential increase in emission.

The stimulated scattering of polaritons occurs because of their bosonic nature. The coupling between the pump-signal-idler polariton states is called an *optical parametric oscillator*, with the threshold observed when the occupancy of the final signal state becomes close to unity. The phase of the pump polariton does not affect the phases of the signal or idler polaritons. Long-range spatial and temporal coherence was predicted [43] then observed soon after [44].

Krizhanovskii et al. (2008) [45] showed that self-organisation takes place when the coupling between the pump-signal-idler occurs. Causing renormalisation in the lower polariton branch, making the signal state the new $k = 0$ condensate.

1.4.3 Polariton bistability

Bistability was predicted by Tredicucci et al. [46] and demonstrated by Baas et al. LPB [47] for the polariton system. Detuning a laser (CW) above the $k = 0$ energy and gradually increasing the occupancy, the mode blueshifts until it reaches resonance with the laser. When this happens, a super-linear increase in transmission intensity is observed. Reversing the direction of power, going from high to low, the point where a sharp decrease is expected is significantly less. This *hysteresis* cycle can be seen in figure 1.8.

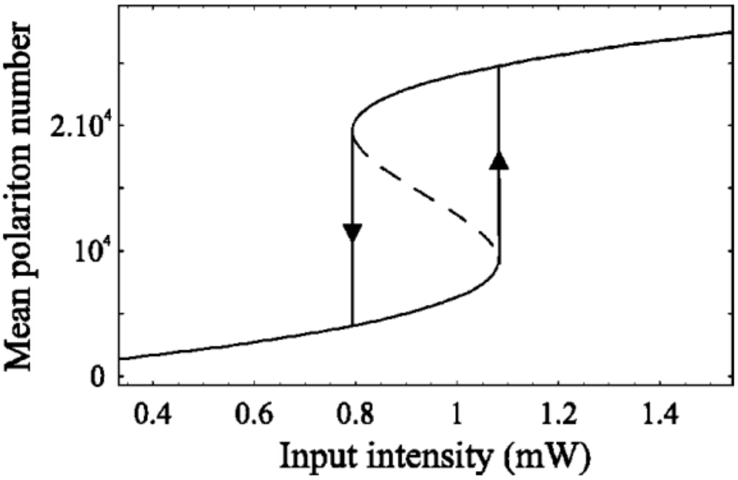

Figure 1.8: Bistable behaviour of the mean polariton number as a function of intensity. Taken from ref. [47].

Optical bistability is not a phenomenon exclusive to polaritons, with bistable media seen as an option for building optical circuits for computers [48]. For polariton systems, the bistable threshold has a switching behaviour and has industrial applications such as a polariton transistor [25, 49].

1.5 Polarisation

1.5.1 Pseudospin

The constituents of polaritons are electrons, holes and photons, all of which have a spin value. In GaAs the conduction band electrons have spin angular momentum $m_j = \pm 1/2$, while the valence bands of the light and heavy hole states have $m_j = \pm 1/2$, $\pm 3/2$ respectively [9]. Therefore the total angular momentum for an exciton will be projected along the ±1 or ±2 direction. The spin angular momentum of a photon is $m_j = \pm 1$; by the conservation of total momentum, this prevents coupling to the $J_z = \pm 2$. The $J_z = \pm 1$ exciton, photons can couple to and are called *bright excitons*, while $J_z = \pm 2$ are called *dark excitons* due to the fact, that light does not couple to them. The plus and minus components are the coupling between right (+1) and left (-1) handed circular polarisation. Under linear excitation, the photons couple to a mixture of right and left states. So, polaritons will have two different spin projections.

Pseudospin is a 4D vector that describes the polarisation direction. The vector direction is calculated from the *Stokes parameters*, represented as:

$$S = \begin{pmatrix} S_0 \\ S_1 \\ S_2 \\ S_3 \end{pmatrix} \tag{1.19}$$

Where S_0 is the total intensity. The other three parameters are calculated by measuring the polarisation in three orthogonal bases', and the first S_1 is horizontal and vertical:

$$S_1 = \frac{I_H - I_V}{I_H + I_V}. \tag{1.20}$$

The second Stokes parameter is measured for diagonal and anti-diagonal components:

$$S_2 = \frac{I_D - I_A}{I_D + I_A}. \tag{1.21}$$

While the third Stokes parameter is found by measuring on a circular polarisation basis:

$$S_3 = \frac{I_{\sigma+} - I_{\sigma-}}{I_{\sigma+} + I_{\sigma-}}. \tag{1.22}$$

Where I_H, I_V, I_D, I_A, $I_{\sigma+}$ and $I_{\sigma-}$ refer to the polarisation intensity resolved in horizontal, vertical, diagonal, anti-diagonal, right and left circular. It is represented by the Poincaré sphere, shown in figure 1.9. The S_2 parameter will measure the polarisation rotation in a polariton mode in chapter 4, then calculate the phase shift. The *linear polarisation angle* (LPA) ϕ is used to show the linear polarisation direction. ϕ will be used to show the transition from Rashba to a Dresselhaus like field in lattice emission in chapter 5 [4].

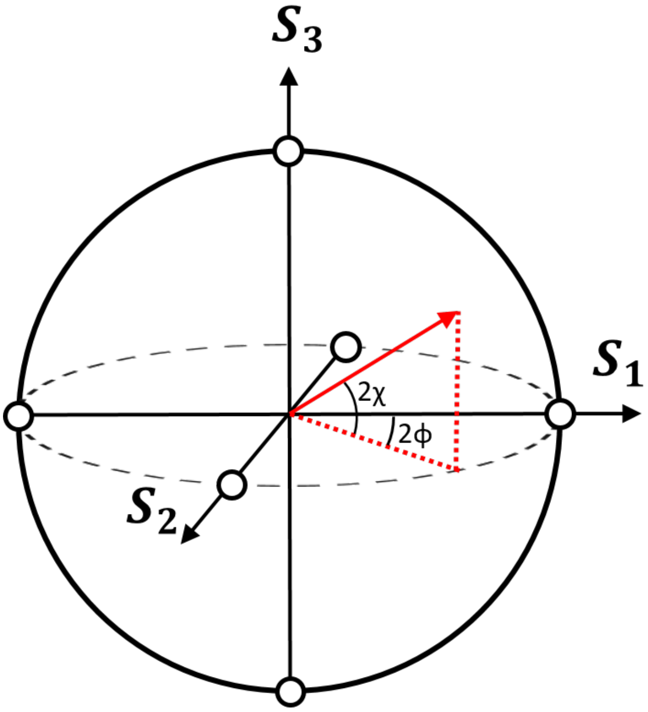

Figure 1.9: The Poincaré sphere.

1.5.2 TE-TM slitting

Polaritons have a transverse electric and transverse magnetic (TE, TM) mode splitting. The splitting is caused by an angular and polarisation dependent phase delay when reflection occurs in the DBR layers of the microcavity. The TE-TM splitting depends on the mismatch between the Fabry-Pérot frequency of the cavity, and the *stop band* frequency of the dielectric mirrors [50]. The TE-TM splitting can be seen by looking at the polariton dispersion relation and resolving in horizontal and vertical polarisation.

The Hamiltonian describing this splitting can be written in a circular polarisation basis:

$$H = \begin{pmatrix} H_0(k) & \Omega_{TETM}(k)e^{-2i\phi} \\ \Omega_{TETM}(k)e^{2i\phi} & H_0(k) \end{pmatrix} = H_0(k)I + \Omega_{TETM} \cdot \sigma \tag{1.23}$$

where k is the in-plane wavevector, ϕ is the in-plane angle (polar) between (k_x, k_y) and $\Omega_{TETM}(k)$ is the magnitude of the TE-TM energy splitting.

Ω_{TETM}= $\Omega_{TETM}(k)(cos2\psi,\ sin2\psi,\ 0)^T$ represents an effective magnetic field, which is analogous to spin-orbit coupling. The TE-TM field creates a pseudospin dependent splitting in the polariton modes, which, as previously mentioned, can be resolved on a polarisation basis. Figure 1.10a shows the TE-TM field in k-space around the degenerate k=0 point for a planar microcavity.

The direction of pseudospin can be seen in figure 1.10b. Comparing $\psi = 0$ and $\psi = \pi$, the phase change between the circular components is 2π. The resulting pseudospin points in the same direction. Also noticeable is that the pseudospin winds doubly during a full rotation around the origin in k space; these pseudospin textures can be visualised experimentally through the *optical spin-Hall effect*.

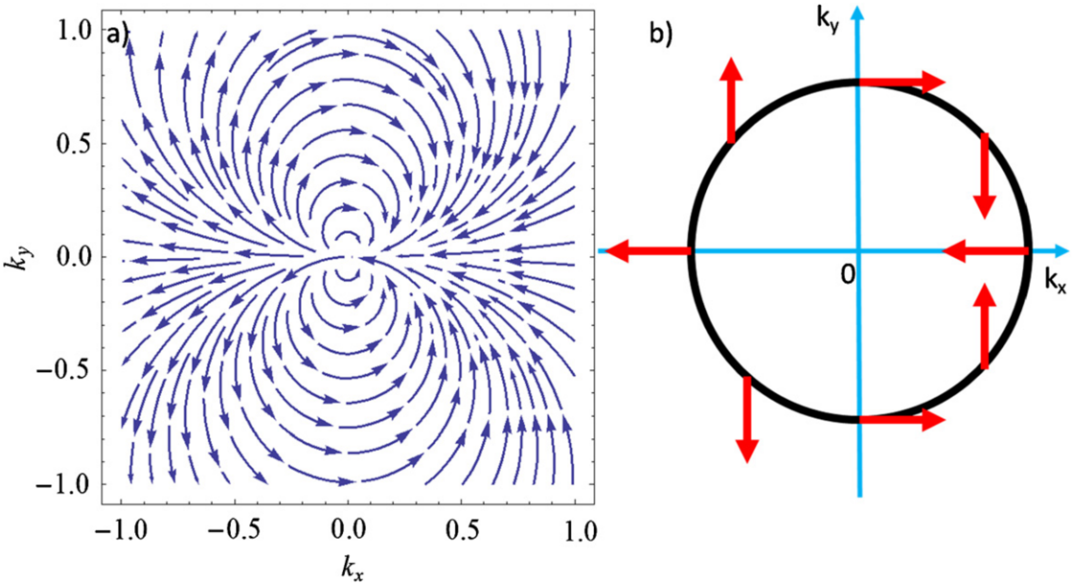

Figure 1.10: The direction of linear polarisation as a function of in-plane wavevector for a planar microcavity. a) TE–TM(**k**) field in the Fourier-space. b) The pseudospin of the polariton eigenstate is orientated along the effective B-field. Taken from ref. [51].

1.5.3 Optical spin-Hall effect

The spin-Hall effect generates a spin current perpendicular to the charge current flow. This can happen in two ways, electrons scattering from charged impurities (extrinsic) or spin-orbit coupling effects (intrinsic). Using charged carriers incur fast dephasing and decay due to electron scattering [52].

Polaritons can produce spin currents controlled by a polarised optical excitation [52], the so-called *optical spin Hall effect* (OSHE). In this optical analogue, the pseudospin of polaritons is linked to the in-plane momentum and produces polarisation textures in real and momentum space.

The evolution of the pseudospin is described by:

$$\frac{\partial \mathbf{S}}{\partial t} = \mathbf{S} \times \mathbf{\Omega}(k) + \frac{\mathbf{S_0}}{\tau_1} - \frac{\mathbf{S}}{\tau}. \tag{1.24}$$

With the first term describing the precession of the polariton pseudospin, the second is due to the initial state scattering (Rayleigh scattering), and the final term is the radiative relaxation term. Under resonant excitation, a Rayleigh ring is created, similar to figure 1.16 b(iv). The effective magnetic field creates four domains, two of σ^+ and two of σ^-. The momentum space S_3 parameter has a quadrant circular polarisation textures for a linear input polarisation, as shown in figure 1.11a. The corresponding real-space image shown in 1.11b.

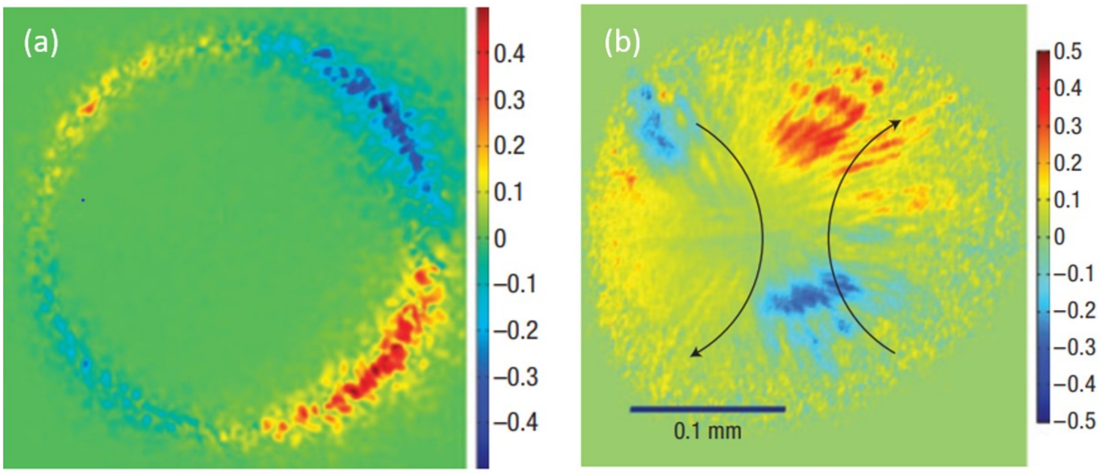

Figure 1.11: The optical spin-Hall effect in a planar microcavity. a) The S_3 parameter in real space collection. (b) The S_3 parameter in k-space collection. Taken from ref. [52].

These two images demonstrate the precession of polariton pseudospin around an effective field. The polariton pseudospin separates in real space once they move away from the centre of the pump spot. In Chapter 5, a TE-TM field that mimics Dresselhaus SOC is used to replicate similar results. The work relies on the engineering of the bandstructure in photonic structures [4].

1.6 Collective phenomena

1.6.1 Relaxation processes

Under non-resonant optical excitation, free electron-hole pairs are created through photon absorption. They thermalise via interactions with optical (LO) and acoustic (AC) phonons [9, 26] to the lower polariton branch.

The logic of the polariton relaxation is as follows. The exciton dispersion is populated when the e-h pairs generated by the laser excitation interact with LO phonons [9]. The polariton dispersion has two regions, the optically active and dark region. The optically active region has excitons that couple to photons, with the lifetime of polaritons related to the photon cavity lifetime, typically a few picoseconds [9, 53]. The dark region excitons have a wavevector larger than the light wavevector. In contrast to the former region, the particles have a long lifetime. This is because polaritons decay through nonradiative channels, with decay times of the order of hundreds of picoseconds [9]. Other distinguishing features are that the density of states is large, and the dispersion relation has a gradual curvature.

Figure 1.12 shows the relaxation mechanisms for polaritons, where high k-vector excitons interact with acoustic phonons, taking them to the intersection between the dark and active regions. This process takes between 100-200ps as the energy exchange is not very efficient - with 10ps per relaxation step and 1meV exchanged. Even at this stage, the polaritons need to lose 5-10meV to reach the minima of the lower polariton branch. Through interactions with acoustic phonons, the relaxation time would be at least 50ps, which can be several times the lifetime of the polaritons in the active region.

This slow relaxation results in polaritons accumulating in the higher momenta areas in the dispersion. This area is known as the *bottleneck effect* and was predicted by Tassone et al. [54] (1997) and experimentally observed by Tartakovskii et al. [55]. Polaritons become stuck in the bottleneck region under low excitation powers. By increasing the polariton density in this region, inter-particle scattering by; polariton-polariton, polariton-exciton and exciton-exciton all contribute to suppressing the bottleneck feature.

More relaxation channels become available when this stronger excitation is used. The outcome, polariton relaxation to the ground state is more efficient compared to relying on acoustic phonons at low polariton densities.

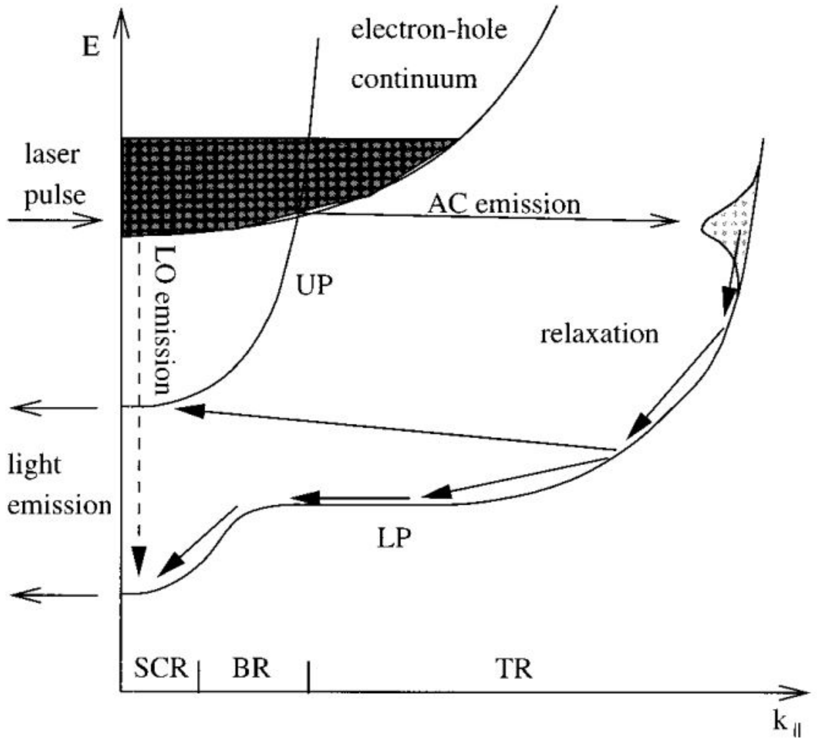

Figure 1.12: Schematic of non-resonant excitation and the formation of polaritons. The free-carrier thermal reservoir, scattering processes via acoustic phonons (AC) and radiative recombination. Noted at the bottom x-axis is the strong coupling regime (SCR), the bottleneck region (BR) and Thermal region (TR). Taken from ref. [54].

1.6.2 Bose Einstein condensation

Bose-Einstein condensation (BEC) is a name given to describe the phase transition of a gas of bosons, whereby quantisation of the translational motion of the particles may be observed. A macroscopic fraction of the total number of particles occupies the zero velocity state in the statistical mechanics' framework. The transition temperature for non-interacting particles in a gas is given by:

$$T_c = 0.0839 \frac{h^2}{mk_B} (\frac{N}{V})^{\frac{2}{3}}. \tag{1.25}$$

Where T_c is the critical temperature for the BEC phase transition, h is Planck's constant, m is the mass of the particle, k_B is Boltzmann's constant, N the number of particles and V the volume occupied. BECs have several experimental challenges associated with them. The atoms must be separated sufficiently to avoid liquefaction, magento-optic traps, and Doppler cooling techniques. These techniques will take the atoms to near the *recoil limit*, which is set by random thermal energy as a result of spontaneous emission by the atom in random directions. Next, the lasers are switched off, and the magnetic trapping potential is reduced, meaning that the atoms with sufficient kinetic energy may escape, reducing the overall energy within the trap. The first observation was made by Anderson et al. [56] using rubidium-87 atoms and was shortly followed by Ketterle et al. [57] using sodium atoms, both would share a nobel prize for their observations. A diagram of the optical trap and images showing the onset of BEC is displayed in figures 1.13 and 1.14.

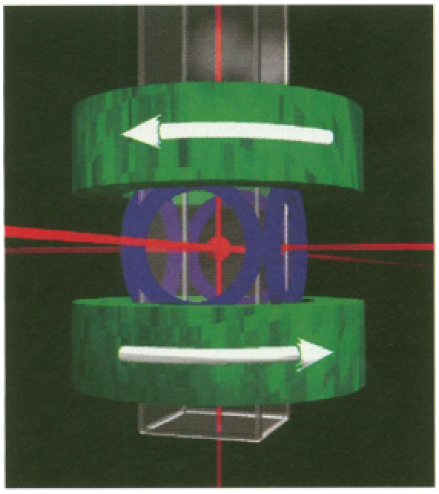

Figure 1.13: The magnetic-optical trap is used for laser cooling. The red lines indicate the laser excitations coming from three different axes. The white arrows on the top and bottom indicate the direction of the current, which induces the magnetic field for trapping and subsequent evaporation. Taken from ref. [56].

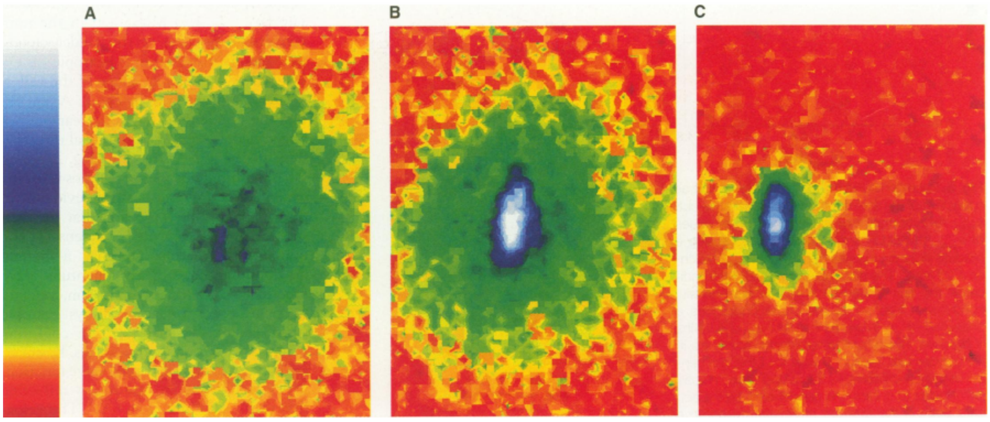

Figure 1.14: The velocity distribution of the Rb cloud. (A) before condensation, the (B) onset of condensation and (C) when evaporation has left only the condensate. Taken from ref. [56].

1.6.3 Polariton condensation

Shortly after the results mentioned in the previous section, A. Imamoglu proposed that polaritons may undergo a kind of BEC transition [58]. Polaritons have a low effective mass due to the strong coupling to the cavity mode, therefore, there was a strong possibility that a BECs would be seen at cryogenic temperatures. Polaritons have an effective mass 10^9 times smaller than the rubidium atoms mentioned before, meaning that the complicated atomic traps and cooling to micro-kelvin temperatures would not be required.

Accessing the polariton; coherence, polarisation and population can be done by measuring in far-field (momentum space) imaging, this imaging gives direct properties of the polariton wavefunction. In 2006, Kasprzak et al. [26] demonstrated condensation into the ground state with a population out of thermal equilibrium. They excite a cadmium telluride (CdTe) based microcavity non-resonantly, shown in figure 1.15. A threshold is marked by an increase nonlinear in intensity and narrowing of the polariton linewidth, with the condensate building up long-range spatial coherence and temporal coherence.

The system is still in the strong coupling regime, with the blueshift observed being $1/10^{th}$ of the Rabi-splitting and the coherence time increases from $1.5ps$ to $6ps$ above the threshold. The radiative lifetime of the polaritons is short when close to the threshold, while the dephasing time of polariton-polariton scattering is less than this lifetime. Above the threshold, relaxation to the condensed state is boosted by *stimulated scattering*, the polarisation of the emission becomes aligned to the [110] axis of the microcavity. The output polarisation is not correlated with the laser polarisation, which removes the possibility of a parametric amplification process being the source of the acquired polarisation. Below the threshold, the population is depolarised.

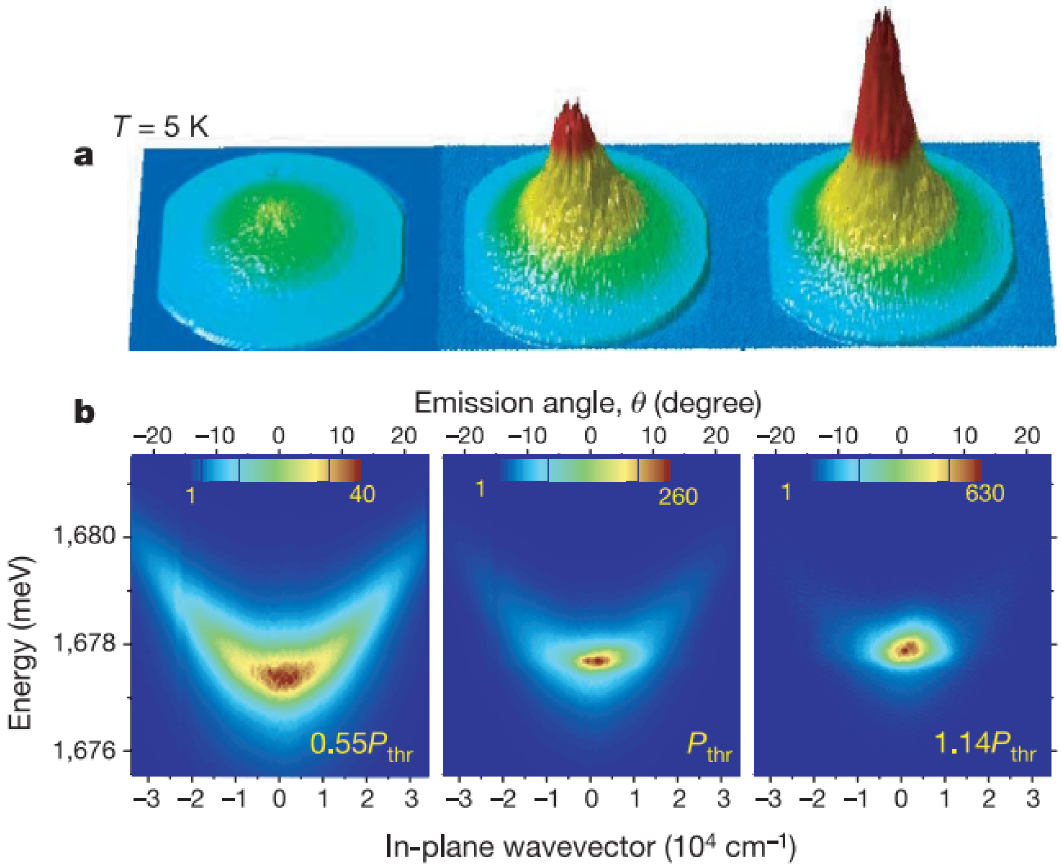

Figure 1.15: Far-field imaging of polariton angular distribution inside the cavity. (a) Series of tomographic scans in the angular intensity in Θ_x and Θ_y direction. (b) In-plane wavevector resolved in energy for three input powers, revealing energy narrowing and blueshift. Taken from ref. [26].

BEC of polaritons have been observed in multiple microcavity systems; GaAs [59], ZnO [60], GaN [17] and organic microcavity [24].

Polariton condensation sparked interest from the atomic BEC community, with the key talking point beingthat the system is out of thermal equilibrium, meaning condensation can occur in excited states and above the minimum energy of LPB. Even when condensation is observed in the low energy states, most of the population are excited states are in the exciton reservoir.

The emission from the polariton condensate is often called a *polariton laser*, where the polariton condensate spontaneously emits light [58]. The source is monochromatic and with a fixed wavevector and is coherent. A polariton laser does not require stimulated emission, in contrast conventional lasers that require *population inversion.* Experimental demonstration of a polariton laser has been done in many systems; GaAs [61](T=40k), CdTe [62] (T=50k), GaN [63] (T=300k) and ZnO [64](T= 120K).

Aside from the novelty of generating condensates, there is great interest in controlling the propagation. Optical control has been demonstrated for both confining a condensate and propagating over macroscopic distances [61]. In more recent experiments, microcavities have been etched into periodic arrays to produce a topologically protected moving condensate [30]. Novel experiments on condensates like these open the way for polariton based circuits, with the ultimate goal of high-speed all-optical information processing [61, 65].

1.6.4 Superfluidity

Following the demonstration of polariton condensates, there was significant interest surrounding the closely related phenomena of superfluidity. Superfluidity was co-discovered independently in LHe experiments in 1938[66, 67]. Superfluids behave differently from ordinary fluids; fork-like dislocations appear in interferogram measurements when rotated. The fork-like dislocations or *quantised vortices* were observed in the polariton system by Lagoudakis et al. [68], with the authors remarking that observing the vortices was insufficient to claim superfluity for a non-equilibrium system.

The confirmation of superfluid polaritons came from Amo et al. [27], observing suppressed scattering from defects when the flow velocity of polaritons v_p is slower than the speed of sound in the fluid c_s. The condition $c_s > v_p$ is known as the *Landau criterion* for superfluidity [69]. Their experiment involved resonant frequency-momentum tuning of the injected polaritons, until the condition was met.

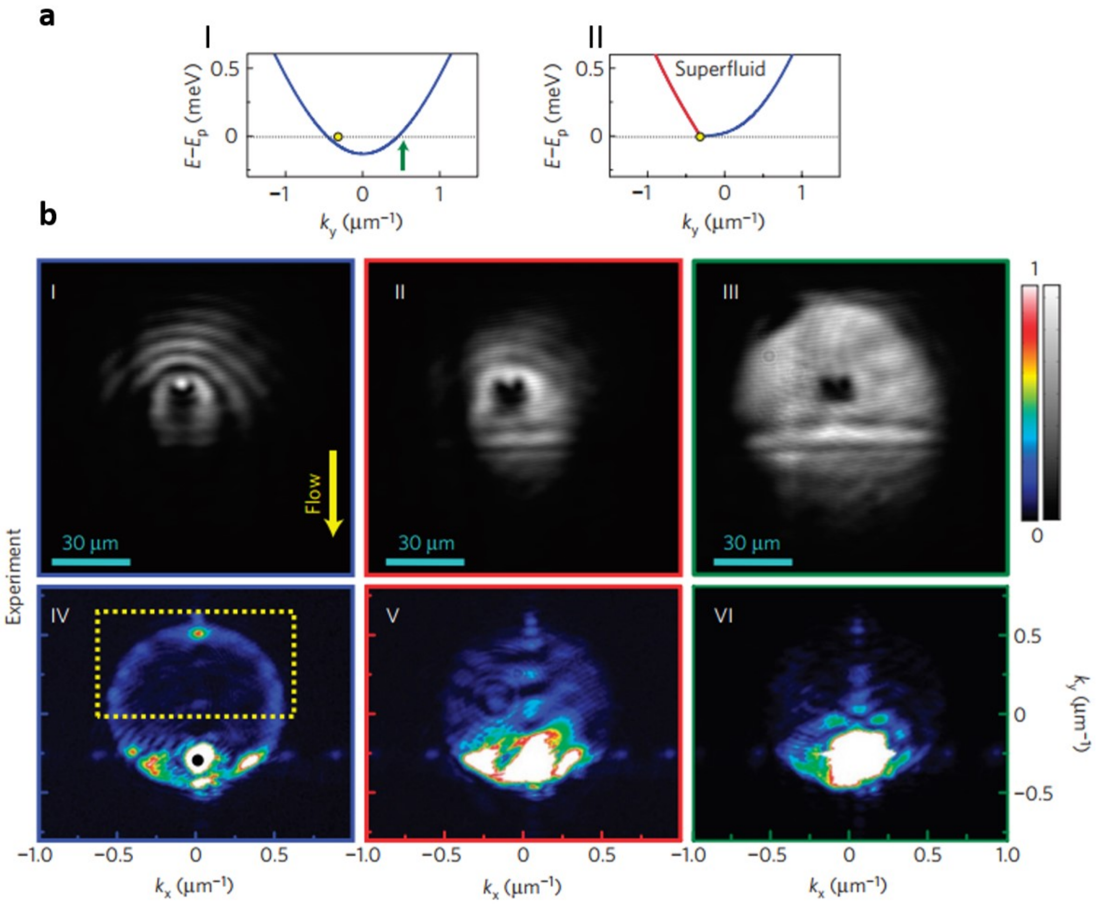

Figure 1.16: Far-field imaging of polariton angular distribution inside the cavity. (a) Series of tomographic scans in the angular intensity in Θ_x and Θ_y direction. (b) In-plane wavevector resolved in energy for three input powers, revealing energy narrowing and blueshift. Taken from ref. [27]

Looking at figure 1.16a, two in-plane dispersion relations are shown for the LPB of a microcavity. A faint line at $E - E_{pump} = 0$ shows the energy of the polariton states injected by a continuous wave laser. Polaritons injected at this energy may scatter to other states if the in-plane momentum is conserved, with the *Rayleigh ring* shown in figure b(iv). They increase the excitation power, which increases the number of states. Polariton-polariton interactions increase, leading to a blueshift in the LPB towards the laser's energy. The dispersion can be seen on figure 1.16 a(ii), where the dispersion becomes distorted. The distorted dispersion removes the like-pump energy scattering pathway as seen in the Rayleigh ring, shown in figure 1.16 b(iii) and b(vi). In Fourier space image b(vi), the scattering to states in the ring is suppressed, and the accompanying real space image b(iii) shows no scattering around the central defect.

More recently, room-temperature superfluidity was achieved [70] using an organic microcavity, with the sample supporting Frenkel exciton-polaritons.

Superfluidity protects the polariton fluid flow around defects, with the protection realised through polariton–polariton interactions which distort the dispersion for microcavity polaritons. The topological polaritons section will explore the theme of transport and protection for a polariton condensate, with the TE-TM splitting and magnetic field sensitivity of polaritons making this possible.

1.7 Topological polaritons

Polaritons are hybrid light-matter particles and when confined in microstructures, their photonic component has a transverse-electric transverse-magnetic (TE-TM) splitting, analogous to spin-orbit coupling. In periodic arrays, the bandstructure of polaritons is engineered to produce new TE-TM field relationships. The other component is the exciton, which is sensitive to magnetic fields. When an external magnetic field is applied to polaritons, they experience a Zeeman splitting [4] between right- and left-circular polarisation states. A *Chern insulator* hosts topological channels of light, which support unidirectional transport; immune to certain types of disorder and backscattering. *Topological insulators* were first investigated in electronic band structures, allowing for control of electron transport. More recently, photonic structures have been at the cutting edge of this research [71].

Topology is a field of study in mathematics that classifies objects according to their geometric characteristics. Topological edge states emerged in the 1980s in a series of quantum Hall (QH) effect experiments. Applying an external magnetic field to a 2D-electron gas at low temperature produced quantised Hall conductances in a slab material [72, 73]. Critical elements of QH systems are: electrons propagate only at the edges of the system, it is one-way transport and is protected against disorder in the material [74, 75].

The *Chern number* of a system is a topological invariant, which is an integer calculated by the integration of the *Berry curvature* around the first Brillouin Zone [76]. Suppose the Chern number is a non-zero value, the insulator is said to be *topological*, with the number related to the expected *edge states* in the system. An edge state in electronic systems (QH) has persistent unidirectional conduction around the sample edges; this property appeals to optical analogues with photons and polaritons. The quantum-Hall effect requires an externally applied magnetic field; this breaks the system's time-reversal symmetry, which is essential to forming edge modes.

The QH system discussed has one edge state that propagates around the edge of the material. Different kinds of edge states were proposed in graphene [77], where for this system, the transport of spin and charge at the sample boundaries is possible, this is called the *quantum spin-Hall effect*. The physical mechanism relies on electrons experiencing a strong spin-orbit coupling (SOC) and a bandgap opening at the Dirac point. The group velocity of an electron is locked to its spin, this is called *spin-momentum locking*, which allows for helical edge states to propagate without backscattering [78, 79].

The following section discusses the two experimentally demonstrated edges states for polaritons. One platform uses a one-dimensional chain, while the other uses a honeycomb lattice geometry.

1.7.1 Polariton topological insulators 0D and 1D edge states

The Su-Schrieffer-Heeger model (SSH) was used to describe the electronic properties of Polyacetylene [80], shown in figure 1.17. In the case of Polyacetylene, sites A and B would be carbon atoms, and t (t') describe the intra- (inter-) coupling strength between carbon bonds. Using the *tight-binding model*, a lattice with this structure will behave differently for the same wavevector for cases: $t < t'$, $t = t'$ and $t > t'$.

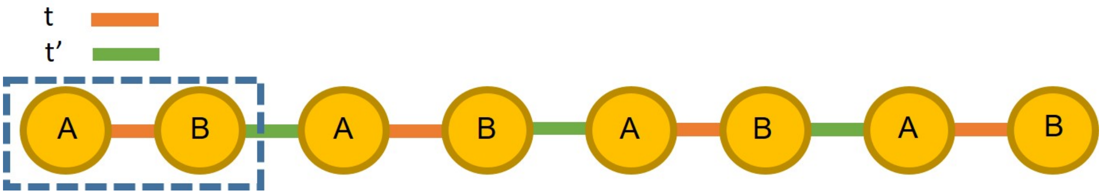

Figure 1.17: SSH chain schematic showing coupling strengths between sites A and B, where t is the intra-coupling strength and t' is the inter-coupling strength.

The interesting case is for $t < t'$, under this condition considering a finite chain length, there is a non-zero winding number, indicating an edge state in this 1D chain of sites. This scheme was implemented using polariton micropillars [29]. The single pillar mode structure will be shown in the methods and later sections. For now, it is enough to say that there is a polariton energy structure in the pillar that resembles s-like and p-like atomic orbital modes. The p-like mode is described as P_x and P_y, which have perpendicular spatial orientation in the pillar. The pillars are arranged in a zig-zag pattern, with an overlap between nearest neighbours. The orbitals have different coupling strengths to the nearest neighbours, which the authors refer to as the longitudinal and transverse coupling (or hopping) strengths t_l and t_t. Using an elongated (elliptical) laser spot on to zig-zag chain in two configurations, at the edge and in the centre of the structure—figure 1.18 [29]. Exciting at the edge leads to the formation of a localised P_y state, in contrast to the other band states that are delocalised over the entire chain, as shown in figure 1.18c-f.

The two Fourier-space PL images figure 1.18a-b show that the P-band has an additional state positioned at the centre for edge excitation. They also demonstrated lasing in this topological mode by gradually increasing the excitation power. The mode beats out competition from other modes due to the large density of states available. This topological model is robust against disorder in hopping, providing chiral symmetry is preserved. The eigenspectrum is symmetric around $E = 0$, with the edge states having energy E=0. Fluctuations in t and t' do not destroy the protection, and strong localisation of the P_y mode was still maintained when on-site disorder changed the energy from $E = 0$ to energies within the gap. If the mode energy changes significantly, then hybridisation with other modes is possible.

The demonstration of a 0D edge state was a step forward, but a bigger goal is to use topological protection for a moving edge state. A proposal for supporting 1D edge states is based on graphene in the exciton-polariton system. Here, micropillars are arranged in a honeycomb geometry resembling the C6 symmetry of carbon atoms of graphene. Polaritons have been studied in single, dimerised [81], Lieb [82], Kagome [83] and the honeycomb (graphene) [84] geometry. The honeycomb lattice has been shown to support a Dirac-cone dispersion along with edge modes [84]. Dirac-cone dispersions are regions in the bandstructure where the in-plane momentum is linear with energy—the intersection of the conduction and valence band is known as the Dirac-point. In artificial or electronic graphene, there are 6 Dirac points in the S-band, three $\mathbf{K}$ and $\mathbf{K}'$ points. These points are not equivalent and have a different local *winding* of the phase of the wavefunction around the respective K (K$'$) cone.

The 1D moving edge state was realised in this system by Klembt et al. [30], using a strong magnetic field to break time-reversal symmetry. The system is said to be non-trivial because a gap is opened at the Dirac points **K-K'** under a smooth deformation, which is driven by the interplay between effective SOC (TE-TM splitting) and the external magnetic field. This system has $C = \pm 2$, classifying it as a QH system allowing for one-way edge modes. They could see the polariton transport by non-resonantly exciting at the zig-zag edge of the lattice. Looking at figure 1.19, they pumped above the threshold, condensing polaritons into the K (K$'$) S-band energy locations. Then, a bandgap is opened at the Dirac point by applying the magnetic fields. Through careful selection of lattice and sample parameters, the authors were able to find a sample with a sizeable TE-TM splitting $\Delta_{TE-TM} = 384\mu eV$ and an effective Zeeman splitting $\Delta_{eff} = 22\mu eV$ at the Dirac point. They resolve the opened Dirac point gap to be $108 \pm 32\mu eV$ using a $B = +5T$ magnetic field.

Exciting non-resonantly and condensing polaritons into the gap, then applying a +5T and -5T magnetic field. They see a signal intensity around the edge of the lattice, noting that the intensity at the edge mode energy is seen far from the pump spot. The mode was recorded travelling across a defect site and around a 90° bend in the lattice. Figure 1.19 shows this edge state intensity around the lattice. Using far-field imaging, selecting the edge mode energy, they were also able to show chiral propagation of the edge state.

Nonlinear effects are of interest in topological polariton research [71]. With 1D edge state lasing demonstrated, other platforms have achieved zero and one dimensional lasing [85–87]. Other geometries such as the Kagome [88] and Lieb [89] are still under investigation for polariton topological protection.

Recently, another class of topological systems was developed using the valley degree of freedom. These systems are called valley-Hall topological insulators [78]. In these systems, two lattices with opposite valley topological invariants are interfaced. The interface supports unidirectional channels of light and is robust to sharp bends, and random disorder [90, 91]. Unlike spin-Hall edge states, which form inside the light line and therefore are leaky [91, 92], the valley-Hall edge states form outside the light line. Polaritons have yet to be explored in this platform, but the fabrication of such lattices would be possible with the current etching technology.

Karzig et al.[93] in 2015 proposed a topological insulator architecture for polaritons, calling the resulting states *Topolaritons.* This proposal is for polaritons in waveguides, where polaritons are confined by total internal reflection and propagate with high momenta.

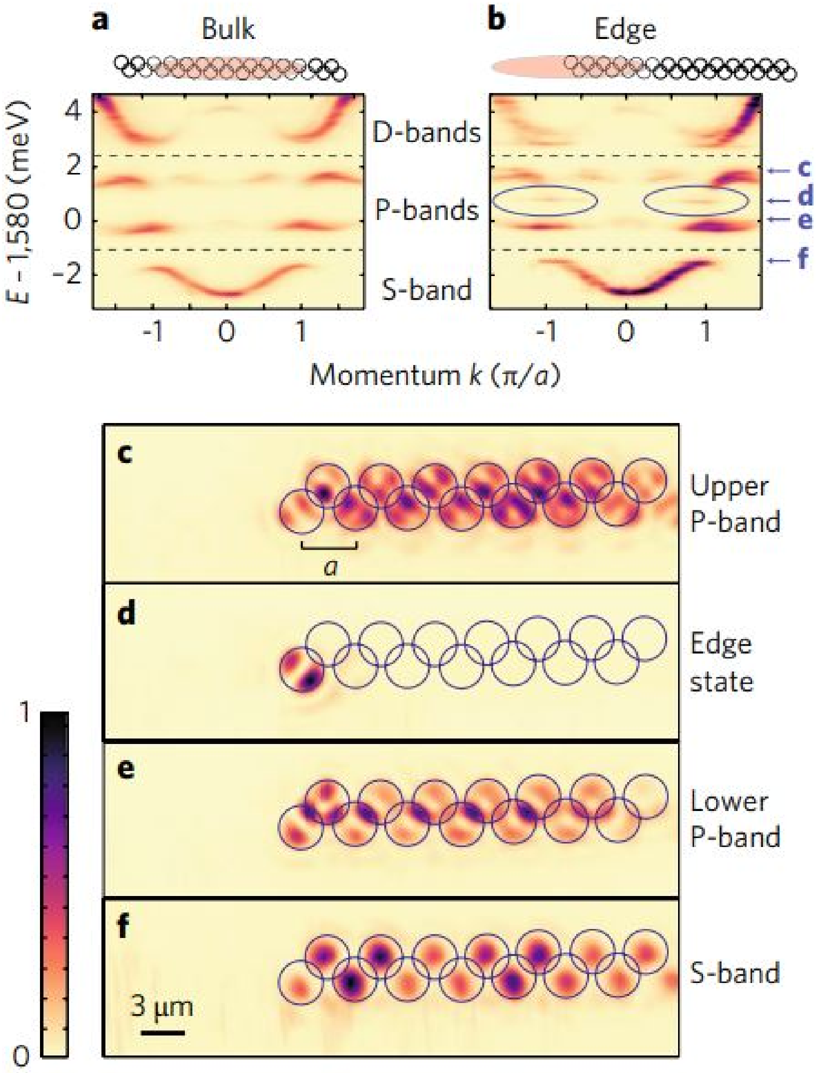

Figure 1.18: SSH chain excitation for Bulk and Edge region. a) Fourier space image showing the band structure for the Bulk. b) Fourier space image showing the band structure for the Edge. Note the appearance of the edge state mode in the P-band. c) Real-space imaging for the upper P-band. d) Real-space imaging for the edge state. e) Real-space imaging for the lower P-band. f) Real-space imaging for the upper S-band. Note that the PL is localised only on the edge pillar for the edge state, compared to the other mode emission. Taken from ref. [29].

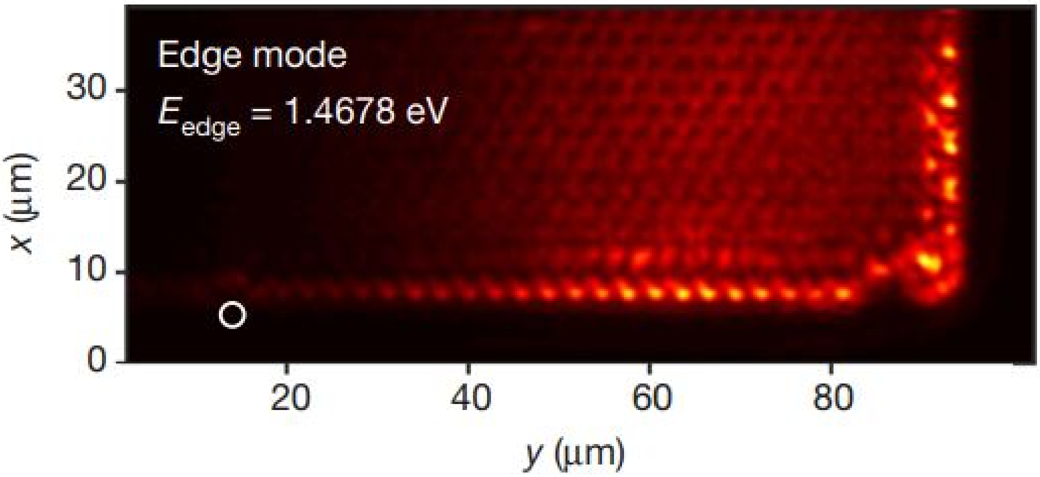

Figure 1.19: The edge state intensity is visible around a bend and an artificial defect in the lattice. Taken from ref. [30].

1.8 Polariton blockade

The photon blockade for an emitter coupled strongly to a cavity was proposed by Imamoağlu [94]. When considering a finite-level system (atom) coupled to the quantum harmonic oscillator, the resulting system will have an anharmonic (irregular) and harmonic (regular) energy spectrum. The Jaynes-Cummings model describes a two-level system coupled to a photon, absorbing or emitting a photon results in going up or down in energy, as can be seen in figure 1.20a.

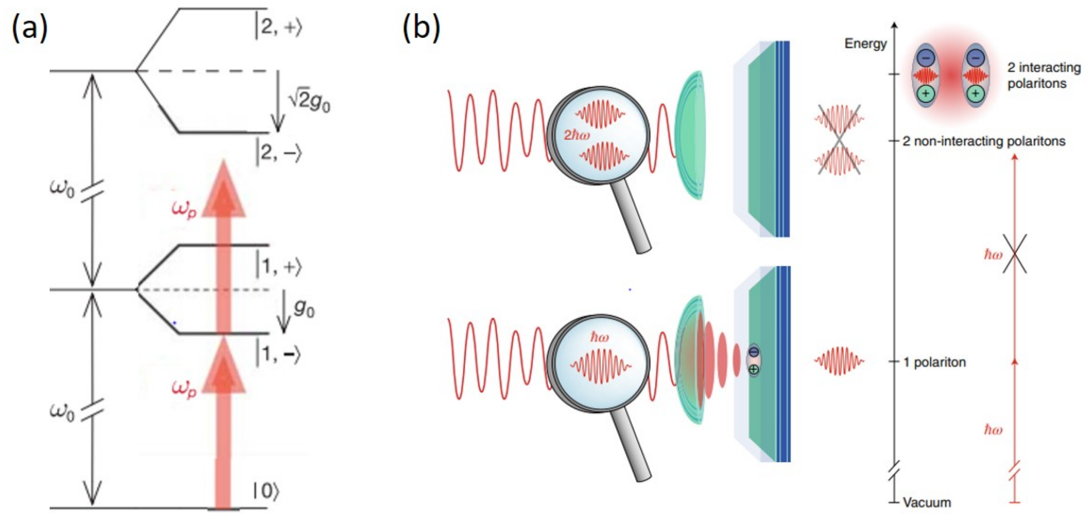

Figure 1.20: The Jaynes-Cummings model for a photon ladder in a QD and the polariton conventional blackade. (a) taken from ref. [95] and (b) ref. [96].

The energy spacing can be written as:

$$E_{i,\pm} = i\hbar w \pm \sqrt{i}\hbar g_0. \tag{1.26}$$

The level spacing for the small occupancy is anharmonic, meaning the resonant driving w_p will not populate the system further when going to the $|2,\pm\rangle$ state. Leading to subpoissonian photon emission from the $|1,-\rangle$ state [95]. This effect is known as the *conventional blockade.* Verger, Cuiti and Carusotto proposed this model for the polariton system [97], looking at the size of the nonlinear energy shift U and decay rates κ. They study the second-order coherence for a variety of pumping detuning, which are shown in figure 1.21. They conclude that anti-bunching and bunching are possible given a strong nonlinearity.

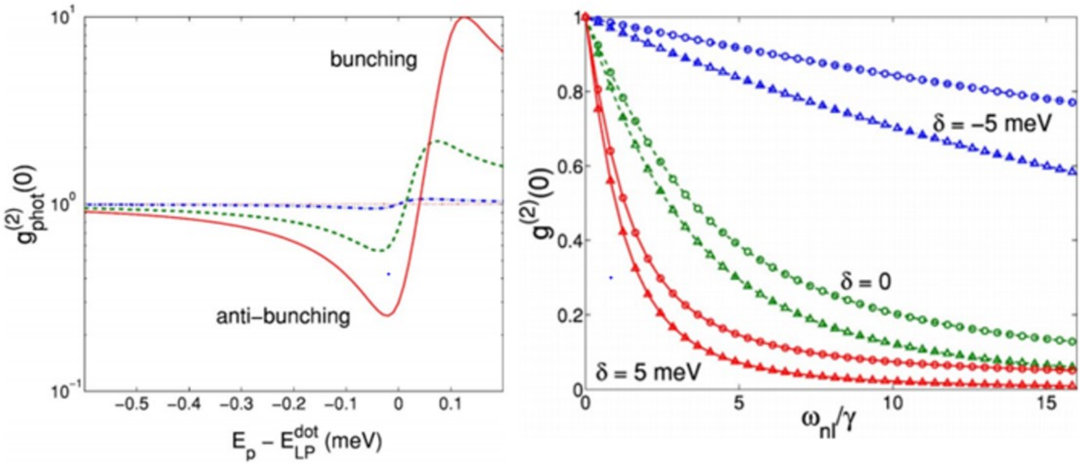

Figure 1.21: The second-order coherence function, $\mathbf{g^{(2)}(0)}$, for a photonic dot. a) The expected $g^{(2)}(0)$ for three exciton-cavity detunings vs laser to polariotn mode detuning. (b) The $g^{(2)}(0)$ expected value for three exciton-cavity detunings, where the strength of the nonlinearity of the polariton is increased. Taken from ref. [97].

The exciton-exciton interaction typically ranges from $g_X = 5 - 10\mu eV \mu m^2$ [35, 98] in GaAs based devices. When the energy shift associated with two polariton occupancy is greater than the linewidth of the one polariton state, the conventional blockade is achieved. The conventional blockade approach is shown in figure 1.21b. Microcavity design improvements have led to smaller polariton linewidths, with higher Q-factors in a microcavity. The world-leading experimental result was reported by Imamoa$\bar{g}$lu [31]. Even though the nonlinear blueshift is smaller than the mode linewidth, they still report weak antibunching effects. They used an open cavity (fibre-cavity) design that allows the cavity length to be changed.

Testing at the optimal exciton fraction and linewidth for the polariton mode; as the LPB tends to ever higher exciton fractions, the linewidth suffers from broadening through inhomogeneous effects relating to the exciton. Using a red-detuned laser excitation, 5% anti-bunching was seen, shown in figure 1.22b. Munoz-

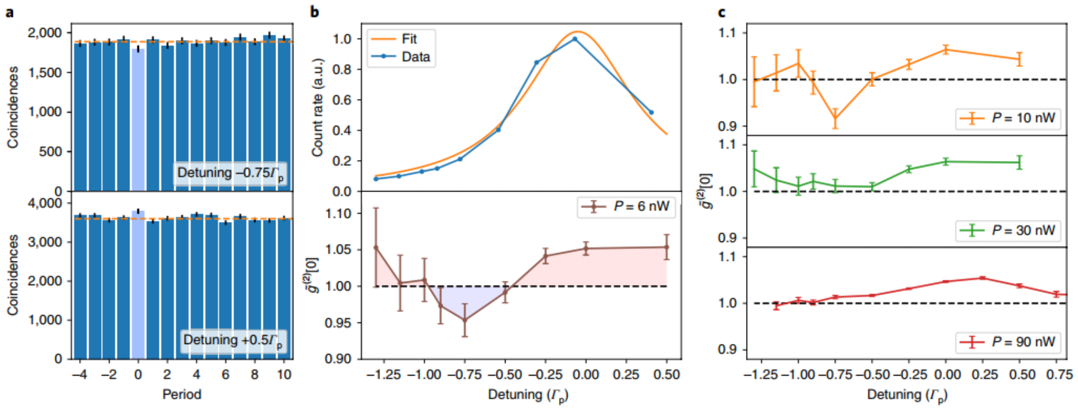

Figure 1.22: Weak anti-bunched and bunched light from a polariton mode. a) the $g^{(2)}(0)$ value for 6nW detuned from the mode peak. b) the transmission linewidth of the polariton mode, with the $g^{(2)}(0)$ value plotted as a function of excitation laser detuning. c) $g^{(2)}(0)$ with different laser-mode detunings for incident powers 10nW, 20nW and 90nW. Taken from ref. [31].

Matutano et al. [40] reported a similar level of anti-bunching the same year.

The current values of anti-bunched light in the polariton system are small, the main difficulty in achieving strong polariton-polariton interactions, while maintaining narrow linewidths. This problem will persist with studies on the conventional blockade, therefore, alternative proposals have been put forward for achieving anti-bunched light in polariton systems.

Liew and Savona [99] proposed a photonic molecule where two modes are coupled to each other and can interact through tunnelling between micropillars; this configuration is the *unconventional photon blockade.*In another proposal, Kyriienko and Liew discussed the *parametric blockade* [1] for a χ^2 weak nonlinear system with particles that can *parametrically scatter*. In parametric scattering, a signal and idler mode are produced above and below the central energy mode. They analysed emission from a central dipolariton mode undergoing parametric scattering with strong signal excitation, concluding that the emission from the central mode is strongly anti-bunched. This paper is the motivation for chapter 3, where a polariton micropillar device is used.

Chapter 2

Experimental methods

2.1 Sample growth

The microcavities used in this work came from two sources; one based in Sheffield grown by Dr. Ed Clarke at the EPSRC National Epitaxy Facility designed by Dr. Paul Walker, and the other was fabricated in Paris at the centre for nanoscience and nanotechnologies, C2N, as part of the Quantera collaboration across multiple European countries.

The Sheffield sample is a GaAs microcavity with 23 (26) top (bottom) GaAs/$Al_{0.85}GaAs_{0.15}$ distributed Bragg reflector pairs and six $In_{0.04}Ga_{0.96}As$ quantum wells. A benefit of introducing a low indium content into the QWs is that the emission energy is shifted away (lower) from the GaAs substrate, allowing samples of this kind to be measured in transmission geometry.

The sample provided by C2N is a GaAs cavity, containing a single 15nm $In_{0.05}Ga_{0.95}As$ quantum well (QW) at the electric field antinode and embedded between two $Al_{0.1}Ga_{0.9}As/Al_{0.95}Ga_{0.05}As$ Bragg mirrors.

2.1.1 Pillar etching

The Sheffield sample was etched into multiple micropillar structures by Dr. Ben Royall of the University of Sheffield Growth Facility. An array of geometries such as single, dimers, Lieb and Honeycomb lattices are etched onto the microcavity. The areas of interest in this sample were the honeycomb lattice and the unetched region. Pillars are etched completely through the top and bottom DBR layers, deep etching creates a larger confinement potential for the polariton modes but leads to exciton linewidth broadening and more significant surface recombination rates. The recipe for fabricating the micropillars is as follows:

1. Develop the appropriate sequence, shapes and dimensions for the designs in a programming language of choice and import them to Raith Voyager software (or equivalent software).

2. Prepare the microcavity sample for the designs to be patterned. Involves; cleaning with solvents, hard-mark deposition and a positive/negative resist coated evenly onto the sample.
3. Expose sample through electron beam lithography to imprint designs onto the surface of the resist.
4. Develop the resist to see the desired etching pattern.
5. Etch away hard mask.
6. Plasma ashing to remove remaining resist.
7. Inductively coupled plasma etch down to the depth of interest.

The final result of the etching process is shown in figure 2.1, showing a honeycomb structure similar to the one used in chapter 5. Looking at 2.1b, the DBR stacks are visible along with the GaAs cavity which appears as a lighter colour.

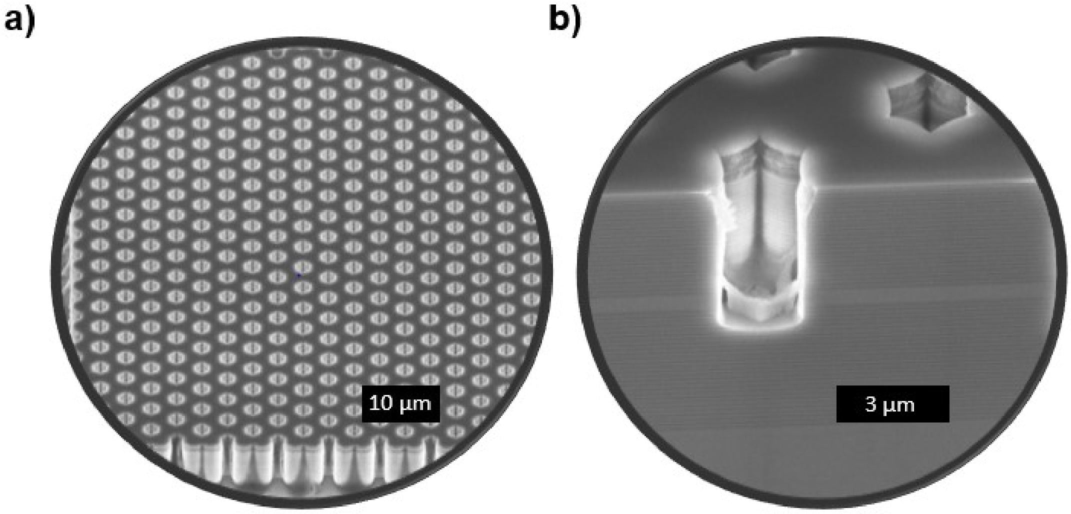

Figure 2.1: Result of the fabrication process for the Sheffield Sample. a) Pillars are etched into a honeycomb geometry with the diameter of the pillars being $3\mu m$, b) A side on view of the microcavity structure.

2.2 Experimental setups

2.2.1 Sample cooling

Flow cryostats are used for all experiments, with the sample(s) adhered to a copper plate, as shown in figure 2.2. The cryostat sealed and the air evacuated from the system using a vacuum pump, reaching an air pressure of the order of 10^{-6}mbar. A dewar filled with liquid helium (LHe) is connected to the cryostat, and a second vacuum pump connected to the cryostat pulls LHe through and lowers the temperature of the *cold finger*. The cold finger is a long piece of copper that extends towards the sample, providing thermal contact and cooling the sample to approximately 10K. A temperature sensor is attached to monitor the temperature of the cold finger. The LHe that passes through the cryostat is recycled for use later.

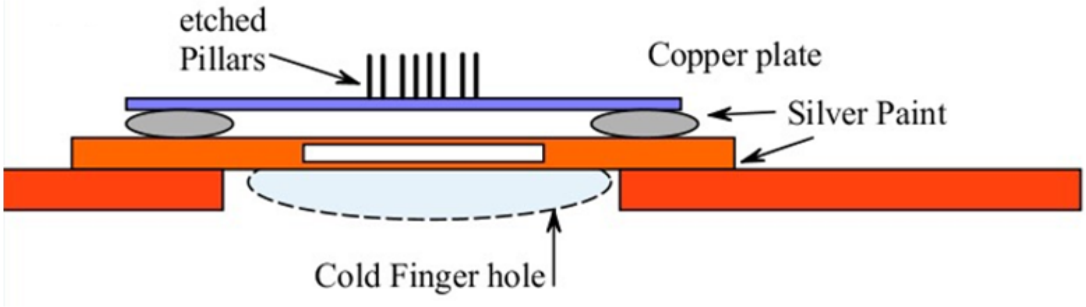

Figure 2.2: The sample mount would be attached to the cold finger of the flow cryostat.

2.2.2 Excitation optics

All experimental results in this thesis used transmission or a reflection excitation. In transmission, the excitation laser scatter can be suppressed when collecting at an angle. The sample can be mounted such that the etched side of the sample is facing the incoming laser or reversed.

For measurements performed in chapters 3 and 4, a laser was directed onto the sample using a 4 mm focal length (f) objective with a numerical aperture (NA) of 0.42. An f=10mm microscope objective collects the light with NA=0.6 placed at the backside of the cryostat.

In chapter 5, a camera objective with f=50mm with large NA is placed in excitation. An f=10mm microscope objective with NA=0.6 placed in the collection path. In each of the subsequent chapters, a schematic is shown alongside the experiment.

2.2.3 Sample excitation

For non-resonant photoluminescence (PL) measurements, a continuous-wave (CW) laser is positioned far above the UPB energy. The CW laser is focused through the excitation objective, with polaritons emitting light at lower energy. An objective placed in front collects and collimates light along the optical axis.

Different optical apparatus is used on the collection side depending on the measurement—experiments in this thesis use either real- or Fourier-imaging. A long-pass filter is used, 800 nm or 850 nm, which filters the excitation laser.

In chapters 3 and 4, the CW laser used was a coherent MBR-110; the laser light is polarised, so the linear polarisation can be controlled using a half-wave plate (HWP). A tunable mode-locked Ti:Sapphire laser with an 80MHz repetition rate and ∼100ps pulse length was used to excite polaritons resonantly. The laser can operate over a wide bandwidth of 700-1080 nm. A Faraday isolator is placed at the output of the laser cavity; this component is essential to avoid reflections going back into the cavity.

The laser pulse waveform is checked using an oscilloscope connected to a photodiode. An auto-correlator is used to estimate the laser pulse length to calculate the peak number of photons/polaritons. A combination of an HWP and a linear polariser (LP) is used in the excitation path to control the power. A power meter measures the average power per second. After the LP, an additional HWP or quarter-waveplate (QWP) may be used to control linear/elliptical/circular dependencies.

The optical table is enclosed, with protective goggles worn when lasers are used.

2.2.4 Fourier- and real-space imaging

The PL emission is imaged onto the entrance slit of a HORIBA TRIAX 550-series spectrometer equipped with a 1200 gr/mm grating resolution of 0.03 nm. One of the exit ports goes to a Princeton Instruments PIXIS 1024x1024 pixel charge-coupled device (CCD) with a pixel size of $13\mu m$. Figure 2.3 is a schematic of the spectrometer used.

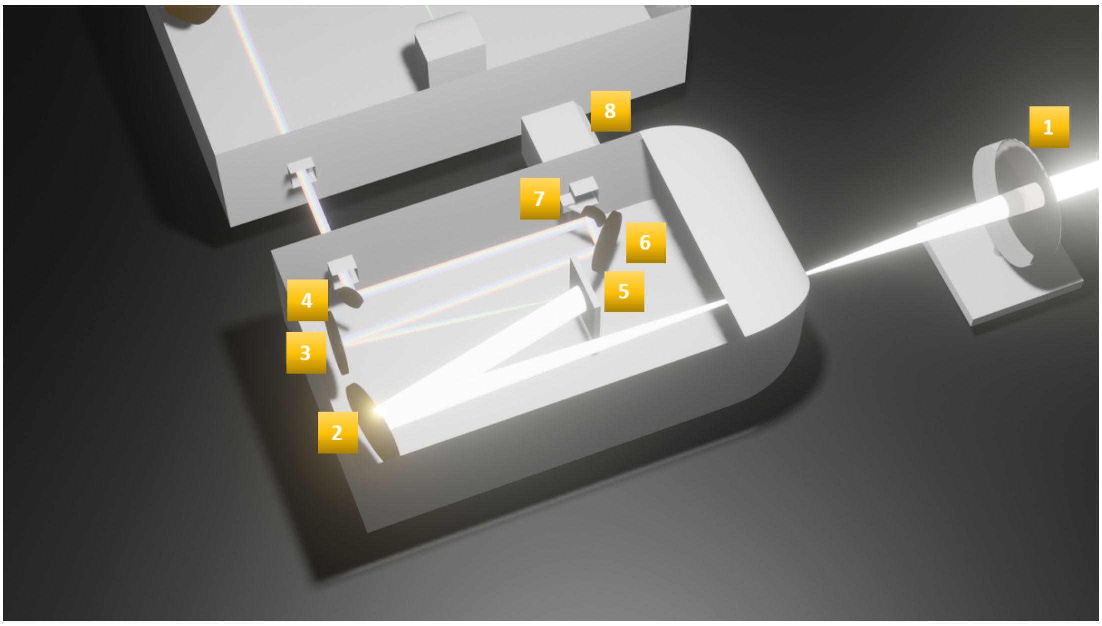

Figure 2.3: A schematic of the spectrometer used for Chapters 3 and 4. (1) A focusing lens on a motorized translation stage. (2,3) A parabolic mirror. (4, 6) Mirror. (5) Grating. (7) A motorized mirror allows light to be sent to the CCD or an output slit (in this configuration, the light is going to the output slit). (8) The CCD.

The light is directed onto the CCD (8), what is imaged depends on the optics placed before the spectrometer. A schematic of the real- and Fourier-space collection is shown in figure 2.4. The collection MO and the final lens will produce an image with magnification f_{il}/f_{cl}, where f_{il} is the final lens focal length and f_{cl} is the microscope objective focal length. By placing two additional lenses (plano-convex) in-between MO and the final lens, this will again produce a real space image, as shown in figure 2.4a. The magnification that results will be $\frac{f_1}{f_{MO}} \cdot \frac{f_{fl}}{f_2}$, so one can choose the appropriate magnification to either increase or decrease the feature size.

A Fourier-space image is formed on the back focal plane of the collection lens. Light from the sample that is emitted at the same angle is focused on this spot in the Fourier plane, as shown in figure 2.4b. An additional two lenses can be placed in figure 2.4b to either increase or decrease the size of the Fourier space image, referred to as the *zoom*. Fourier-space imaging is sometimes called; far-field, momentum-space and k-space imaging. This type of imaging gives information about the in-plane momentum of polariton modes emitted from the cavity. Each of the angles emitted gives a different in-plane momentum value, and when resolved in energy, the dispersion relation of polariton modes is visualized.

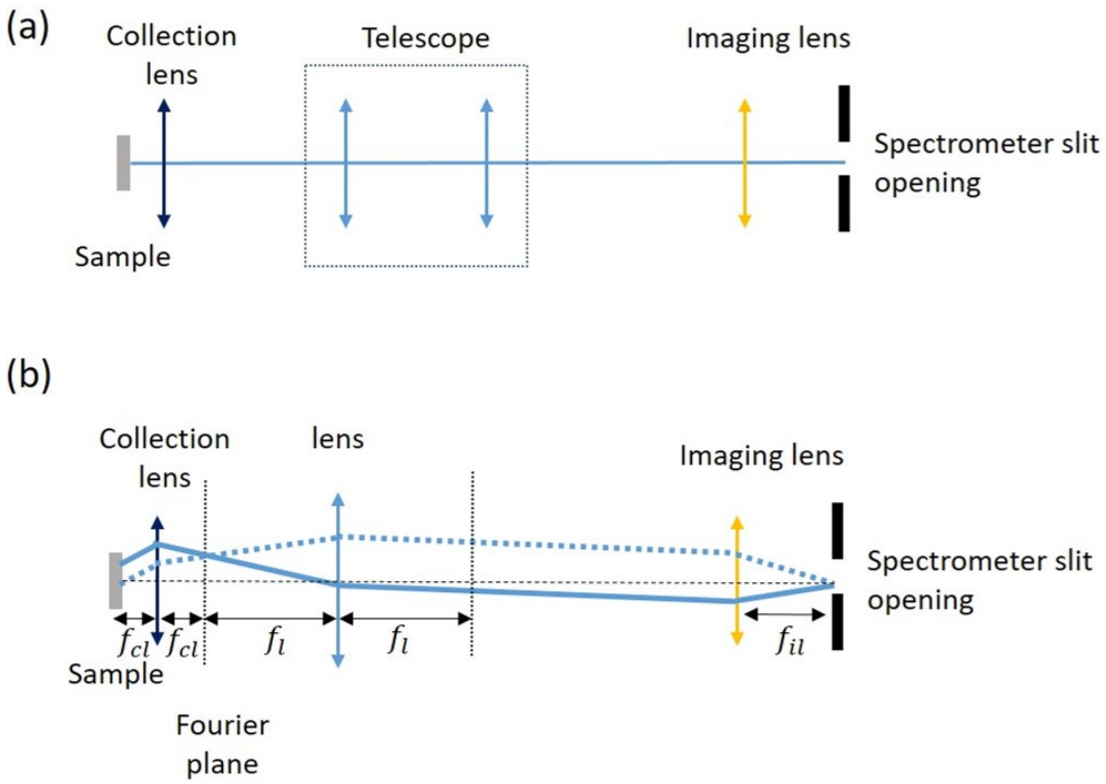

Figure 2.4: The simplest schematic for real (near-field) and Fourier (far-field) space imaging. a) PL from the sample is collimated using a collection lens (microscope objective), the emissions can be expanded or shrunk using a telescope (two plano-convex lenses) and focused onto the entrance of a spectrometer. b) PL emitted at the same angle is focused onto the same position in the *Fourier plane*, placing two lenses after the lens (not shown) can expand or shrink the image. Light emitted at the same angle is focused onto the sample position on the entrance of the spectrometer slit; this technique allows one to see the dispersion of the polariton modes, see figure 2.8.

2.2.5 High angle excitation

High angle excitation is an experimental technique used in chapter 5. Instead of exciting the sample at a normal incidence with in-plane wavevector $k_{||} = 0$, the path is horizontally offset to excite the sample at a finite angle Θ_x. The horizontal offset means that the excitation optic needs a large aperture to allow the laser light to get to the sample. The horizontal offset required to excite the sample at a given angle or in-plane wavevector can be found using the focal length f and the laser position offset from normal incidence Δx. Figure 2.5 shows the real experimental equipment, and a schematic.

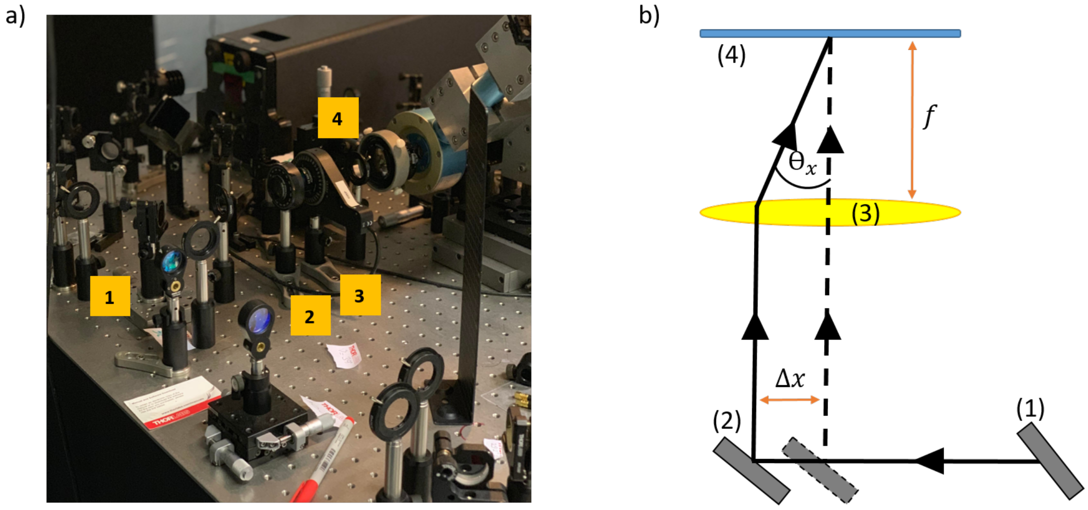

Figure 2.5: The experimental table for the high angle excitation in chapter 5 and to the right is a schematic of the adjustable mirror to create the desired angle. a) The experimental setup: 1) a mirror mounted on a translation stage 2) Linear polarizer 3) Half-wave plate 4) Excitation Objective $f = 50mm$. b) The schematic for angled excitation: 1) Mirror 2) Mirror mounted on a translation stage, the dashed and solid lines show two potential positions on the translation stage 3) excitation objective 4) sample surface.

This technique is used in chapter 5 to excite the **K** and **K′** point of the Brillouin zone of a honeycomb lattice. When exciting at normal incidence, the **Γ** point of the lattice can be excited at the lowest energy of the lowest energy band. Using non-resonant excitation and Fourier space imaging, the full Brillouin zone of the honeycomb lattice can be shown. This information can be used to approximately calculate the Δx required to excite the K and K' points. With the Δx given by:

$$\Delta x = f \tan(\Theta_x). \tag{2.1}$$

2.3 Light Modulation

Chapters 3 and 4 use an electro-optical modulator that changes the polarisation of the incoming light to the sample in a controlled way. In the same chapters, a CW-laser is changed into a pulsed-laser, with components are listed for achieving this.

2.3.1 Electro-optic modulator

Experiments performed in chapter 4 use an electro-optical modulator (EOM), a device which allows for the controlled output of the direction of linear polarisation with an applied electrical bias to the device. The device contains two matched lithium niobate crystals, when an electric field is applied to the crystal the indexes of refraction change. The device behaves as a HWP on a linear input state. A signal generator applies a high and low voltage, shown as a square wave in figure 2.6. This voltage biases the EOM, modulating the input into two orthogonal polarisations.

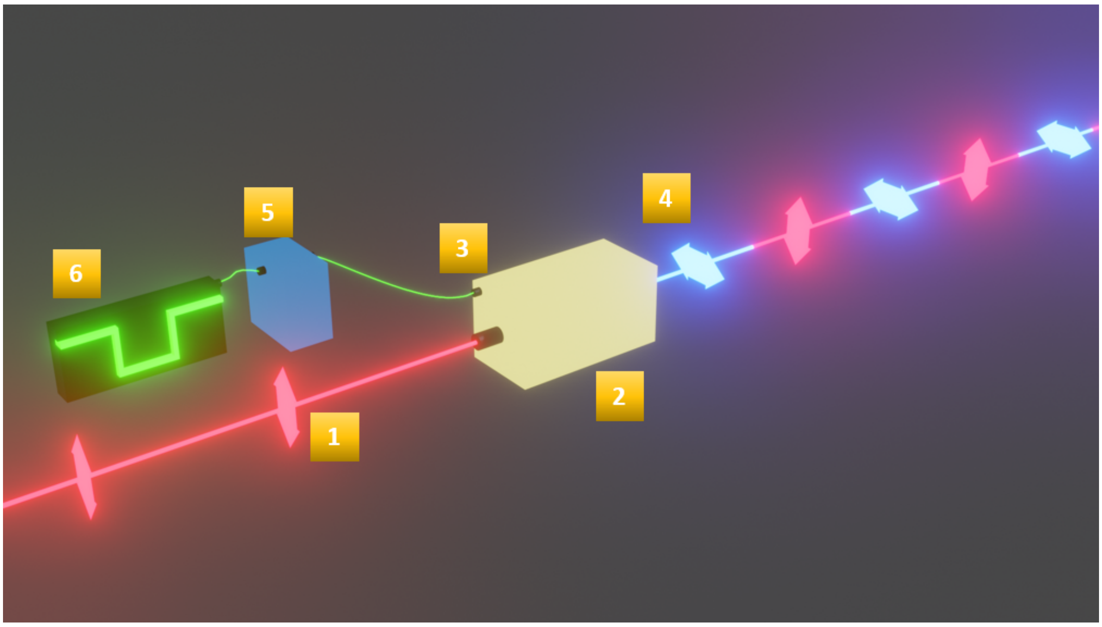

Figure 2.6: Operation of the EOM, a high and low voltage is applied (square wave) and biased onto the EOM. (1) Incoming vertically polarised light. (2) EOM. (3) Bias input (rf). (4) Horizontally polarised light. (5) Bias controller. (8) Signal generator.

2.3.2 Pulsar

Experiments performed in chapters 3 and 4 used a Pulsar designed by iXblue. The device allowed for a CW laser to pulse over a range of pulse lengths see figure 2.7. The laser is locked to a reference's repetition rate, an 80MHz Ti:Sapphire laser. The pulse lengths are measured on a streak camera (Hamamatsu), the results of which are shown in figure 2.7.

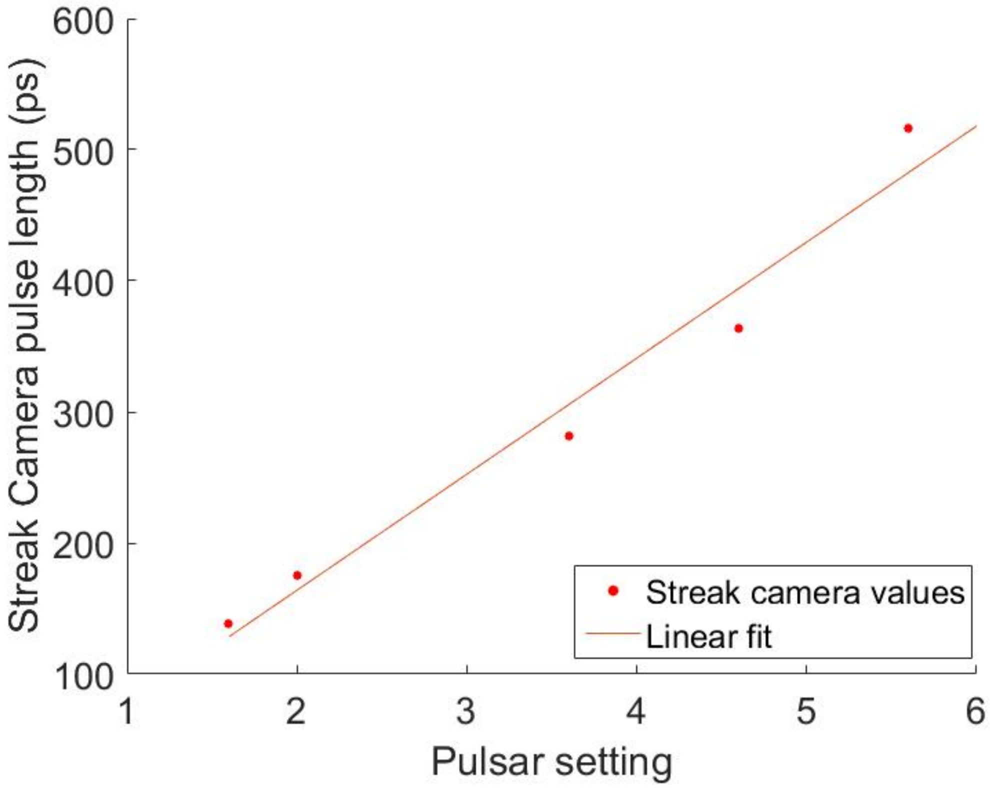

Figure 2.7: Streak camera pulse length is measured for a given pulsar setting.

A sequence of electronic components has to work together to achieve the desired pulsed output:

1. A reference signal is taken from the output of the Ti:Sapphire laser control box.

2. This signal is split on an oscilloscope as it will be used for CW to pulsed light and also for triggering photon counting software
3. One signal goes to an iXblue DR-PL-10-MO driver, the driver is connected to a power supply and a NIR-MX800-LN-10 Modulator.
4. A linear polarisation maintaining optical fibre is connected to the modulator, and the CW laser is focused onto this fibre.
5. The modulator is connected to an iXblue MBC-DG-LAB bias controller, which has several inbuilt automated programs for minimising or maximising the output power from the modulator. The bias controller is a critical piece of equipment, avoiding voltage drift and allowing consistent output power and pulse length times.
6. All the components are now in place, so the CW laser should now be able to pulse at the repetition rate of the reference laser.

2.4 Sample characterization

Non-resonant excitation on an unetched region of the microcavity is the easiest way to get quantitative information about the Rabi-splitting and exciton-cavity detunings. Fourier space photoluminescence (PL) is focused onto the narrow slit entrance of the spectrometer, and due to the variation in cavity length, the cavity-exciton detuning changes throughout the whole sample. Collecting a Fourier space image gives information about the in-plane momentum of the polaritons. Using the spectrometer grating allows for the resolving of energy and momentum. The Fourier space image collected is imported into Matlab, and data is analysed using the peak intensity values to extract the energies of the UPB and LPB. An example of the fitting procedure is shown in figure 2.8. Where one axis shows the angular emission of the polaritons, given by $k_{||} = \frac{2\pi}{\lambda} sin\theta$ vs energy.

The fitting process extracts the LPB and UPB from the raw data, where the Rabi-splitting Ω can be estimated by least squared fitting using all available $k_{||}$ values. The linewidth is given by the full-width at half-maximum (FWHM) of a fitted Lorentzian peak at $k_{||} = 0$.

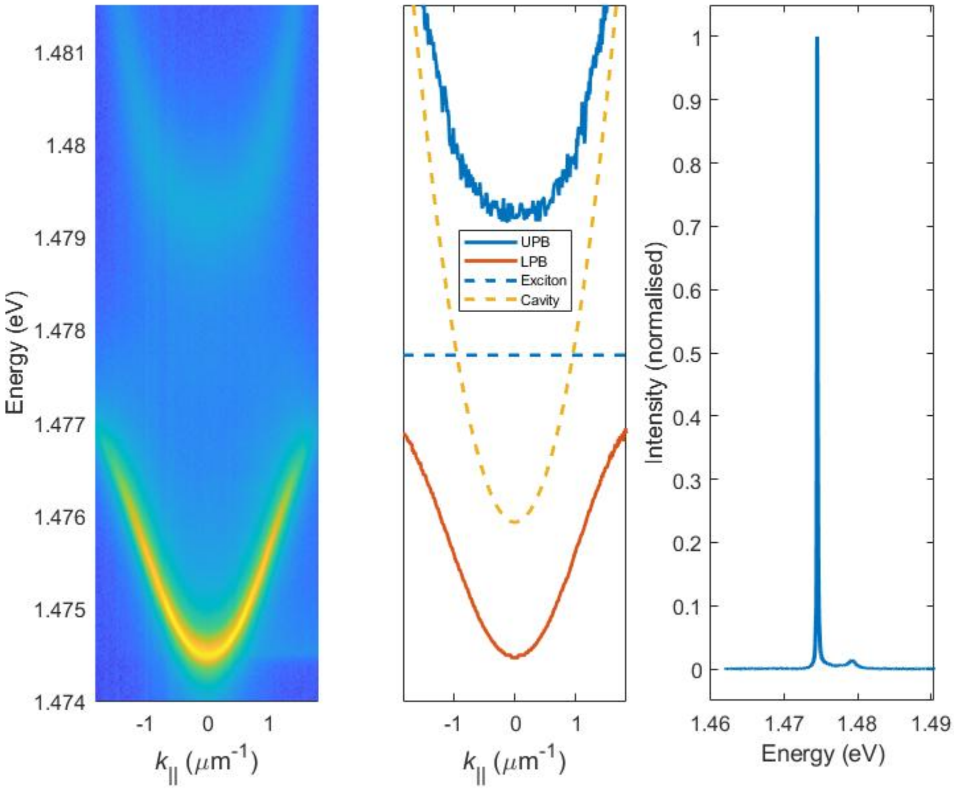

Figure 2.8: Planar microcavity dispersion characterisation. a) Energy vs in-plane momentum log(raw intensity). b)The peak intensity extracted for the LPB and UPB with exciton and cavity lines fitted. c) $k_{||} = 0$ line intensity. $\Omega = 4.42$meV, exciton-cavity detuning -1.80 meV, $\gamma = 123\mu eV$ and Q=12001.

2.4.1 Tomographic scans

Tomographic scans show a complete real-space and momentum profile of polariton emission. The procedure is straightforward but requires automation if one wants to extract multiple different parameters in as little time as possible. In figure 2.3, a lens mounted on a translation stage can move the image to the left or right of the spectrometer entrance slit. Considering real-space PL emission, the energy and intensity can for a given y-positions are recorded. The lens begins at position $x = x_1$, moved a defined number of steps until reaching $x = x_n$, where n slices are used to construct the (E,x,y) spatial profile.

The same method can be used in the far-field collection to show the momentum profile at an energy in the microcavity. In chapter 5, the $\mathbf{K}$, $\mathbf{K'}$ and $\mathbf{\Gamma}$ points of a honeycomb lattice's first and second Brillouin zone are presented.

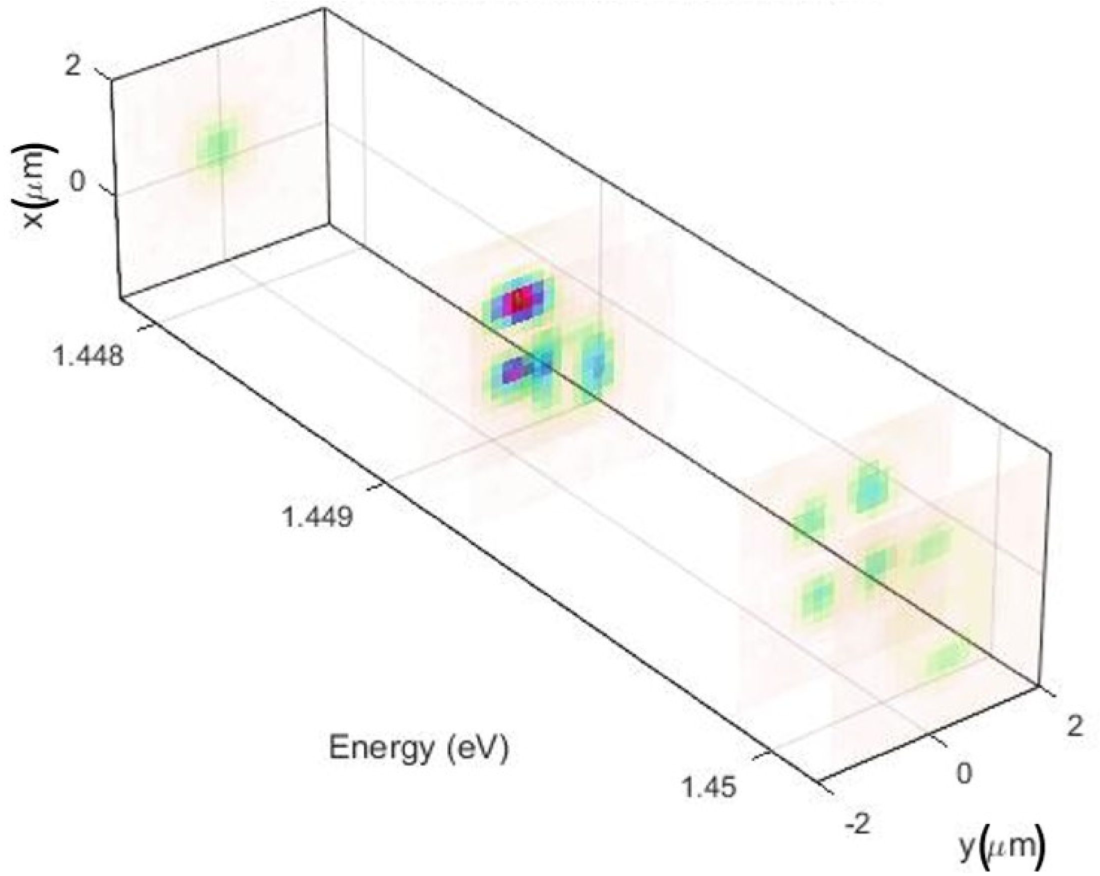

Figure 2.9: The spatial and energy profile of a 5μm square micropillar device. Multiple modes are visible, which can be selected at a given energy.

2.4.2 Polarisation metrics

Excitation and collection of linearly polarised light are calibrated with polarising beam splitters (PBS), where the light transmitted and reflected from the PBS has orthogonal polarisation. Using a thin film linear polariser (LP) to match the PBS in either transmission or reflection will calibrate it with a known polarisation. A HWP can rotate the linearly polarised light, while QWP's are used to obtain right- or left-handed circularly polarised light. A thin film LP of known polarisation direction is placed in the collection path before the final lens, and a HWP or QWP or both are placed before this LP. In this configuration, the three *Stokes parameters* can be measured. Mounting the HWP and QWP on automated rotation stages can be controlled with Matlab to select specific angles that allow a chosen polarisation output.

More metrics are available to use, such as the *degree of linear polarization* (DLP), given by $\sqrt{S_1^2 + S_2^2}$. Also, the *linear polarization angle* (LPA), given by $\psi = arctan(S_2/S_1)$. The LPA allows visualisation of the TE-TM field and will be used to provide experimental proof of a Dresselhaus type field in chapter 5.

Chapter 3 will use two APDs to detect photon count differences, with the arms collecting orthogonal polarisations, the S_2 parameter is used to track the sensitivity of our measurement.

2.5 Polariton number calculations

Several steps must be considered to estimate the number of polaritons inside the cavity. Considering the energy E_{cav} within the DBR stacked microcavity. The top mirror, where the laser beam is incident, is DBR1, and the bottom mirror, through which the light is transmitted towards the detectors, is DBR2. The cavity is pumped continuously by a monochromatic light source to reach a steady state and contain constant energy. E_{cav} and round-trip transmitted fraction through DBR2 leads to the overall cavity power transmission, which is measured at the output by using a power meter.

The relationship between the E_{cav} and the polariton number is:

$$E_{cav} = \hbar\omega N_{pol}, \tag{2.2}$$

where $\hbar\omega$ is the polariton energy and N_{pol} are the number of polaritons. This expression is related to the output power by:

$$P_{out} = \hbar\omega N_{pol}\eta\gamma_{DBR}, \tag{2.3}$$

where P_{out} is the overall cavity power transmission, η is the mirror asymmetry factor that characterises the transmission through the mirror on the detection side, compared to the total cavity losses due to non-unity reflection of the mirrors. γ_{DBR} is photon cavity mode linewidth.

γ_{DBR} is a quantity for a pure photon circulating inside the cavity. Introducing photon-exciton strong coupling means that a $|C|^2$ fraction of photons are circulating, which is the photonic Hopfield coefficient. The energy and transmitted power will then be related by:

$$E_{cav} = \frac{P_{out}}{\eta\gamma_d}, \tag{2.4}$$

where $\gamma_d = \gamma_{DBR}|C|^2$, which accounts for broadening in linewidth caused by entering the strong coupling regime.

Chapters 3 and 4 use the same sample provided by C2N. They measured γ_{DBR} at a large negative detuning on the planar microcavity before it was etched into pillars, reporting a value of $\gamma_{DBR} = 20 - 30\mu\text{eV}$. Simulations obtain $\eta = 0.536$ since it depends only on the ratio of mirror transmissions.

In practice, the excitation energy is required along with the transmitted laser power. The spectrometer resolves the energy, while a power meter measures the output power on the transmission side of the cryostat.

Finally, remarking on the relation between average power for CW excitation and pulsed excitation.

$$P_{peak} = \frac{P_{out}}{f\Delta t}. \tag{2.5}$$

P_{peak} is the peak optical power, f is the repetition rate, and Δt is the pulse length. The denominator is referred to as the Duty Cycle.

2.5.1 Hopfield coefficients

This section concerns the micropillars discussed in chapters 3 and 4 only. To calculate the peak or average number of polaritons in the resonant transmission experiments, the photonic and excitonic fraction must be estimated. A Rabi-splitting $\Omega_{Rabi} = 3.5\text{meV}$ was measured on a planer dispersion before the sample was etched at the C2N facility. Using this value, we extract the exciton fraction by looking at the splitting between purely photonic E_{11} and E_{12} modes. The energies we calculate during non-resonant PL are then used to estimate the exciton fractions for a respective mode. Figure 2.10 shows the exciton fraction estimates. The values for the relevant micropillars are displayed in the table 2.1. The coefficients are extracted from the equation:

$$|X_{nm}|^2 = \frac{(\frac{1}{2}\Omega_{Rabi})^2}{(\frac{1}{2}\Omega_{Rabi})^2 + (\Delta E_{nm})^2}. \tag{2.6}$$

Where $|X_{nm}|^2$ is the exciton fraction and ΔE_{nm} is the E_{nm} mode detuning from the exciton.

Micropillar	$\mathbf{|X_{11}|^2}$	$\mathbf{|X_{12}|^2}$
Chapter 3	0.13	0.21
Chapter 4 pillar A	0.09	0.15
Chapter 4 pillar B	0.25	0.42

Table 2.1: Micropillar exciton fractions.

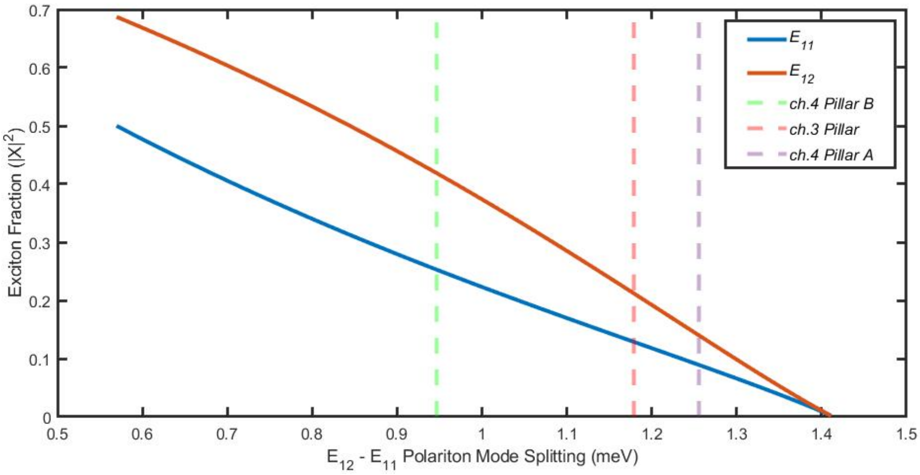

Figure 2.10: Exciton fractions calculated from the $\Omega_{\mathrm{rabi}} = 3.5$meV splitting provided by C2N. See table 2.1.

Chapter 3

Polariton micropillar photon statistics in pump-probe configuration

3.1 Motivation

On-demand single photons are a vital ingredient for quantum technologies, where a wavepacket contains exactly one photon in the quantum state. The purity of the state is an essential aspect needed to demonstrate photon-photon gates and interference results with high fidelity.

Since sodium atoms were shown to produce single-photon in an atomic energy transition [100], albeit with low efficiency, cold atoms gathered attention as a candidate as a source of single-photons. As of today, cold atoms can produce on-demand single photons with near-indistinguishable photons [101]. A lingering problem with cold atom approaches is the set-ups, and low operation rates [102]. Spontaneous parametric down-conversion is another process used to generate single photons and entangled photon pairs [103] though this process is not efficient. The leading solid-state approaches are as follows.

Two-dimensional materials that host quantum defects [104]; the emitter is embedded in a monolayer, and extraction efficiency can be especially high, shown to operate on MHz-repetition rates [105]. Another system are colour centres in crystals, with diamonds being the most studied host, along with nitrogen- and silicon-vacancies [106]. The most comparable system to the contents of this chapter are quantum dots, with self-assembled InAs/GaAs QDs having the leading single-photon source performance [107, 108]. Under resonant excitation $g^{(2)}(0) < 0.01$ has been demonstrated. QDs have been implemented in waveguides and have been operated with Purcell-enhancement to reduce lifetimes as low as 22.7ps [10]. Key challenges remain for InAs QDs: reproducibility of the samples, growth of multiple identical dots and site-control placement of QDs.

Polaritons have a rich history of nonlinear optical phenomena, it has only been in the previous five years that emergent quantum effects have progressed. The significant factor leading to these effects has been the fabrication and optimisation of quantum well layers grown inside microcavity. The work of Delteil and Imamoaglu [31] was discussed in chapter 1, where an open cavity polariton mode was excited. Measuring the photon statistics leaving the cavity, see figure 1.22, they were able to achieve $\sim 5\%$ anti-bunched light leaving the cavity. This is the leading value for polariton anti-bunching using the conventional photon blockade approach.

Around the same time, Munoz-Matutano and Voltz et al. [40] demonstrated a similar level of anti-bunching. They use a mechanically tunable fibre cavity with a quantum well coupled to the cavity. Both approaches looked to reduce the decay rate κ in the microcavity and decrease the mode volume, showing that polaritons can enter the quantum regime. However, this is far from the values required for applications [102]. The conventional blockade approach reaches a limit as the microcavity structures approach the best possible condition.

The parametric blockade is another approach to achieving anti-bunched light. Kyriienko and Liew [1] proposed this for dipolaritons in a three-mode system, where each of the modes is coupled by a weak nonlinearity. Although the authors used dipolaritons to analyse the expected values for anti-bunched light, they noted that systems, where parametric scattering is possible might use this approach. Parametric scattering has been studied in planar semiconductor microcavities [42] and in 0D structures [109]. In the parametric scattering process, signal and idler modes are generated from the pair scattering from the pump. The initial pump energy and in-plane wavevector are given by, E_p and $k_{p,||}$. Figure 3.1 shows three levels equally spaced in energy, where parametric scattering results in signal and idler states forming at the energy levels E_1 and E_3.

Parametric scattering causes the population of the E_1 and E_3 to increase, while the population of the E_2 mode decreases. The population of the signal and idler

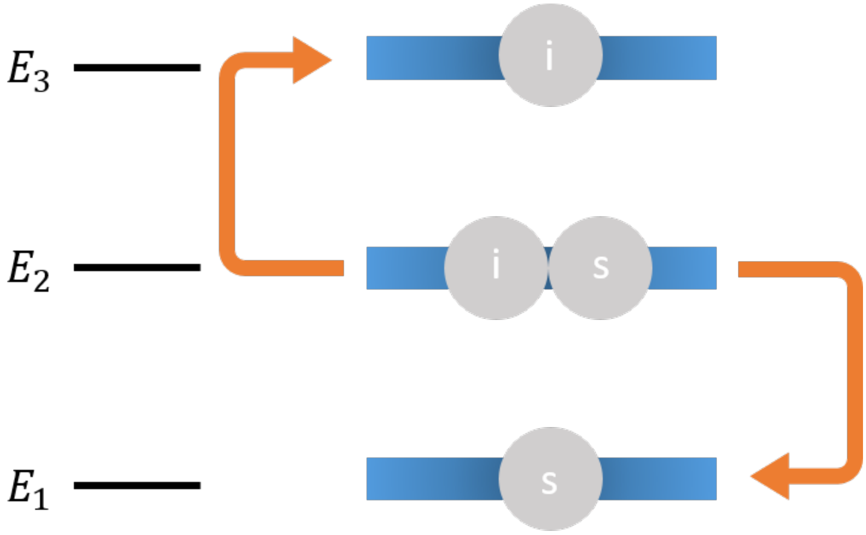

Figure 3.1: Parametric scattering of two polaritons at energy E_2 (pump energy) to signal and idler states E_1 and E_3. Here $E_2 - E_1 = E_3 - E_2$.

states in parametric scattering have a quadratic dependence on the pump population. For Bosonic systems, *seeding* a population in E_1 (signal), the parametric scattering process can be enhanced. Going beyond a quadratic dependence to where *stimulated scattering* is observed [110]. The signature of stimulated scattering is an exponentially increasing population in the signal and idler state, with a reduction in mode linewidth. The *parametric blockade* relies on limiting the population of the E_2 mode, with two particles undergoing parametric scattering if two particles are in the mode.

The linewidth and the nonlinear energy shift of polaritons make the conventional blockade difficult. In GaAs based QWs, the exciton-exciton interaction is $g_X \sim 10\mu eV \mu m^2$. When this nonlinearity is large compared to the decay rate κ, the second-order coherence theoretically will approach $g^{(2)}(0) = 0$, see figure 1.21. In micropillars, to achieve sufficient $\frac{U}{\kappa}$ would require a sub-micron pillar diameter, where U is the nonlinear energy shift. As the diameter of micropillars decreases, the decay rate κ increases. The polariton linewidth is a good indicator of the decay rate κ, with a larger linewidth implying a faster decay rate and a lower quality factor.

Polariton micropillars are not yet suitable for the conventional blockade, however, the energy spacing between respective modes can be approximately equal. With the observations of parametric and stimulated scattering reported, we do a preliminary study of the parametric blockade approach in a micropillar setting.

In this section, tomographic scans will reveal individual micropillars' spatial and energy profiles, with appropriately spaced energy micropillars chosen for parametric scattering. In the parametric scattering experiment, a pulsed laser excites the middle mode, E_2, and photon counts are accumulated in the E_1 and E_3 mode. Next, a second laser is introduced, which will populate the E_1 mode and stimulates scattering into the E_1 and E_3 mode. A small number of polaritons are injected into the E_2 mode while strongly exciting the E_1 mode. The light emitted from E_2 mode is analysed in a Hanbury-Brown and Twiss (HBT) interferometer, where the second-order coherence function $g^{(2)}(\tau)$ is measured. The $g^{(2)}(0)$ value is measured for a red, resonant and blue detuning from the E_2 mode. Even though the micropillar selected was appropriate for observing parametric scattering, especially when compared to other devices reported [109], it was not observed in our device. Enhanced scattering into the idler mode was seen when introducing a seeding population of polaritons into the E_1 mode. The E_2 mode light was analysed in the HBT interferometer, where no evidence of anti-bunched light was observed.

3.2 Low dimensional polariton confinement

Over the past 15 years, confining polaritons has been a growing field of interest. Moving from planar to lower dimensions lifts translational invariance, wavevector selection rules are relaxed, which leads to more efficient build-up for polaritons at lower energy states. Groups started by looking at 0D structures like circular and square pillars before moving to 1D chains and 2D geometries. Two approaches have been used to lower the dimensionality of the system: *surface acoustic waves* (SAW) and *lateral confinement.*

SAWs are acoustic waves that travel on the surface of the sample, creating a periodic potential through mechanical stress. When the amplitude of the SAW energy modulation is sufficient, the 2D system transitions to a 1D system[111].

The second approach confines the photonic component of polaritons [112]. By depositing periodic strips of metallic thin films on the surface of the sample, the boundary conditions on top of the DBR lead to a higher cavity photon resonance energy, trapping the lower polaritons [113] - leading to 1D confinement. Alternatively, the cavity can be etched instead of depositing material onto the surface, this creates localised regions on the cavity with different surface heights, then depositing the top DBR. Areas in the cavity will have different lengths, with the more extended regions having a lower cavity mode energy, creating trapping potentials. These are referred to as mesas and have been investigated in 1D [114] and 0D [115] structures.

The method used in this thesis is to etch through the layered microcavity structure until reaching the substrate. Many different groups have employed this approach on GaAs based samples that have been used to create 2D, 1D and 0D structures. The introduction discussed a 1D chain of coupled polariton micropillars, producing a 0D topologically protected mode localised on one lattice site. Later, the

1D topological edge state was realised in a 2D geometry of coupled micropillars. The building block of these structures is 0D micropillars. The following section will discuss the energy profile of the micropillars used.

3.3 Characterisation of micropillars

The modes of micropillar devices are characterised using non-resonant photoluminescence (PL). Devices are excited using a continuous wave laser with a Gaussian spatial profile. The emitted light from the device resolved in energy and position. There are square and circular pillars, ranging from 2.6 μm to 5 μm in diameter. The PL is used to compare the energy spacings and select devices for testing which have approximately equal mode spacings. The square micropillar devices have a complex structure, not a simple three-level system. The main differences are that; there is a polarisation splitting for each mode, and there is a different spatial profile for each mode of the micropillar device. Tomographic scans show the spatial profile for square micropillars.

3.3.1 Size dependence of micropillars

A planar cavity is etched into square and circular shapes, and the top and bottom DBRs form a pillar. The significant difference between the refractive indices of the cavity layer and the surrounding air leads to strong lateral confinement of photons via total internal reflection. Quantising both the longitudinal and transverse wave vector for photons inside the pillar. This three-dimensional confinement, in theory, leads to the formation of equally spaced modes in the cavity. Figure 3.2 is an SEM image of the square micropillar devices on our sample. Micropillars are often referred to as a 'photonic atom' or 'Photonic dot', akin to energy levels in an atom. The strong coupling between excitons and photons means we deal with confined polaritons, with the 0D discretised photon modes coupling to the 2D exciton states. As the energy increases, so does the kinetic component. When the kinetic is similar to the barrier potential, the mode confinement disappears.

There are many pillars available for testing, with the sample having an exciton-cavity detuning gradient in both the horizontal and vertical direction for positions on the sample. Using a micropillar with a large negative detuning will allow us

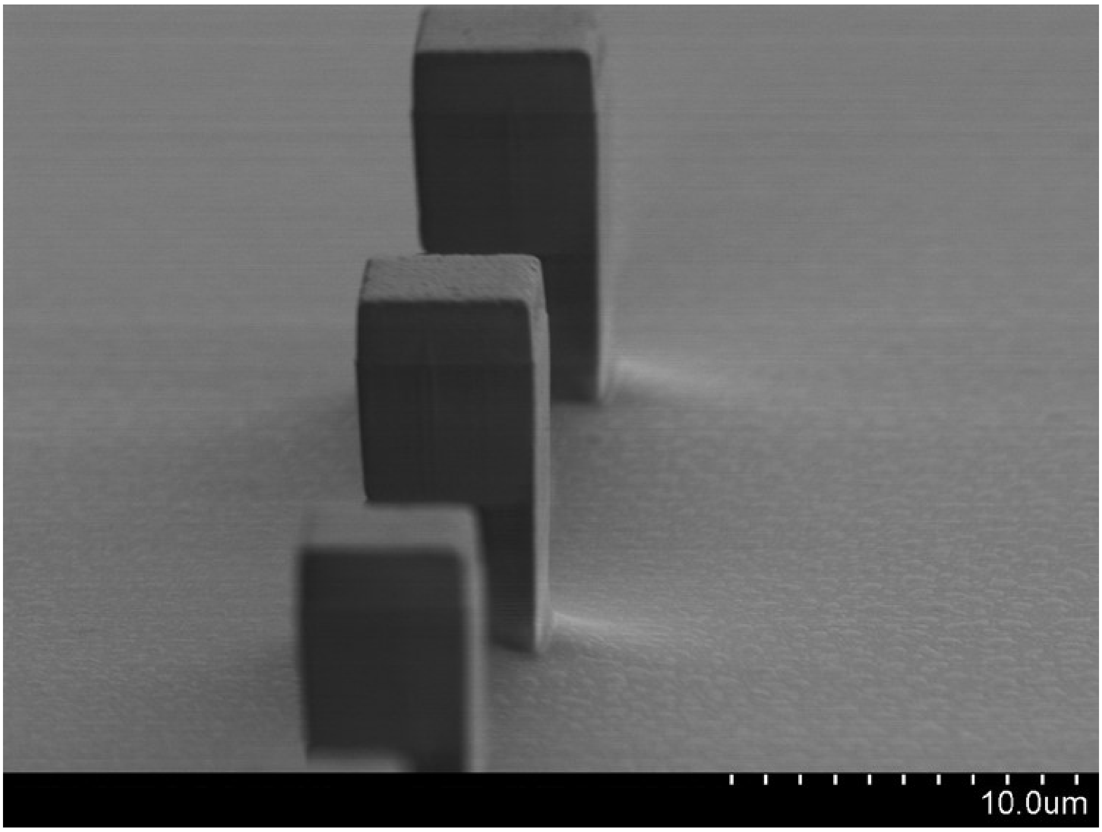

Figure 3.2: A scanning electron microscope image of square micropillar devices on our sample. Image provided by C2N.

to see the mode structure of the system, pillar *set one* provides this. The light emitted from the square micropillars is imaged using near-field collection optics, the position and energy are shown in figure 3.3(a-c). These micropillars are positionally close, with the maximum distance between $2.4\mu m$ and $5\mu m$ diameter pillar being $\approx 100\ \mu m$. Working in this small region, we can see that reducing the pillar size; increases the mode energy value for E_{nm} and increases the nearest-neighbour mode distance.

The confinement energy becomes so strong that some modes are no longer visible and are absorbed into the broad exciton region. The emission intensity is different for each mode in figure 3.3, this is because of the different photonic fractions of the confined states and thermalisation toward the lower energy states[116]. Pillars tested in less negatively detuned sample regions show a closer mode separation. More details about the size dependence and how it affects the photonic confinement are explained in T. Gutbrod et al. [117].

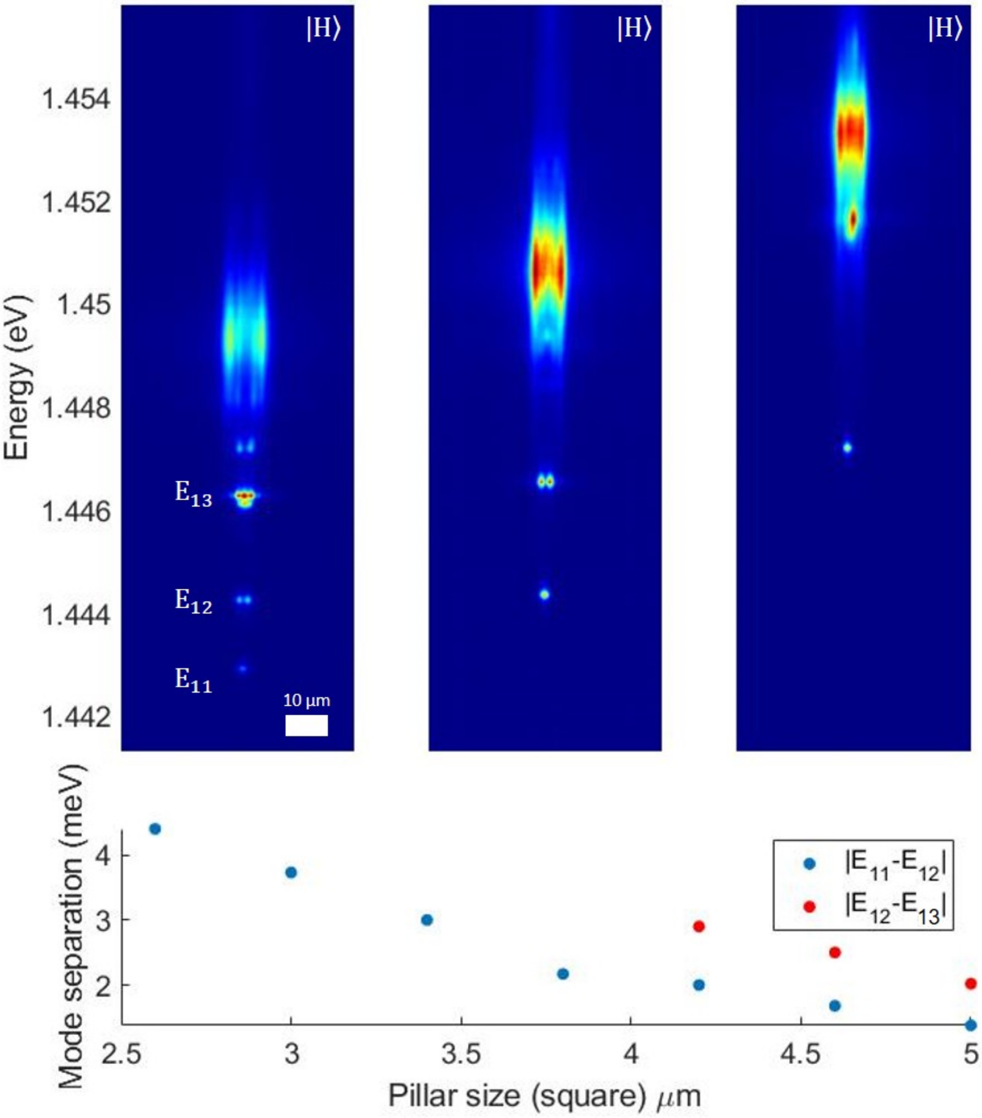

Figure 3.3: Real-space imaging of three different sized square micropillars. a)PL of 5 μm pillar set 1. b)PL of 3.8 μm pillar set 1. c)PL of 2.4 μm pillar set 1. d) Mode separation between E_{11}, E_{12} and E_{13}.

3.3.2 Tomographic scans

Tomographic scans are technique explained in the methods section , which are used to analyse the shape of the square micropillar modes. A 2D spatial map of a 5 μm square pillar is shown in figure 3.4. The cuboid geometry of the potential produces modes of Hermite-Gauss nature, which has a different form to the cylindrical potential, which are Bessel-like[117].

The first polariton mode E_{11} has a symmetric Gaussian profile, while the second excited modes E_{21} and E_{12} are localised in two directions which is reminiscent of p_x and p_y orbitals. The most intense counts are within the pillar, outlined by the white square in each sub-figure. As the mode energy increases towards E_{22} and onwards, emission outside the pillar is seen, which is likely due to defocusing on the collection objective.

As discussed in the methods section, placing a half-wave plate and linear polariser in the collection path resolves the polarisation of the emission. Selecting a horizontal, vertical, diagonal and anti-diagonal basis. Figure 3.5a shows the collection configuration for the slit position. When looking at the E_{12} mode, there is a small polarisation splitting for the basis measured, with the maximum splitting of approximately 62 μeV. Noting that when the slit is positioned at x=0, the E_{21} mode is not visible. Figure 3.5c shows the integrated polarisation for the midpoint between the E_{12} and E_{21} mode, 1.192 μeV above the E_{11} mode.

The tomographic scans were essential for determining the shape of the modes and correctly shaping the incident laser's spatial profile to match the chosen mode. The E_{12} is the mode selected to be our middle energy mode, which would be the *pump* mode for parametric scattering. Looking back at figure 3.4, the shape of the spatial profile of the laser beam was changed to resemble the E_{12} state. This shape is achieved by inserting a phase mask at the centre of a telescope in the

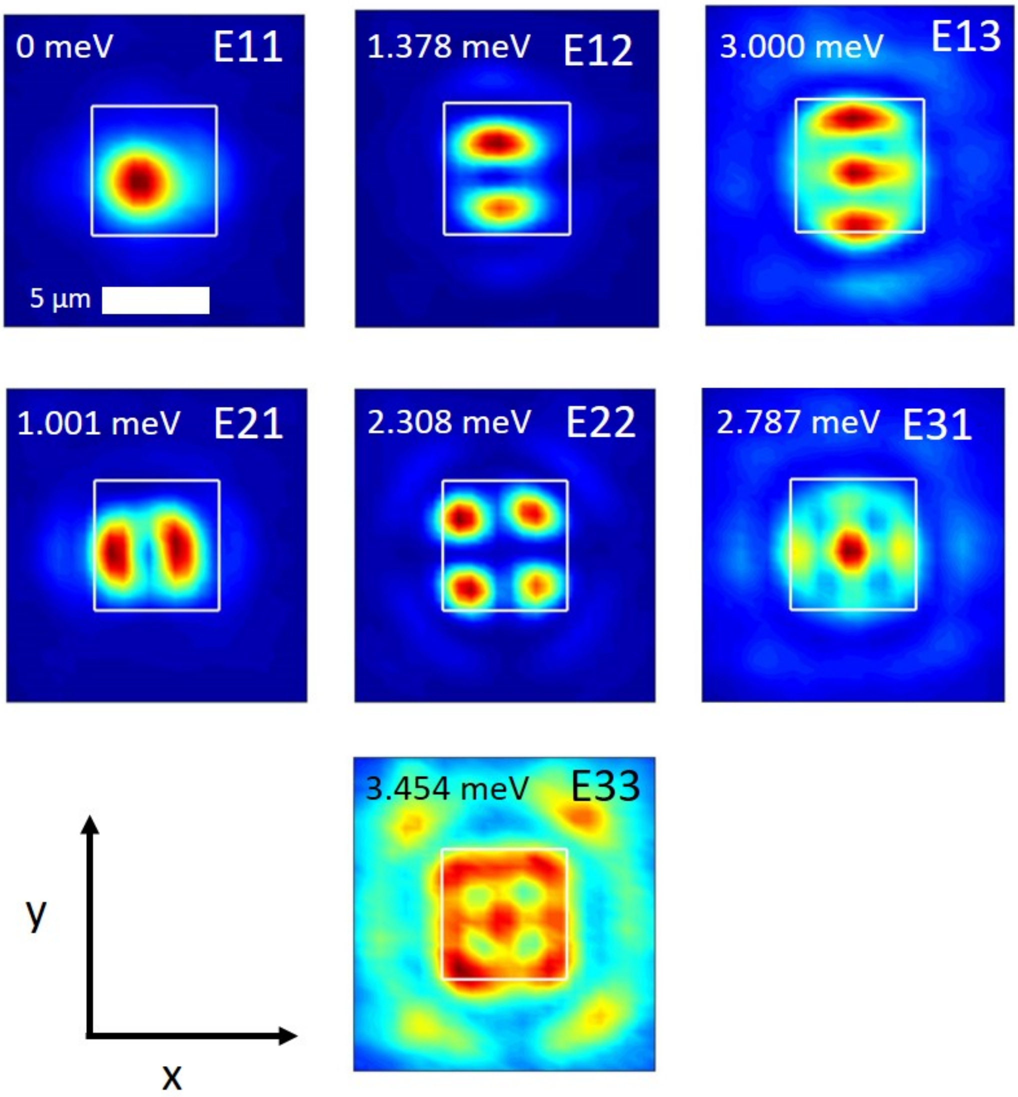

Figure 3.4: Spatial profile of the modes of a 5μm micropillar, resolved in horizontal polarisation. They correspond to Hermite-Gauss modes (HG$_{nm}$). Energy of E_{nm}-E'_{11}, E'_{11}=1446.6 meV; E_{11}=0 meV E_{21}=1.001 meV, E_{12}=1.378 meV, E_{22}=2.308 meV, E_{31} = 2.787 meV, E_{13}=3.000 meV, E_{33}=3.454 meV.

the laser path. When incorporating the second laser in a pump-probe scheme, the second laser will have a Gaussian spatial profile that matches the E_{11} mode, with both beam waists of $3\mu m$.

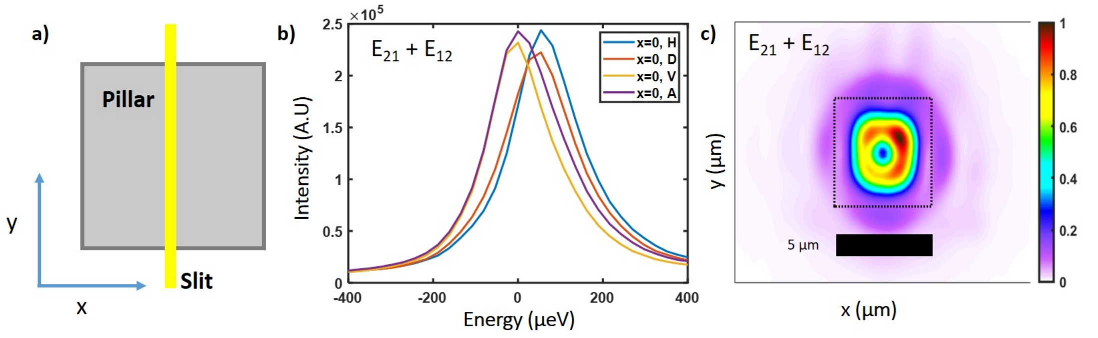

Figure 3.5: Resolving the linear polarisation splitting for the $\mathbf{E_{12}/E_{21}}$. a) Schematic for the slit position on the pillar when doing tomographic scans. The slit is at position x=0. b) The polarisation splitting for the E_{12} mode, measured at slit position x=0. Polarisation basis $|H\rangle$, $|V\rangle$, $|A\rangle$ and $|D\rangle$. A maximum splitting of 62 μeV and linewidth 190 μeV. c) PL map for E_{21} and E_{12} summed over the polarisation basis.

3.4 Nonlinear pumping of micropillar

In this section, three different experiments are presented, in each the E_{12} *pump* mode is excited. The first and second subsections will use a single pulsed laser incident on the E_{12} mode. The laser is blue detuned 100 μeV from the E_{12} pump state, the input power steadily increasing. The output from the E_{12} mode increases rapidly when the E_{12} mode shifts into resonance with the laser energy.

The E_{11} and E_{13} counts are integrated on the CCD region, observing some scattering into the E_{11} *signal* and E_{13} idler mode. However, no quadratic dependence was observed in this process.

Finally, the pump-probe configuration is used to enhance the scattering into the E_{11} and E_{13} state. The E_{11} signal state is excited with a pulsed laser with orthogonal polarisation to the pump. The E_{13} CCD counts are integrated, and an above quadratic dependence was observed for integrated intensity.

3.4.1 Renormalization

A well-known result of the polariton system is the renormalization of the polariton dispersion under strong excitation. The spectrum of the device is shown by non-resonant excitation in figure 3.7a. The light emitted from the cavity is imaged using the near-field techniques discussed in the methods section. The pulse length of the laser is 200ps and horizontally polarised, see figure 3.6. This laser is blue detuned 100μeV from the E_{12} mode, highlighted by the white dashed line in the PL emission. The incident power is increased from 2-58μW (average power), with the integrated counts of the E_{12} region plotted against power in part b of the figure.

The integrated CCD counts gradually increase until close to 40μW, where the counts double over a very small energy range. This sharp increase is the E_{12}

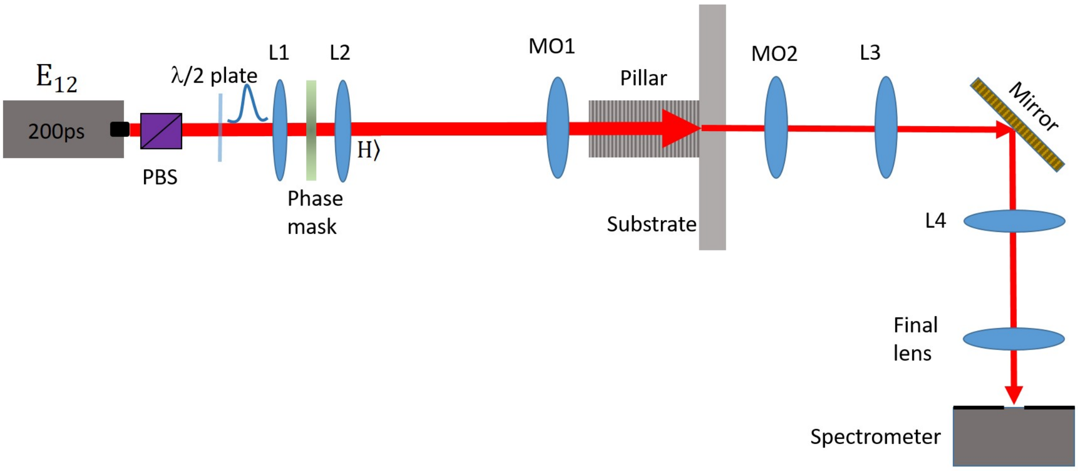

Figure 3.6: Experiment pump excitation scheme. A pulsed laser 200ps, polarisation beam-splitter PBS, a half-wave plate $\lambda/2$ plate, plano-convex lenses Ln where n=1,..,4, microscope objective MOn where n=1, 2.

mode moving into resonance with the laser energy. The mechanism behind this process is the repulsive interaction experienced between polaritons as they begin to fill the E_{12} state. As the polariton number in the E_{12} mode increases, so does the energy of the mode. With each positive energy increase bringing the mode closer to the laser energy, the laser begins to efficiently excite the E_{12} mode, which produces the jump in intensity in figure 3.7b.

3.4.2 Parametric scattering attempt

Parametric scattering is a requirement blockade proposal, In the polariton field, the effect has been observed in both planar [118] and lower-dimensional structures [109]. In our square micropillar devices, the phase-matching conditions are met by the in-plane momentum of the modes selected. We choose square devices to allow for better coupling into the E_{12} state, which has a different mode profile compare to the circular pillar. Energy conservation is the other ingredient for parametric scattering, with a device chosen to match this. Figure 3.8 shows how parametric scattering in our system is possible. The spatial and electric field profiles are in red and blue colours. The red and blue colours highlight that the

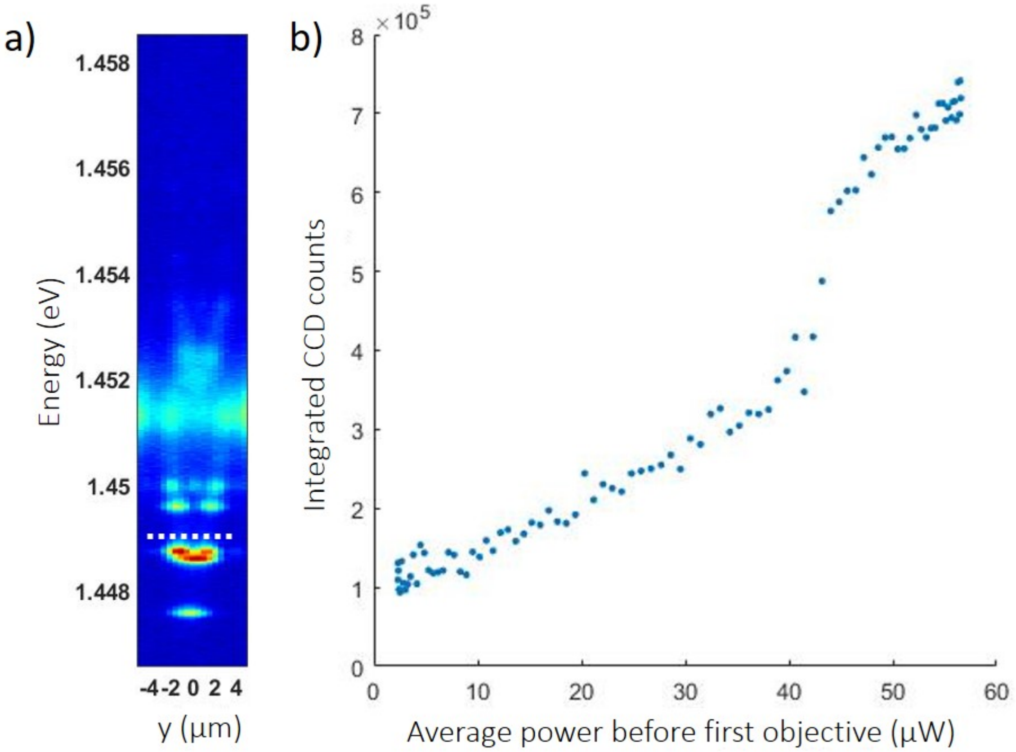

Figure 3.7: Blueshift of E_{12} into resonance with laser 100μeV above the mode for a 5μm square pillar. a) Photoluminescence showing modes and white dashed line indicating laser position. b) CCD photon counts as a function of input power before the first objective, showing a sharp increase in counts as mode blueshifts into resonance with the laser.

degenerate lobes have different phases. Next, the intensity profile is to the right, seen during near-field PL measurements, with respective modes labelled. On the far right are the momentum values for selected modes. For two particles occupying the E_{12} mode, the signal and idler modes that satisfy the phase-matching condition are the E_{11} and E_{13} modes.

To test whether we can get parametric scattering in our system, we select a device where the modes have near-equal separation. The mode separations: $E_{12} - E_{11} = 1.179$meV, $E_{13} - E_{12} = 1.201$meV giving an overall difference of $21\mu eV$. When taking into account the three mode linewidths, the 21μeV peak to peak difference is not an issue with energy conservation, especially when compared to other work [109]. We excite the E_{12} mode resonantly with a 200ps pulsed laser with horizontal polarisation. The E_{12} mode has $|X|^2 \approx 0.22$, with the laser power increased from 10-70nW, equivalent to ∼12-87 polaritons peak. Placing a linear polariser cross-polarized with this laser (vertical polarisation) in the collection path before the spectrometer entrance. Imaging the modes on the CCD, with the regions of interest being the E_{11} and E_{13} intensities.

A signature of parametric scattering is a quadratic dependence of emission counts vs input power, an x^2 relationship with the pump. To test this, we integrate the photon counts detected on the E_{11} and E_{13} regions and plot vs input power, figure 3.9a, c. To find the exponent that describes the growth of intensity vs input power, we fit the function, $y = ax^n$. Where y is the integrated counts in E_{11} or E_{13} mode, a is the intercept, x is the input power, and n is the exponent that will determine the efficiency of the scattering process. The logarithmic plot $\log(y) = log(a) + n\log(x)$, the straight-line fit will extract n, as shown in figure 3.9b and d.

The relationship is sub-linear, 0.6 and 0.3 for the E_{11} and E_{13} mode respectively, not the desired n =2 value. Other micropillar devices were investigated, but in none was parametric scattering achieved for E_{12} excitation only.

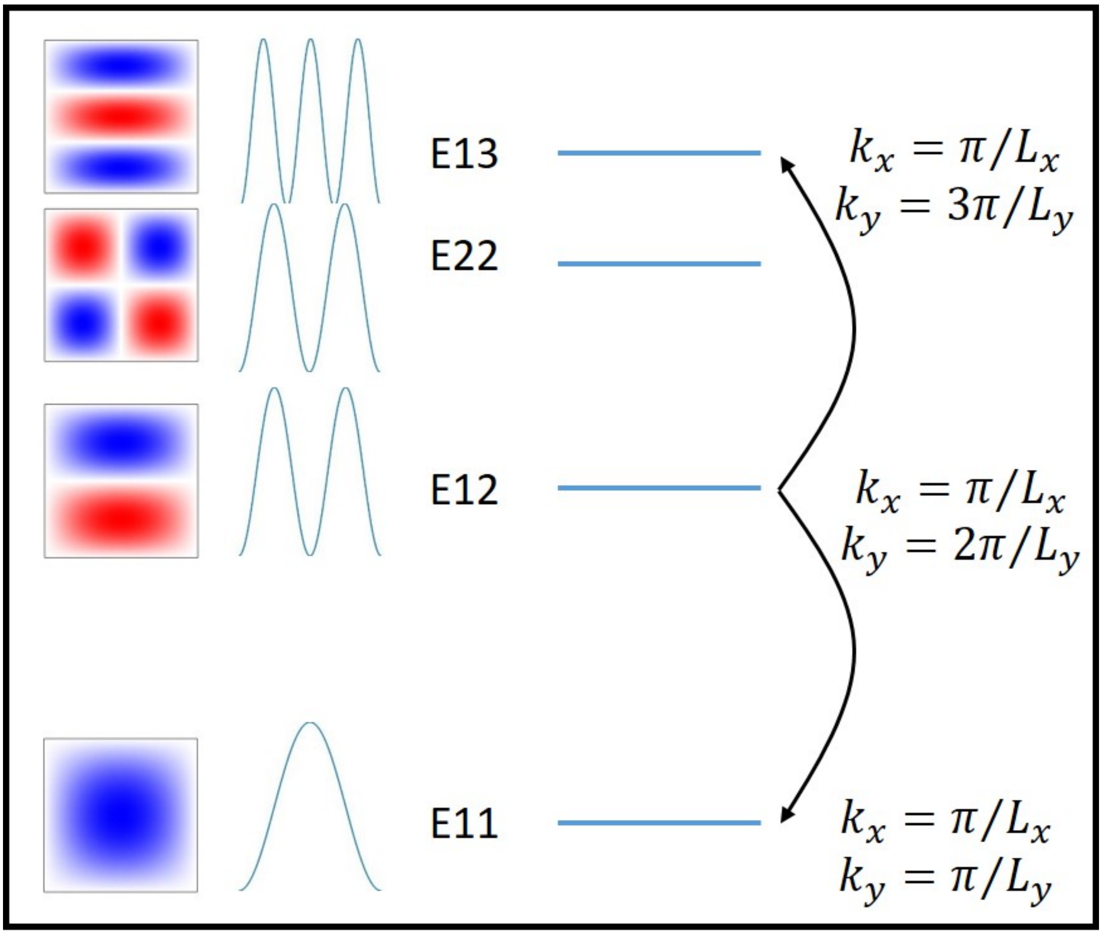

Figure 3.8: Parametric scattering in the micropillar device. From left to right: the spatial profile for modes of interest with the red/blue colours representing regions where modes have opposite phases, an intensity profile for the modes when summed along the x-axis, the respective modes labelled with momentum for the square micropillar modes. Where k is the momentum and L is the length of the square sidewall, in our device, $L_x = L_y = 5\mu m$.

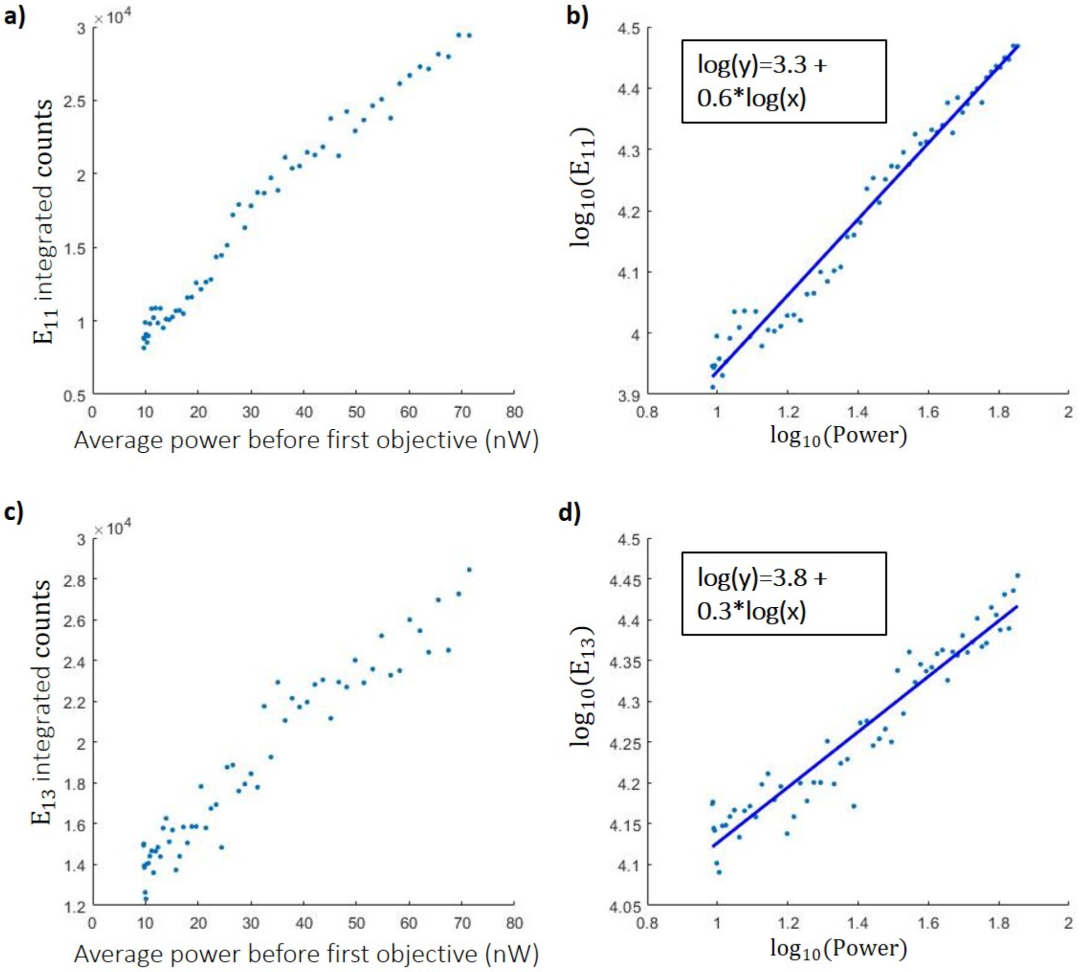

Figure 3.9: Integrated E_{13} and E_{11} mode counts for pump only excitation experiment. a) The raw CCD integrated counts for the E_{11} region b) Using figure (a) log(power) vs log(counts) to extract the power law of 0.6 . c) The raw CCD integrated counts for the E_{13} region. d) Using figure (c) data, log(power) vs log(counts) to extract the power law of 0.3.

3.4.3 Pump-probe excitation

Using a single pulsed laser incident on the E_{12} mode did not show any quadratic behaviour in the E_{11} or E_{13} mode, other scattering mechanisms are hindering the parametric process for E_{12} polaritons. Polariton-polariton scattering can be stimulated by seeding a polariton population in the final state [110], see figure. The E_{11} mode is excited in transmission geometry with a vertically polarized pulsed laser. The E_{11} is excited with a fixed average power of 20-40μW, corresponding to a peak E_{11} polariton population of ~23000 and ~45000. The E_{12} mode is excited with a horizontally polarized pulsed laser, shown in figure 3.10. The average incident power is gradually increased from 1.5-5μW, corresponding to a peak polariton number of ~1900-6300 E_{12}.

The modes emission is collected using near-field imaging. A vertical linear polariser is placed in collection, suppressing the laser scatter contribution from the E_{12} mode onto the E_{13} mode region. Figure 3.11 shows the result of the E_{11} and E_{12} excitation.

The E_{13} emission region is isolated from the rest of the luminescence and laser scatter. The region of interest is then integrated to give a measure of the number of photons in the E_{13} region. The input power before the first objective is the average power of the laser resonant with the E_{12} mode only. The laser resonant with the E_{11} mode is on continually. In sub-figures a-b, 20μW average power is used, while c-d 40μW is used.

It is clear that the E_{13} mode increases beyond a quadratic dependence in both cases. The relationship between the E_{13} mode and the input power is extracted by fitting the data logarithmically. The growth for the E_{13} for 20μW shows an $x^{2.6}$, while for 40μW shows $x^{3.6}$ for the majority of the data. Note that in c-d, the data is truncated and fitted separately, as the rate of increase in counts changes

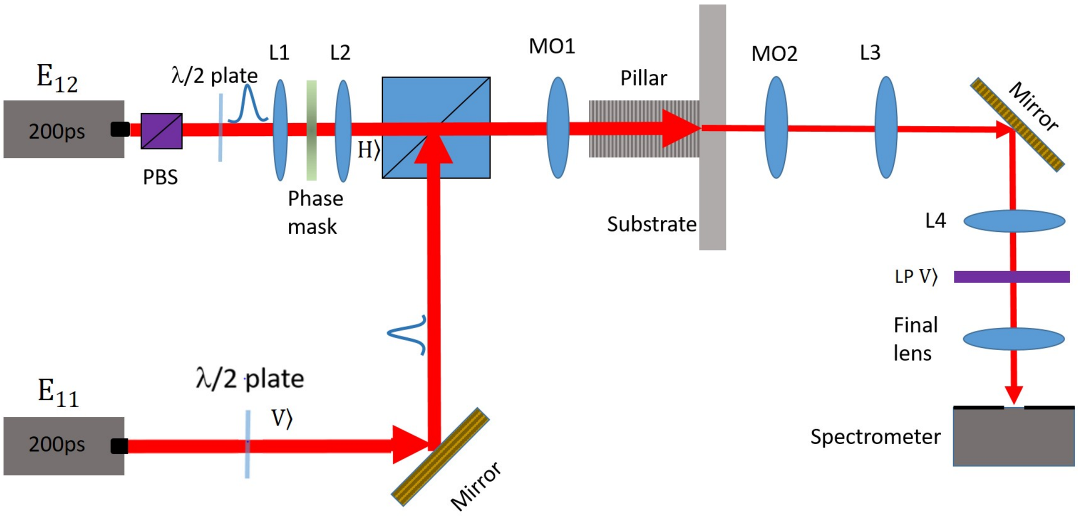

Figure 3.10: Experiment pump-probe excitation scheme for stimulated scattering. Two pulsed lasers set to 200ps, polarisation beam splitter PBS, a half-wave plate $\lambda/2$ plate, plano-convex lenses Ln where n=1,..,4, microscope objective MOn where n=1, 2, a vertical linear polariser LP $|V\rangle$.

significantly.

Figure 3.11 clearly demonstrates that the scattering to the E_{13} mode, can be greatly enhanced by using a large E_{11} seeding population. However, what other behaviour could we expect to be seen from the E_{13} mode if stimulated scattering is occurring?

Figure 3.12 shows a clear change in emission from the E_{13} mode, looking at sub-figures a-b, shows the near-field photoluminescence under single and two laser excitation, with the E_{13} visible inside the square white box. Visually it is clear that the linewidth of the mode has narrowed. By measuring the linewidth of the region over the power range mentioned previously, part c, the narrowing becomes even more clear. The linewidth increases from 230μeV to 280μeV before rapidly decreasing over a small power range to 45μeV. Part d plots the fitted peak position of the E_{13} mode, at 2.3μW input power the peak energy blueshifts and then saturates at approximately 100μeV above the initial E_{13} peak energy.

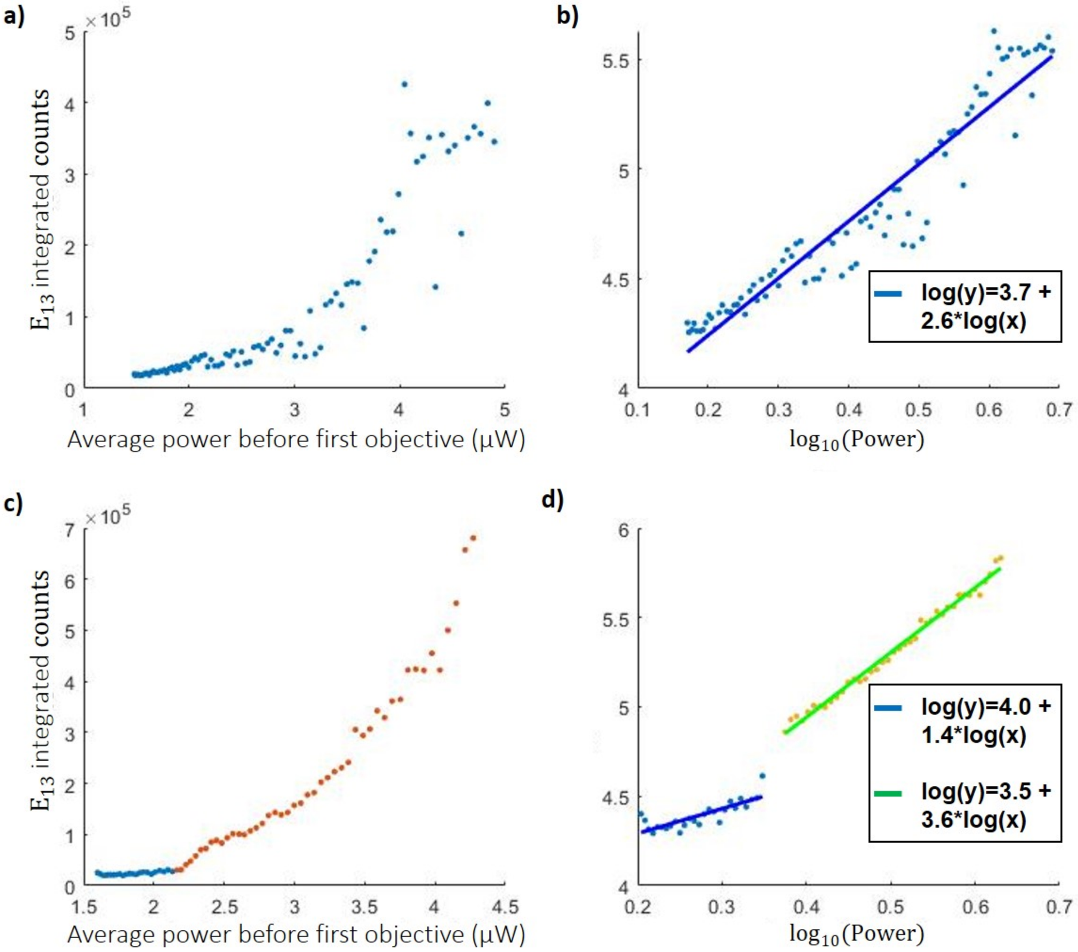

Figure 3.11: Integrated $\mathbf{E_{13}}$ mode counts for pump-probe experiment. The pump laser is gradually increased, while the E_{11} state is excited with a-b) 20μW and c-d) 40μW. a) The raw CCD integrated counts for the E_{13} region, for a probe power of 20μW, b) Using figure (a) data, log(power) vs log(counts) to extract the power law of 2.6, a) The raw CCD integrated counts for the E_{13} region, for a probe power of 40μW, d) Using figure (c) data, log(power) vs log(counts) to extract the power law of $x^{1.4}$ and $x^{3.6}$.

Another result observed but not included was the strong dependence on the E_{12} excitation energy. After polaritons condense into the E_{13} state, the laser incident on the E_{12} mode was red and blue detuned from resonance. The energy of the E_{13} mode moves to a higher (lower) energy when the pump laser is blue (red) detuned from the E_{12} mode. The E_{13} state, therefore, has a strong energy dependence on

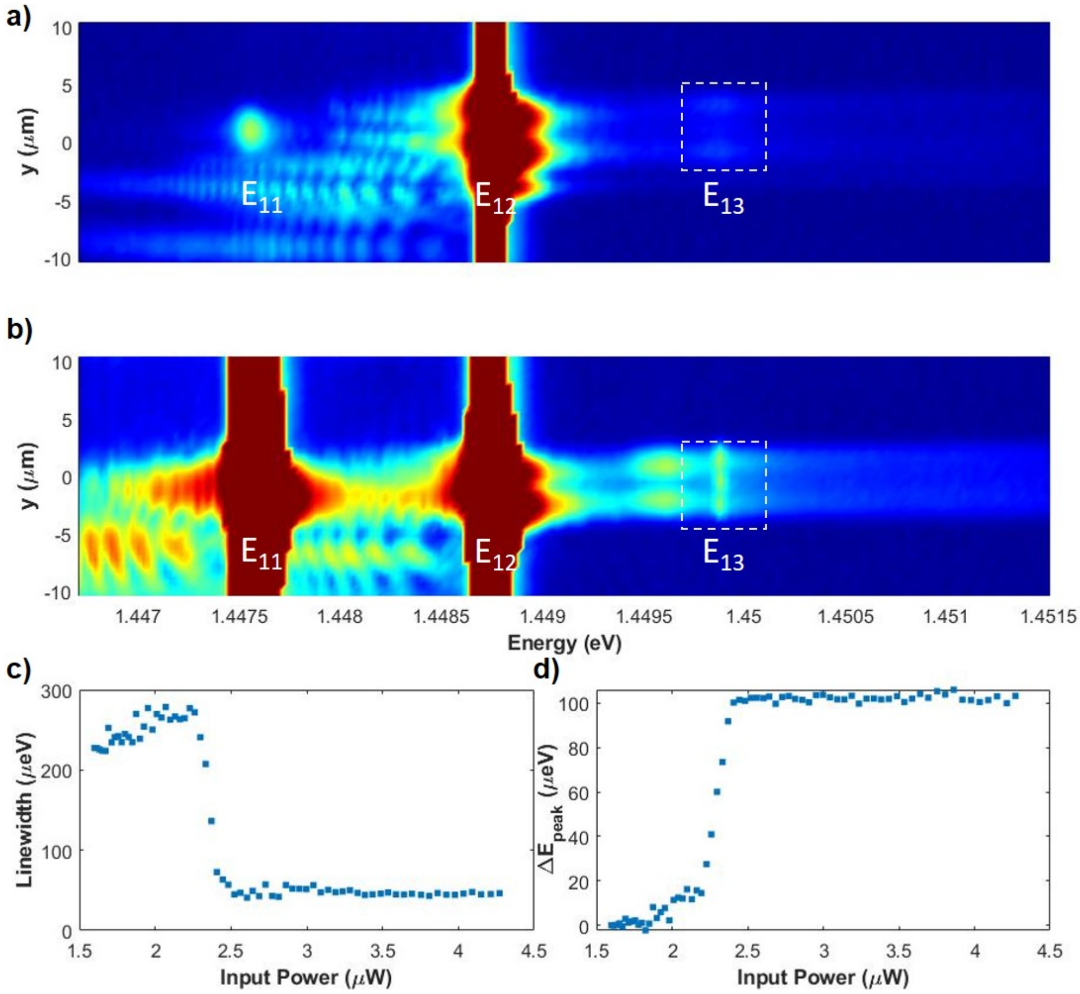

Figure 3.12: The transition from weak scattering into the E_{13} state to enhanced stimulated scattering in the E_{13} state. a) Single laser excitation of the E_{12} mode, the E_{11} and E_{13} mode are populated. Note that the E_{13} mode is highlighted with a white box. b) Two laser excitation of the E_{11} and E_{12} state, the E_{13} mode is clearly visible with a narrow linewidth compared to (a). The E_{13} mode is highlighted in a square box. c) The fitted (Lorentzian) linewidth of the E_{13} vs input power d) The fitted (Lorentzian) peak energy vs input power, $\Delta E_{peak} = E_{peak} - 1.4499$ eV.

the pump laser.

Producing parametric scattering at low polariton numbers was not achieved in any device. The powers used to observe stimulated scattering are several orders of magnitude higher in the E_{12} state compared to the single polariton level, even with a large E_{11} population. A solution to this could be to excite the E_{11} mode with even higher polariton numbers, however, exciting the E_{11} mode with such high power results in a population of E_{12} polaritons. Therefore the strength of the E_{11} excitation is limited when attempting the parametric blockade. The micropillar displayed in the parametric and stimulated scattering subsections had an appropriate mode energy separation; $E_{12} - E_{11} = 1.179$meV, $E_{13} - E_{12} = 1.201$meV and giving an overall difference of $21\mu eV$. This ∼1meV energy separation posed a challenge concerning laser scatter into the nearest neighbour state. In the following section, the E_{11} mode is populated with the maximum power such that no emission is detected from the E_{12} mode, which was 400 polaritons peak. The E_{12} mode is then injected with a peak power equating to N_{pol} =1, approximately 40pW average output in transmission.

3.5 Photon statistics of light emitted by polariton micropillar

The interactions between light and matter can strongly modify the statistical properties of photons [119]. The metric that allows experimentalists to claim to have super-Possionian (bunched), Possionian or sub-Possionian (anti-bunched) photon statistics is given by the second-order coherence function $g^{(2)}(\tau)$.

The device that is used to show stimulated scattering into the E_{13} mode will be seeded with an E_{11} population of 400 polaritons. At the same time, the E_{12} mode is excited with a peak population of 1 polariton, as shown in figure 3.13. The emission from the E_{12} mode is filtered through a spectrometer and put into a Hanbury-Brown and Twiss (HBT) interferometer detection scheme. Where the coincident photons arriving on two avalanche photodiodes (APDs) construct the $g^2(\tau)$ function of the E_{12} emission. No anti- or bunched-photon statistics for the E_{12} emission is observed, with the value for $g^2(0) = 1$ value consistently observed.

3.5.1 Second-order coherence polariton statistics

The emission from the microcavity is measured using an HBT interferometer setup. The E_{12} mode emission is transmitted through the side exit slit of the spectrometer, and signal strength is maximised on both APDs. See figure 3.13. Joint photon coincidences are registered according to the first and second photon detection times. The expression for the number of coincidences $G^{(2)}$ is given by:

$$G^{(2)}(\tau) = \langle n_1(t) n_2(t+\tau) \rangle, \tag{3.1}$$

where n_1 and n_2 are the number of photons registered on detectors one and two at time interval t and $t+\tau$. The E_{12} is coherently excited with a pulsed laser with a repetition rate of 80 MHz. Photon coincidences appear 12.5ns apart. Figure 3.14a shows the raw photon coincidence sorted by the arrival time. The number

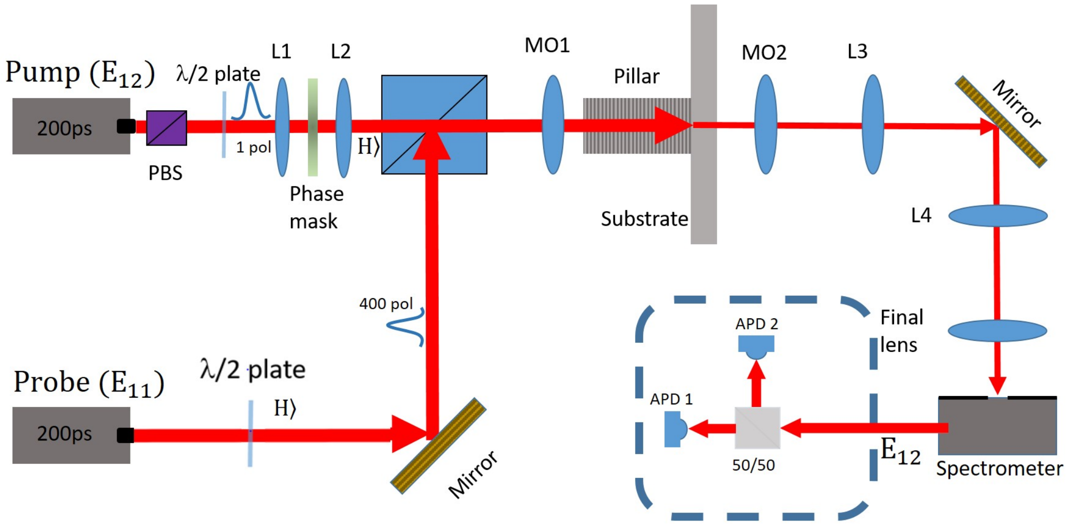

Figure 3.13: Experiment pump-probe excitation scheme with Hanbury-Brown and Twiss interferometer. Two pulsed lasers set to 200ps, polarisation beam splitter PBS, a half-wave plate $\lambda/2$ plate, plano-convex lenses Ln where n=1,..,4, microscope objective MOn where n=1,2, vertical linear polariser LP $|V\rangle$, a 50/50 beam-splitter and two avalanche photodiodes ABDn n=1, 2.

of coincidences $G^{(2)}(j)$ between photons in pulses separated by a time jT, where j is an integer. By integrating over a range of τ the pulse area $G^{(2)}(\tau + jT)$ is found [31, 40, 120]. The life-time of the polariton system are much faster than the time delay between successive peaks, therefore, there are no correlations between successive pulses. The formula for calculating the normalised $g^{(2)}(j)$ is given by:

$$g^{(2)}(j) = \frac{\int_{-\Delta t}^{+\Delta t} \langle n_1(t) n_2(t+\tau+jT)\rangle d\tau}{\frac{1}{N-1}\Sigma_{i\neq 0} \int_{-\Delta t}^{\Delta t} \langle n_1(t) n_2(t+\tau+jT)\rangle d\tau} \tag{3.2}$$

where $N = 7$ is the number of pulses recorded.

The strongest signal to noise ratio (SNR) is selected when choosing the integration window for each pulse. The SNR is calculated following the supplementary information of Munoz et al.[40]. Finding a baseline number of counts for the $\tau = 0$ pulse, S_D, then calculating the optimal signal window width w. The

SNR(w) function is:

$$SNR(w) = \frac{\sum_{j=-w}^{j=+w} S_j}{\sqrt{\sum_{j=-w}^{j=+w} S_j + (2w+1)S_D}}. \tag{3.3}$$

The errors are calculated by finding the peak number of photons in a given pulse window and calculating the Poisson error. The average of the uncorrelated peaks is found, except $j \neq 0$, with error propagated and added in quadrature to the value for $g^{(2)}(0)$.

The laser is transmitted through the GaAs substrate, with the resulting raw and $g^{(2)}(\tau)$ shown in figure 3.14, where $g^{(2)}(0) = 1$, which is expected for a coherent light source.

3.5.2 Pump-probe photon statistics

The excitation scheme takes the same form as the stimulated scattering section, a pulsed laser is matched to the E_{12} mode using a phase mask and tuned into resonance. A second pulsed laser probe is locked to the repetition rate of the other laser and excites the E_{11} mode. Both lasers are horizontally polarised and were transmitted through the GaAs substrate, with pulses checked to see their overlap in arrival time. The light is then transferred through the spectrometer and into the HBT setup, where the peaks were visibly overlapped. An optical delay stage was introduced into the path of the probe laser to ensure the pulses arrive at the same time. The probe laser is tuned into resonance with the E_{11} mode, with a peak power equivalent to 400 polaritons.

The pump laser is tuned with respect to the E_{12} mode using three detunings; +80μeV, 0μeV and -34μeV. The peak power of the pump laser is equivalent to 1 polariton. Figure 3.15 shows this dependence, the value of $g^2(0)$ does not change significantly and remains ≈ 1.

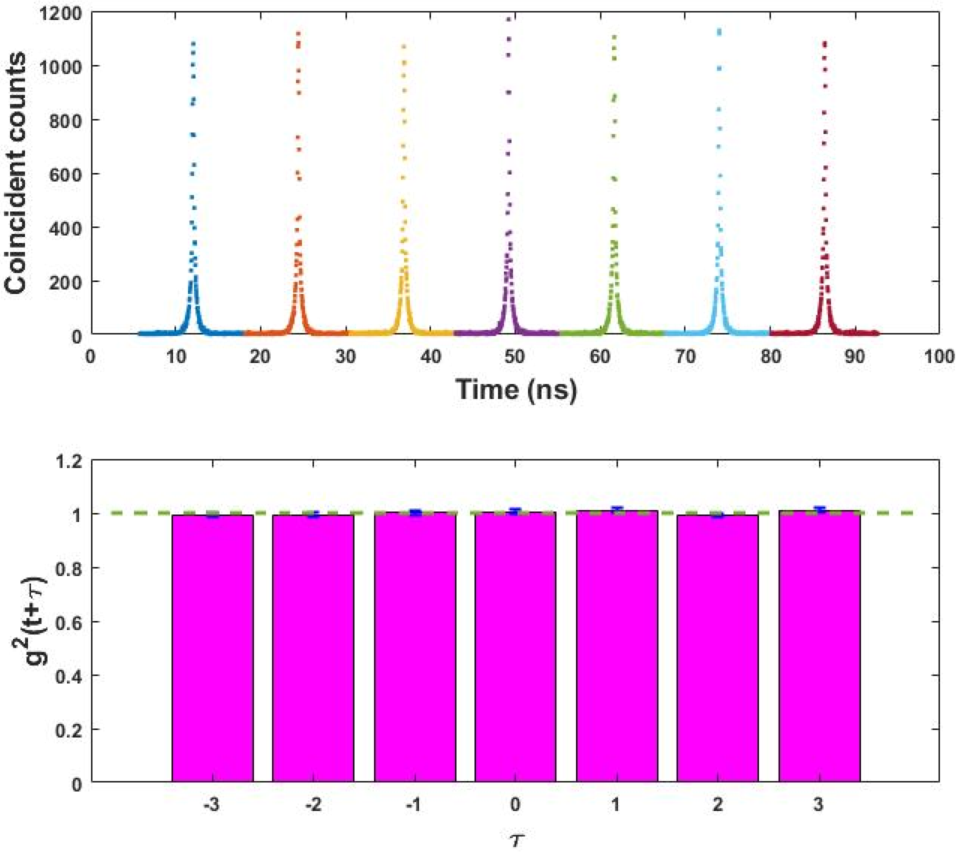

Figure 3.14: Example of the $g^{(2)}$ value obtained when transmitting a pulsed laser through a GaAs substrate. a) Raw coincident count data, b) Normalised coincident count data.

Along with pump-probe excitation, a pump laser only excitation was tried to the E_{12} mode. The only difference is no E_{11} polariton population. There was no deviation from $g^2(0) = 1$. The E_{11} polariton population was chosen based on the background contribution to both the PL spectra and the amount of suppression obtainable by narrowing the spectrometer exit slits. On the APDs, no background is seen in the E_{12} mode emission when the probe laser is used.

In addition to the measurements presented, an E_{11} population of 1 polariton was tried, where again $g^2(0) = 1$. These measurements were done on the same

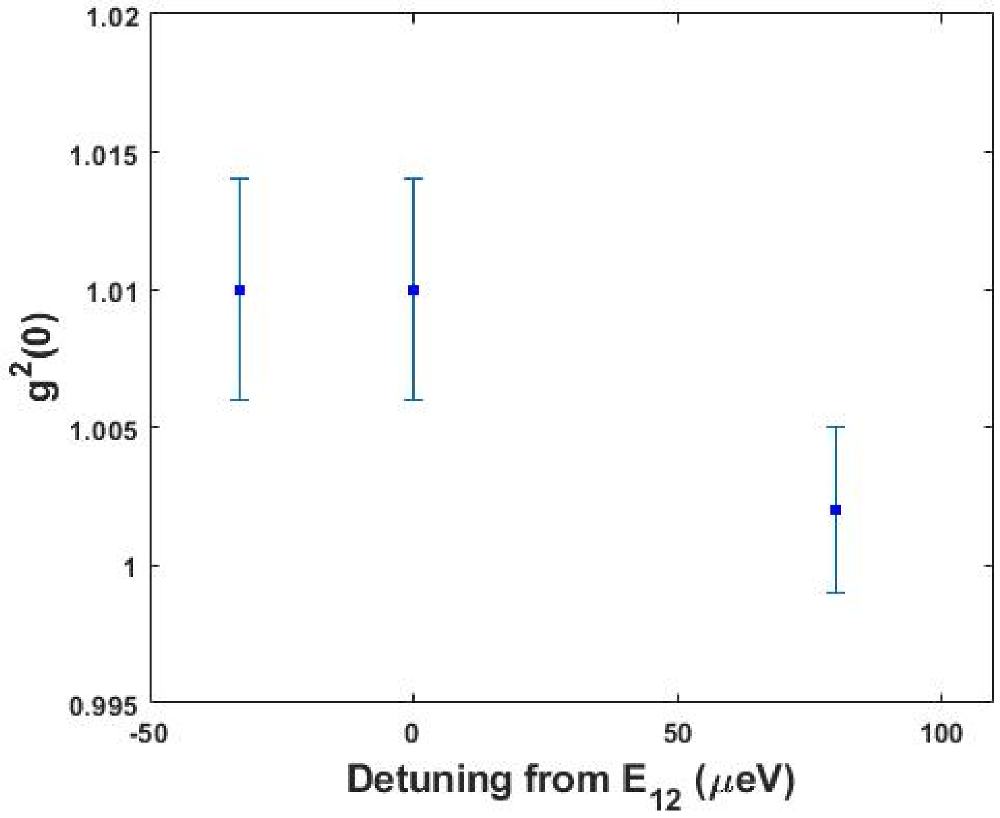

Figure 3.15: Second-order correlation as a function of detuning. The E_{12} mode 1 polariton peak (40pW average power transmitted) $|H\rangle$, with E_{11} excitation of 400 polaritons peak (17.7nW average power transmitted) $|V\rangle$. Both lasers have a pulse length of 200ps.

device used for the parametric and stimulated scattering study.

Moving to a larger energy spacing between micropillar modes would allow for a larger amount of power used in the E_{11} excitation. An equal energy spacing was not obtainable for beyond pillars with mode separation of ~1meV. As the energy spacings increase, the energy conservation to observe parametric scatting in the device becomes an issue. One way to overcome this mode separation issue for larger spacings is to change the temperature of the sample. As the temperature increases, all of the polariton modes redshift [109], as shown in figure 3.16. Bajoni et al. used this variable to reach better spectral equidistance and observe parametric scattering. The modes with a higher excitonic (closer to exciton) fraction will have a larger redshift than modes that are more photonic (further from exciton). Temperature control was attempted, but there were difficulties maintaining a chosen temperature.

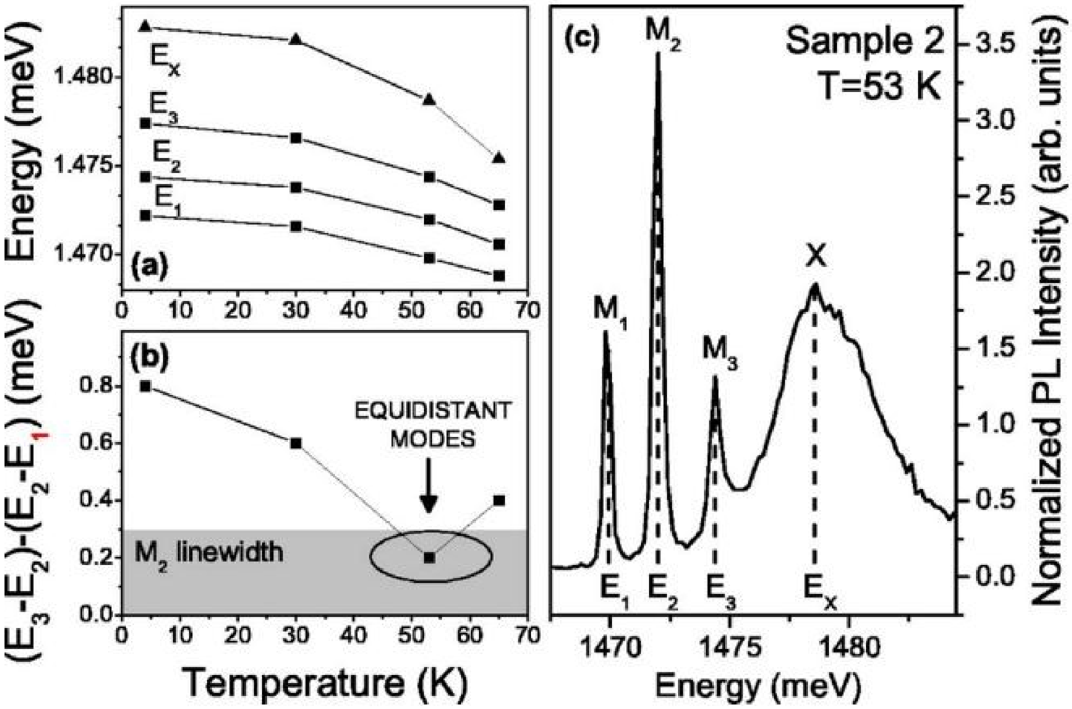

Figure 3.16: The modes of a circular micropillar device as a function of temperature. a) The mode and exciton energies as a function of temperature. b) The energy difference between the three modes of interest, including the middle mode linewidth. c) The mode spectra at the best temperature, T=53K. Taken from ref. [109].

3.6 Discussion

In this chapter, the energy profiles of micropillar devices were investigated. The size dependence diameter on mode spacings was analysed, and tomographic scans showed the spatial and energy profile of the modes. The E_{12} mode (pump) was excited strongly to explore nonlinear effects, demonstrating a blueshift in the polariton spectrum. The best device was selected for parametric scattering; the criteria were based on energy spacing and momentum conservation. Exciting the E_{12} mode only, emission in the E_{11} and E_{13} modes were clearly seen. The efficiency of the polariton parametric scattering depends on the cavity quality factor and the number of quantum wells. There is only one quantum well in the sample, which is likely why it was not observed.

The linewidth of E_{12} found through non-resonant PL is approximately $190\mu eV$. In chapter 4, an E_{12} mode linewidth is calculated by transmitting the laser across a range of frequencies. A linewidth of $87\mu eV$ was found for different devices with comparable characteristics. The quality of the micropillar device is approximately 18000, found by dividing the mode energy by the linewidth, and is better than those discussed in [109].

The emission from the E_{11} and E_{13} was approximately the same for single laser E_{12} excitation. In planar parametric scattering experiments, the signal is stronger than the idler intensity. This equal intensity was seen for parametric scattering in micropillars [109] and could allow for quantum correlation by quantum noise measurements [121]. Polariton micropillar devices that efficiently pair scatter could be a source for correlated photon pairs in quantum cryptography protocols [122]. With the modes of the micropillar device providing the required phase matching, without relying on birefringence to provide this in bulk nonlinear crystals [123].

Introducing strong excitation in the E_{11} mode (signal) was shown to enhance the scattering process greatly. Results showed a strong increase in the E_{13} mode (idler) population, along with evidence of stimulated scattering where the mode linewidth narrowed significantly. If the E_{11} excitation is removed, the E_{13} population growth remains sub-linear with increasing E_{12} excitation power (over the same range of power).

The powers used in E_{11} and E_{12} excitation are significant to observe stimulated scattering into the E_{13} mode, which posed issues for the intended parametric blockade attempt. Strong E_{11} pumping produced emission in the E_{12} state, and required strong E_{12} excitation to observe stimulated scattering into the E_{13} state. Again, this power is several orders of magnitude higher than injecting a single polariton. The parametric blockade attempt in the previous section served as a starting point for how the experiment can be carried out if the prerequisites for the blockade are met.

Chapter 4

Few-photon all-optical phase rotation in a quantum-well micropillar cavity

4.1 Motivation

Photons are an excellent tool for performing quantum information processing[124], due to weak interactions with their environment, long coherence times are achievable, which are necessary when quantum applications increase complexity. Two well known $\chi^{(3)}$ non-linear optical processes are *self-* and *cross- phase modulation* (SPM, XPM). Both of these processes have been studied extensively in optical fibres [125, 126]. In self-phase modulation, a frequency of light passing through a medium will change the refractive index experienced by itself. When a second frequency is present, the phase for both frequencies of light will change, this is cross-phase modulation.

Using two optical beams to observe changes in the level of single photons is a necessary stepping stone toward all-optical quantum information processing. This approach underpins many proposed applications in quantum optics[127] and information processing[128]. An obvious problem here is the weakness of the photon-photon interaction, making it hard to see changes at the single-photon level. Therefore, photons must be made to interact stronger with each other.

Approaches such as; electromagnetic induced transparency (EIT) and slow light [129], Rydberg blockades[130] and single atom strongly coupled to a micro-resonator cavity [131]. These approaches can produce very strong interactions, with this platform still debated due to *phase noise* not allowing for high fidelity operations to be performed [132, 133].

Intermediate or weak strength nonlinearity approaches have been put forward for two modes interacting in a nonlinear medium, allowing for the implementation of a near-deterministic controlled-phase gate [134, 135]. The process involves imparting a phase shift by a few photons or single-photon onto a coherent light source, resulting in small phase shifts. The ability to impart a phase shift of this kind was demonstrated by A.Feizpour et al. [136] using laser-cooled ^{85}Rb atoms in an EIT configuration, reporting a phase shift of 18 μrad per photon. The table below shows the current leading phase shift values reported from different approaches involving XPM:

System	**ϕ per particle (mrad)**
Rydberg atoms in EIT [129]	500
Single Cs atom [137]	280
Strongly coupled quantum dot [131]	220
Rb vapour in hollow core fibre [138]	0.3
Metastable Xe [139]	0.0003
Photonic crystal fibre [140]	0.0001

Table 4.1: Phase shift values in platforms reported in literature.

The table contains different approaches ranging from experimentally challenging preparation of EIT with significant phase shifts to forward and backwards running photons in an optical fibre Sagnat interferometer. In the latter, a small phase is imprinted per photon. In the case of quantum dots (QDs), strong interaction and phase shifts are reported. Although the size of the phase shifts is attractive using QDs, there are scalability challenges such as deterministic growth and frequency tuning for their implementation in optical circuits.

Polariton micropillars can offer a compromise to the approaches listed, providing intermediate phase shifts while circumventing scalability challenges. As the methods section describes, a microcavity can be etched into various shapes and sized pillars. This parameter allows freedom to choose the energy spacing and the polariton confinement potential, as discussed in chapter 3. The Polaritons' excitonic interactions are at least 1000 times larger than in the weak coupling or bulk semiconductor devices [141]. As discussed in the introduction, polariton micropillars are used in many research areas. Nevertheless, the resonant transmission through two polariton modes and the phase shift's size attributed to XPM have not been quantified.

This chapter presents the experimental demonstration of a 3mrad per polariton phase rotation. Resonant transmission through two polariton modes in a square micropillar results in phase shift imparted on one by the other. A collection of different platforms that mediate photon-photon interaction to produce phase shifts are shown in figure 4.1. The device details used for this experiment will be discussed next.

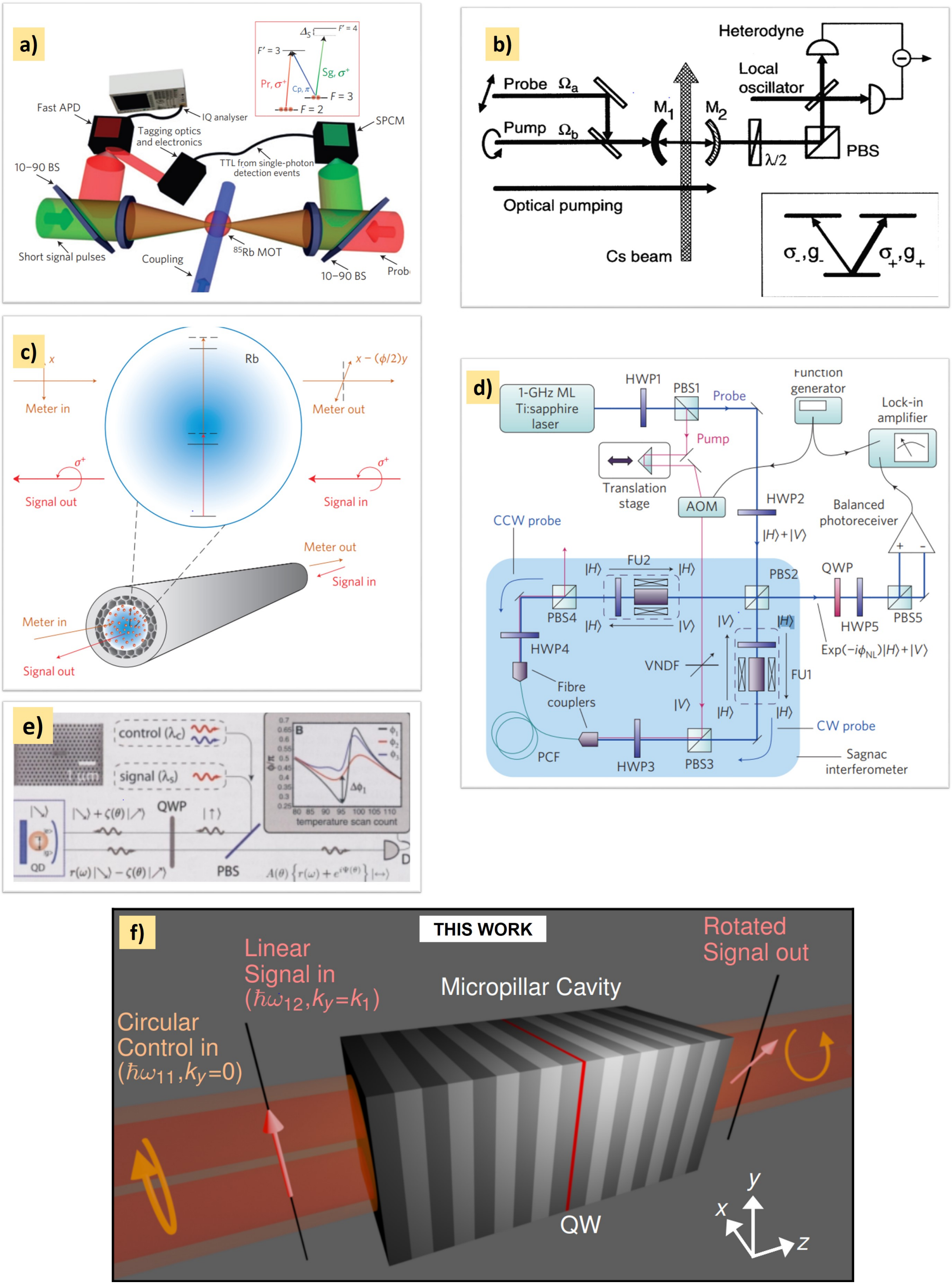

Figure 4.1: Collection of Kerr-effect phase shift platforms. a) ^{85}Rb cloud in EIT, taken from ref. [136]. b) Cs atom coupled to resonator, taken from ref. [137]. c) RB vapour confined to hollow-core photonic bandgap fibre, taken from ref. [138]. d) Optical fibre Sagnac interferometer, taken from ref. [140]. e) QD coupled to a phononic crystal, taken from ref. [131]. f) Polariton micropillar, taken from ref. [2].

4.2 Square Micropillar Devices

The micropillar energy structure for the two pillars used in this experiment is shown in figures 4.2 and 4.3, revealed through non-resonant excitation and near-field imaging PL. The pillars used are labelled A and B, with the significant difference between the two being the excitonic and photonic fraction of the polariton modes. The mode separations are also different.

The mode linewidths can either be extracted from non-resonant PL or, more accurately, by resonant transmission in small wavelength steps through the mode of interest. This characterisation is shown for pillar B E_{12} mode in figure 4.4. Measurements of this kind establish the mode energy and linewidth for theoretical estimations of the phase shift value. The E_{11} linewidth for pillar A (B) was measured to be $90\mu eV$ $(83\mu eV)$, E_{12} in pillar B was found to be $87\mu eV$. The E_{12} linewidth was not measured in pillar A, but it is safe to assume a similar value to pillar B. The measured linewidths are larger than the planar cavity linewidths predicted by the transfer matrix method (20-30 µeV), which is most likely due to absorptive losses associated with elevated sample temperature.

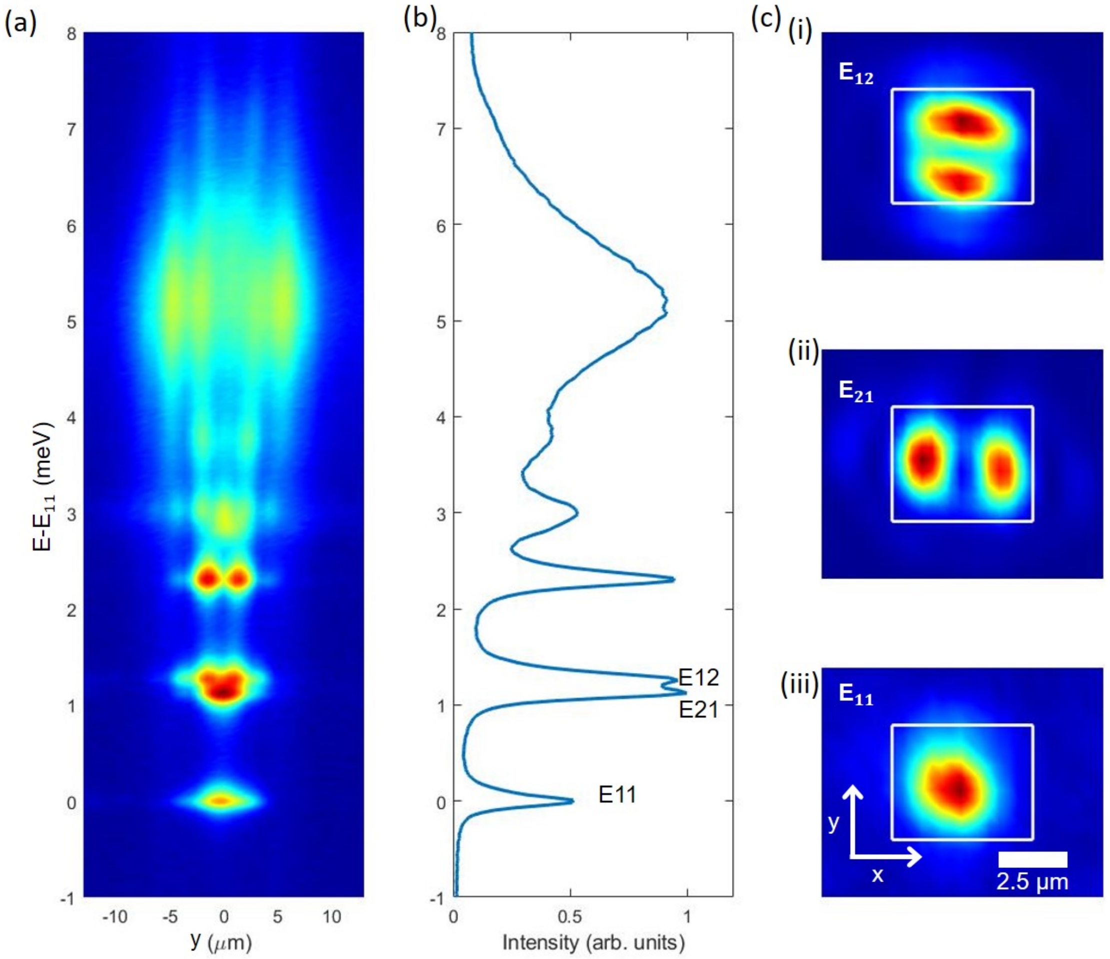

Figure 4.2: Characterisation of pillar A, non-resonantly exciting the pillar at 1550meV. E_{11}=1446 meV a) Polariton modes resolved in energy and x position at y=0. b) Integrated counts along the y direction of (a) with modes E_{11}, E_{12} and E_{21} labelled. c) Tomographic scans revealing the x and y intensities for modes; i) E_{12}, ii) E_{21}, iii) E_{11}.

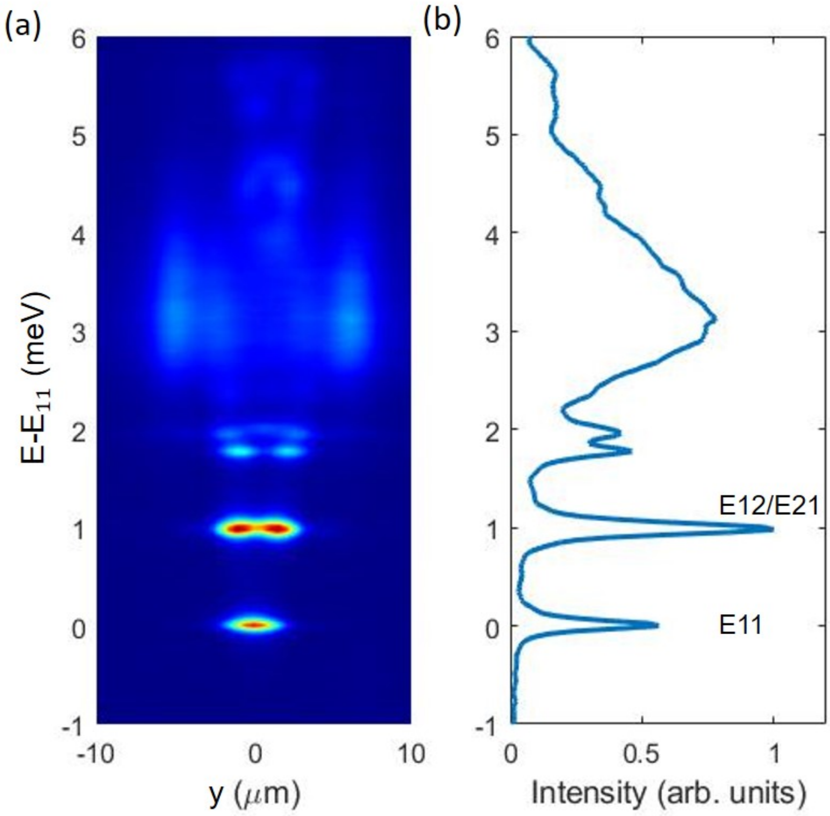

Figure 4.3: Characterisation of pillar B, non-resonantly exciting the pillar at 1550meV. E_{11}=1447 meV a) Polariton modes resolved in energy and y position at x=0. b) Integrated counts along the y direction of (a) with modes E_{11}, E_{12} and E_{21} labelled.

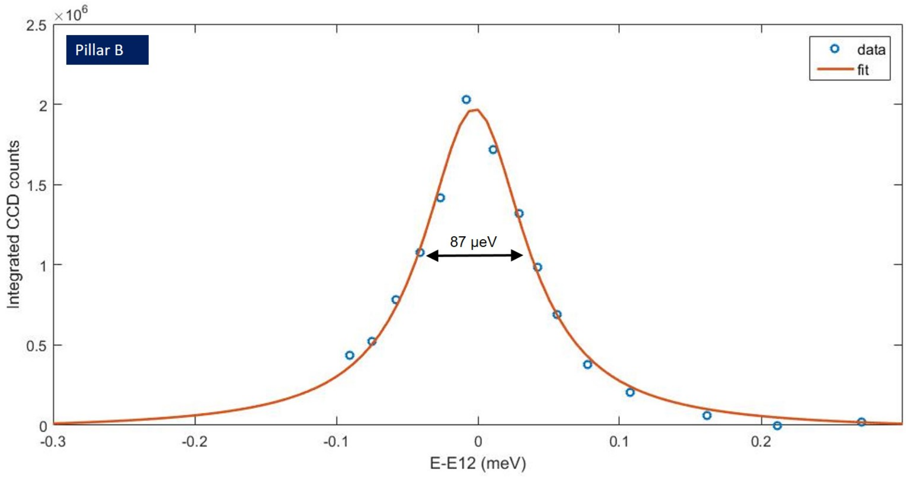

Figure 4.4: Resonant transmission linewidth measurement of pillar B E_{12} mode, with a Lorentzian fit to data points.

4.3 Experiment Design

In this chapter two experiments are presented, in both we identify the phase imparted from one polariton mode onto another. The only difference between the two experiments is that the first was done with a pulsed and continuous-wave laser, while in the second, two pulsed lasers were used. The former establishes a relationship between polariton number and the size of the nonlinear phase shift and how the control's polarisation affects the size of the phase shift. The latter shows how the size of the phase shift depends on the time between the two lasers arriving. There will be some minor experimental apparatus changes and analysis changes, but the core of the experiments remains the same.

As mentioned in the previous section, polaritons in micropillar devices will be the system used. The micropillar sample is the same as described in chapter 3. Two square micropillars are chosen with different excitonic fractions in each mode, see table 2.1. This will change the predicted and realised phase shift values. The ground E_{11} mode excitation will be referred to as the **control**, while the E_{12} excitation is referred to as the **signal**.

4.3.1 Pulsed signal and continuous wave control

Two lasers excite a square micropillar, each with a beam waist of $3\mu m$. The control laser is resonant with the E_{11} mode, while the signal laser is resonant with the E_{12} mode.

As discussed in chapter 3, tomographic scans reveal a Gaussian profile for the E_{11} mode while E_{21} and E_{12} have a two-lobed spatial profile. In order to achieve better coupling to the signal mode, a phase mask is included in its optical path. The mask introduces a π phase jump in the centre of the laser spot. This laser spatial profile matches E_{12} but not E_{21} as it has the wrong spatial symmetry. The control laser is sent to the E_{11} mode with a Gaussian spatial profile. The signal mode will be excited with horizontal polarisation $|H\rangle$, while the control mode excitation will have its polarisation and intensity modified. The polarisation and intensity in the E_{11} mode will affect the output polarisation from the E_{12} mode, as shown in figure 4.1f. This polarisation change will allow the phase shift imparted on the signal to be measured.

Looking at the electro-optic modulator, figure 2.6, a Glan-Thompson linear polariser is mounted at the exit port of the modulator. This polariser will reject one of the linearly polarised components. A QWP is placed after the LP, allowing right- to left-handed circular polarisation in the control laser. An illustration of the modified output is shown in figure 4.5. The laser is modulated into an **ON** and **OFF** intensity, with the rate set to 10kHz by a square wave control signal.

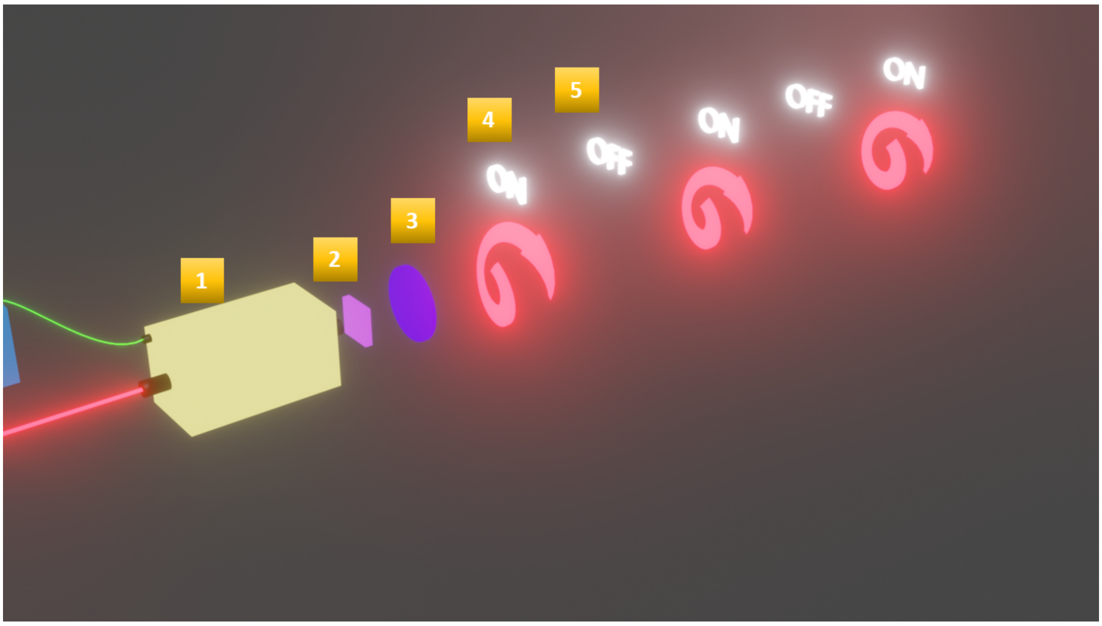

Figure 4.5: A schematic of using the EOM, LP and QWP to produce an ON and OFF light intensity. (1) EOM. (2) Glan-Thompson Linear polarizer. (3) QWP. (4) Circularly polarized light. (5) no light signal.

The control laser is exciting in this ON/OFF configuration, while the signal laser is resonant with the E_{12} mode. A HWP is used to change the signal to be $|H\rangle$ polarised. The lasers are combined onto the same optical axis to couple directly into the micropillar, a schematic of the excitation is shown in figure 4.6.

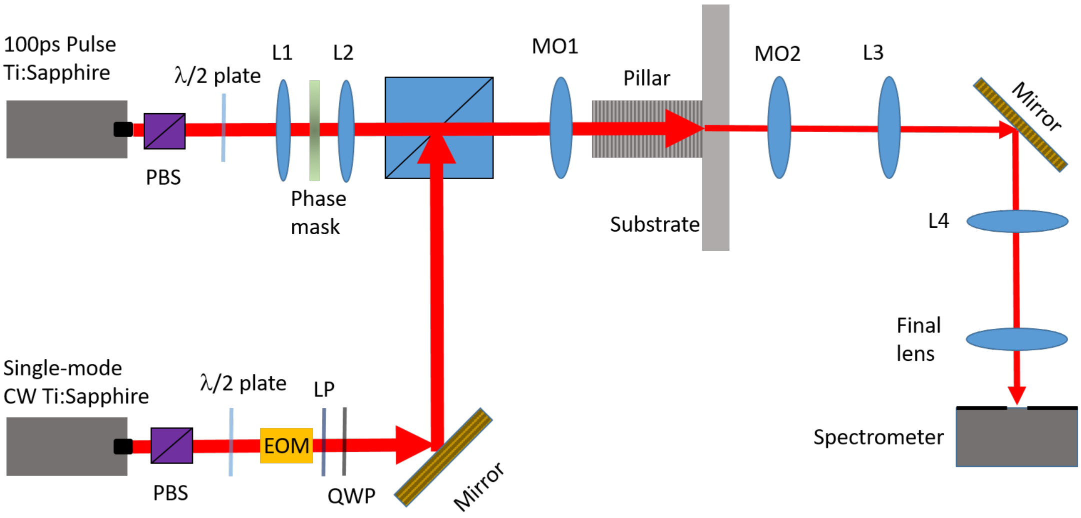

Figure 4.6: A schematic for the pump-probe measurement.

The light emitted is imaged on the CCD to establish the mode positions and adjust for the best coupling to the mode. The signal is then transmitted through the side panel spectrometer, as shown in figure 2.3. An output slit selects a small region of interest in wavelength, which corresponds to the E_{12} mode.

Figure 4.7 shows how the light is collected from the side panel of the spectrometer. A HWP rotates the linearly polarised signal into two equal components upon meeting the PBS. The signal focuses on two avalanche photodiodes (APDs) on each arm. The spectrometer output slit is moved to a narrow exit slit (0.5 mm), this blocks out the contribution of the control laser.

The following subsection shows how the photons are recorded and the experimental calculation of the phase shift.

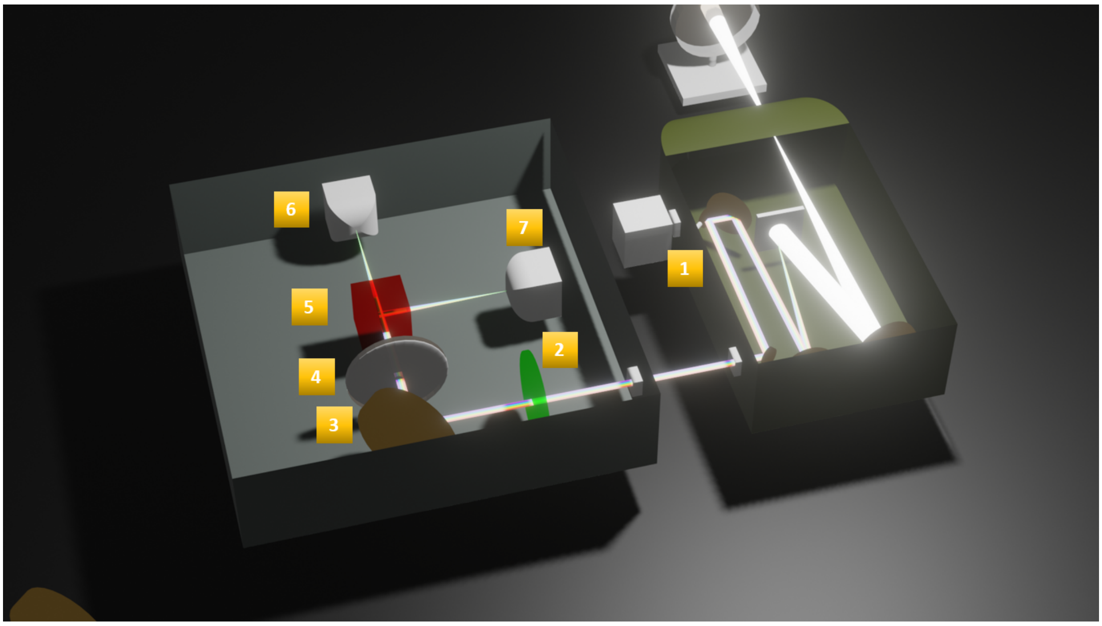

Figure 4.7: A schematic for the collection scheme for time-resolved photon detection. 1) The spectrometer. 2) A HWP. 3) A mirror. 4) Focusing lens. 5) A PBS. 6,7) APD.

4.3.2 Phase shift and photon counting

The signal laser excites the E_{12} mode. This laser has a pulse length of 100ps and a repetition rate of 80MHz (12.5ns). The polariton mode output is collected inside the photon counting box, where the signal polarisation is rotated such that the two arms of the APDs will have a balanced intensity. Both APDs register the maximum possible photon counts.

The photons recorded on each APD are counted by a Becker and Hickl SPC-630 photon counting card (time-correlated single-photon counting TCSPC). They are sorted by a router that encodes arrival time information relative to the incident laser pulses, with channels accumulating based on the EOM status. Four-channel outputs are displayed; $|A_{ON}\rangle$, $|A_{OFF}\rangle$, $|D_{ON}\rangle$ and $|D_{OFF}\rangle$. The ON subscript refers to the photon counts recorded by an APD when both the control and signal excite the device. The OFF subscript refers to when only the signal laser excites the system. The labels A and D label the polarisation basis, which are anti-diagonal and diagonal.

Starting with a balanced number of photons in each channel for a signal only measurement, then introducing the control laser, the count rate between the ON and OFF channels will change. The count rate change caused by leakage from the control beam can be minimised from spectrometer filtering and robustly subtracted for the continuous wave background in each channel. The signal was modulated at 80 MHz, while the control was 10 kHz. Allowing the separation of the signal and control, similar to lock-in detection.

The **S2** parameter is calculated in the $|A\rangle$ and $|D\rangle$ polarisation basis. Taking the $cos^{-1}(S2)$ gives the direction of the diagonal polarisation, now by calculating these parameters:

$$S_{ON} = \frac{D_{ON} - A_{ON}}{D_{ON} + A_{ON}}, \quad S_{OFF} = \frac{D_{OFF} - A_{OFF}}{D_{OFF} + A_{OFF}} \tag{4.1}$$

$$\phi_{ON} = cos^{-1}(S_{ON}), \quad \phi_{OFF} = cos^{-1}(S_{OFF}). \tag{4.2}$$

Where ϕ gives the angle of the diagonal polarisation, by taking the difference, we obtain the relative phase shift between the signal-control and signal only condition ϕ.

$$\phi = \phi_{ON} - \phi_{OFF} \tag{4.3}$$

4.3.3 Circular polarisation dependence CW control

To see what effect the control polarisation has on the signal phase shift value. The QWP in figure 4.5 is initialized with σ^+ polarisation and rotated in steps towards σ^- polarisation. At the midpoint, the control laser will be linearly polarised, with the results from pillar A shown in figure 4.8.

For pillar A, signal peak polariton numbers ranged from 5, while the control with 42, 4.2, 1.3 and 0.13 polaritons.

Clear trends emerge from figure 4.8ai-iv:

- The size of the phase shift is strongest at the lowest and highest QWP angles, $\sigma^+ = 46°$ and $\sigma^- = 136°$.
- The phase shift value changes sign between these circular polarisations, with the linearly polarised control laser phase value showing the lowest phase value.
- The magnitude of the phase shift value increases with the number of control polaritons.

The raw counts detected on the photon counting software and the signal-to-noise ratio (SNR(w)) metric are displayed in 4.8bi-iii. The window size (w) refers to the time range selected concerning the peak of each channel. The range of phase values is shown for all time window sizes.

The first and second trends are repeated in pillar B, figure 4.9a shows the result of signal peak polariton number of 5, with 2.5 polaritons set as the control polariton number. Figure 4.9a suggests that the size of the phase shift is correlated with the number of control polaritons.

The polarisation of the control laser affects the size and sign of the phase imparted on the signal. The following subsection will look at the phase shift as a function of the control polariton number.

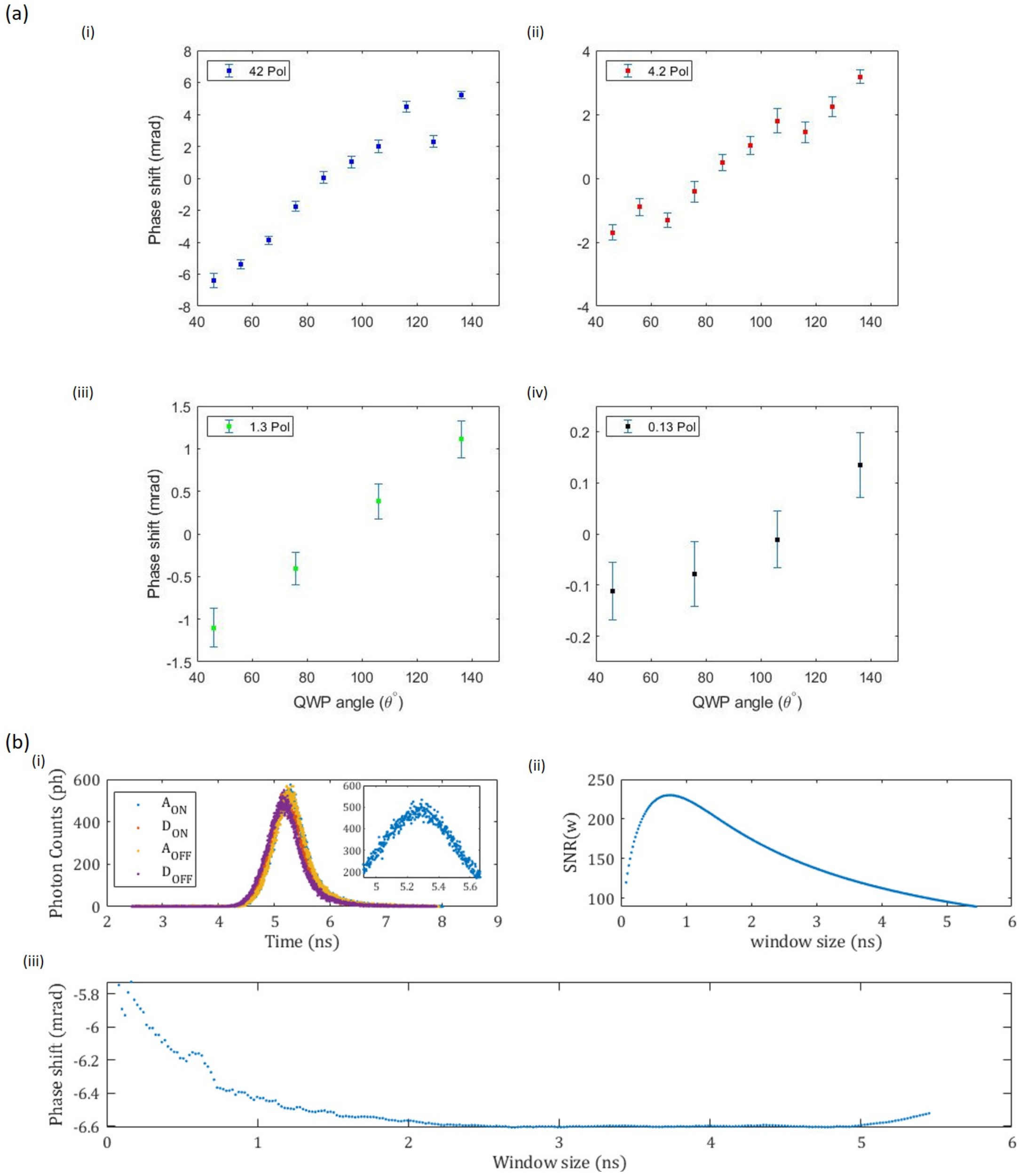

Figure 4.8: Pillar A phase shift in signal mode, N_S ∼5 polaritons, with CW control laser polarisation dependence. $\sigma^+ = 46^\circ$, $\sigma^- = 136^\circ$ ai) Control polariton number $N_C = 42$, aii) $N_C = 4.2$, aiii) $N_C = 1.3$, aiv) $N_C = 0.13$. bi) The raw channel output is seen in one acquisition of a phase shift measurement, with an insert showing the optimal SNR(w) window size. bii) SNR(w) for each window size. biii) The phase shift value for all window sizes is taken from the centre of the peak of the raw data, showing there is a small variation over the window integration.

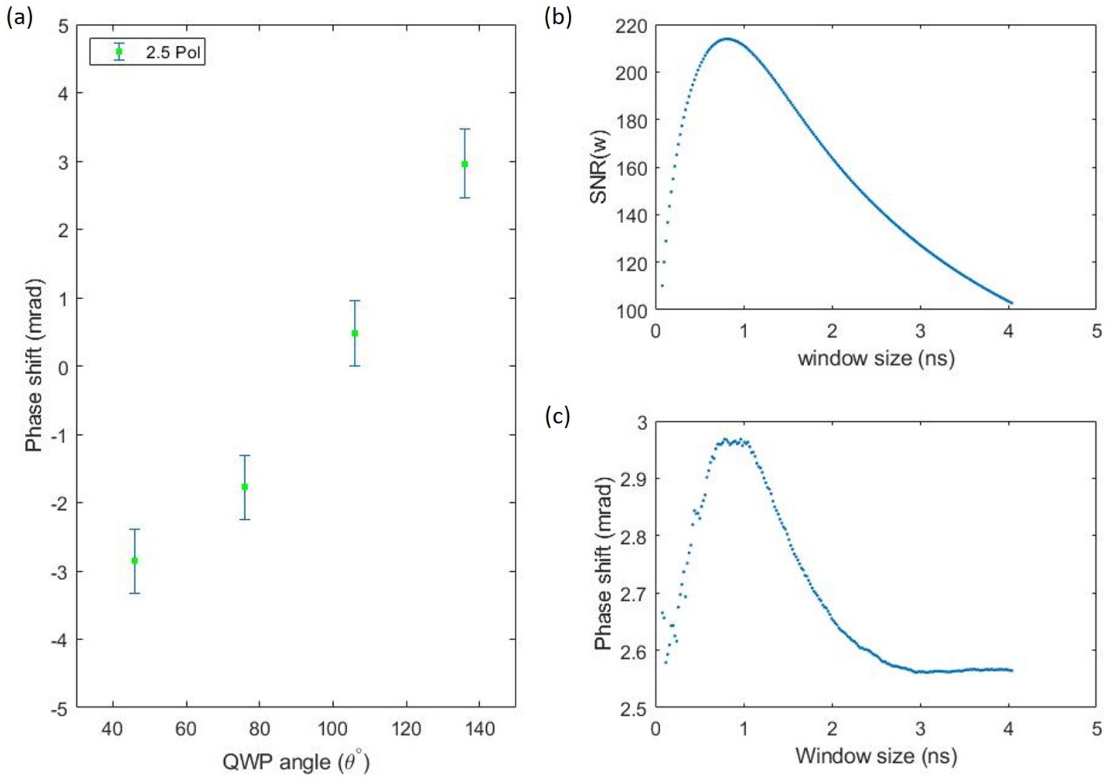

Figure 4.9: Pillar B phase shift in signal mode, N_S ∼5 polaritons, with CW, control laser polarisation dependence. σ^+ =46°, σ^- =136° a) Control polariton number $N_C = 2.5$. b) SNR(w) for each window size. c) The phase shift value for all window sizes is taken from the centre of the peak of the raw data, showing there is a small variation over the window integration.

4.3.4 Power dependence CW control

To investigate how the size of the phase shift changes with the control polariton number, N_C, we again look at pillars A and B. We chose σ^+ polarisation for the control beam. The results of the control power dependence for the same signal polariton number $N_S \sim 5$ can be seen for pillar A in figure 4.10 and B in 4.11.

Looking first at pillar A for N_C=0.13-43 polaritons. Starting from figure 4.10a going from 0.13 to 5.3, the phaseshift ϕ increases gradually with a slope of 0.5mrad per polariton. Around N_C =2.5, the phase shift begins to saturate gradually, and beyond $N_C = 5$, the values fall within the 95% confidence interval error. The phase shift value saturation was reproduced on the following day's measurement under the same experimental conditions. The absolute values change nominally upon repetition day-to-day. Small temperature fluctuations, sample drift and small discrepancies in power are reasons for these differences.

A similar situation is seen in pillar B. Figure 4.11a shows the full range of N_C used. There is a linear increase up until $N_C = 5$, with a slope of 3mrad per control polariton. The same saturation of the phase shift occurs, which happens at a larger phase shift value than in pillar A. Figure 4.11b plots a linear regression fit up to $N_C = 6$, with the smaller sample size considered in the fit. On pillar A at N_{pol} =0.13 a phase shift of $\phi = 0.13 \pm 0.07$mrad was observed.

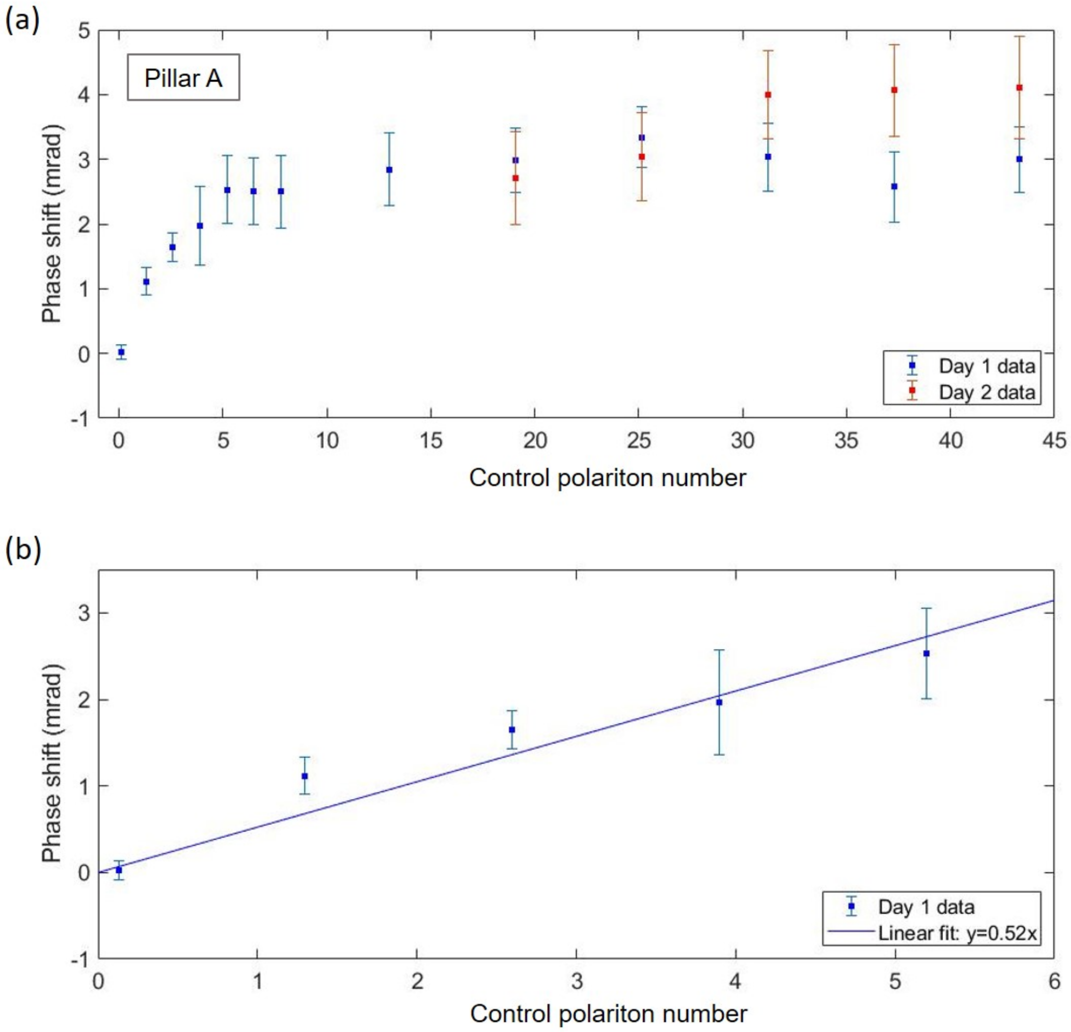

Figure 4.10: Pillar A control power dependence for $\mathbf{N_S \sim 5}$. a) The phase shift on the signal as a function of control polariton number, measured over two days. b) Linear regression fits up to the saturation of the phase shift value.

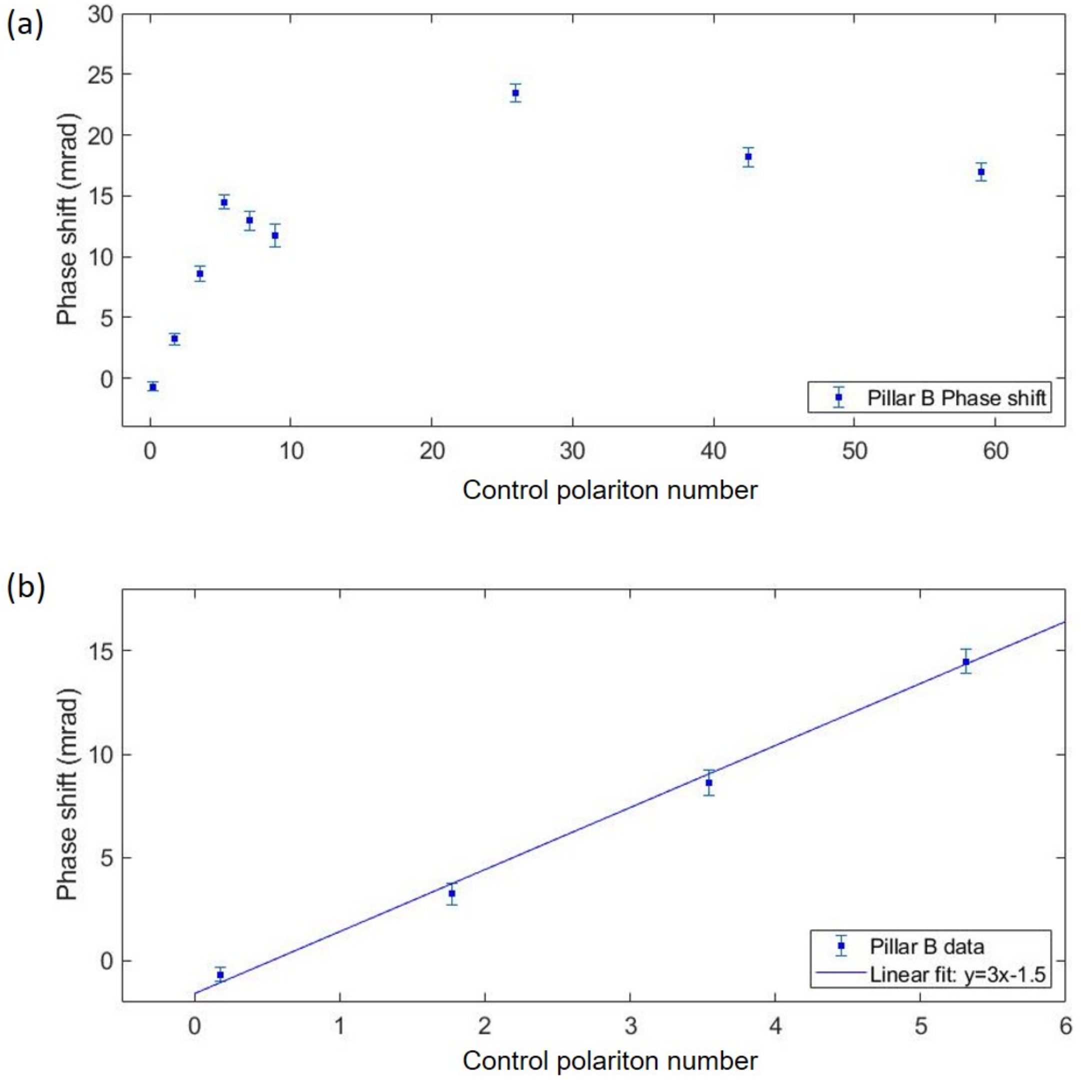

Figure 4.11: Pillar B control power dependence for $N_S \sim 5$. a) The phase shift on the signal as a function of control polariton number. b) Linear regression fits up to the saturation of the phase shift value.

4.3.5 Errors and phase shift value

Figures 4.8 and 4.9 displayed a signal-to-noise (SNR) function and a phase shift integration window dependence. The phase shift value calculated in accordance with equation 4.3. However, how does the integration window size on the channel affect the phase value extracted?

We use a metric that optimally selects the phase shift value based on the signal to the background level across the photon channels. The metric:

$$SNR(w) = \frac{\sum_{j=-w}^{j=+w} S_j}{\sqrt{\sum_{j=-w}^{j=+w} S_j} + (2w+1)S_D} \tag{4.4}$$

Where S_j is the sum of the signal in a channel, w is the window size, and S_D is the baseline count rate far away from the signal region. The optimum window size w is then taken from the maximum SNR(w), an example of the SNR(w) dependence shown in figure 4.8bii.

Each data point plotted in 4.8ai-iv is the mean value of the phase shift, calculated from a sample size of 500 to 8000 files. The files are recorded sequentially, with the dynamics of the polariton system resetting before each successive file.

The distribution of the phase shift values recorded from a sample of 5800 files in figure 4.12. The average phase shift is centred, with the standard error and 2∗(standard error) plotted for the normally distributed data set.

The mean and standard deviation is found for each data set. The standard error is calculated using a 95% probability interval of a t-distribution. A 95% confidence interval is applied to each mean phase value. The number of files measured for the very low polariton numbers is the upper limit for file collection. In most cases, the phase shift value is greater than the error.

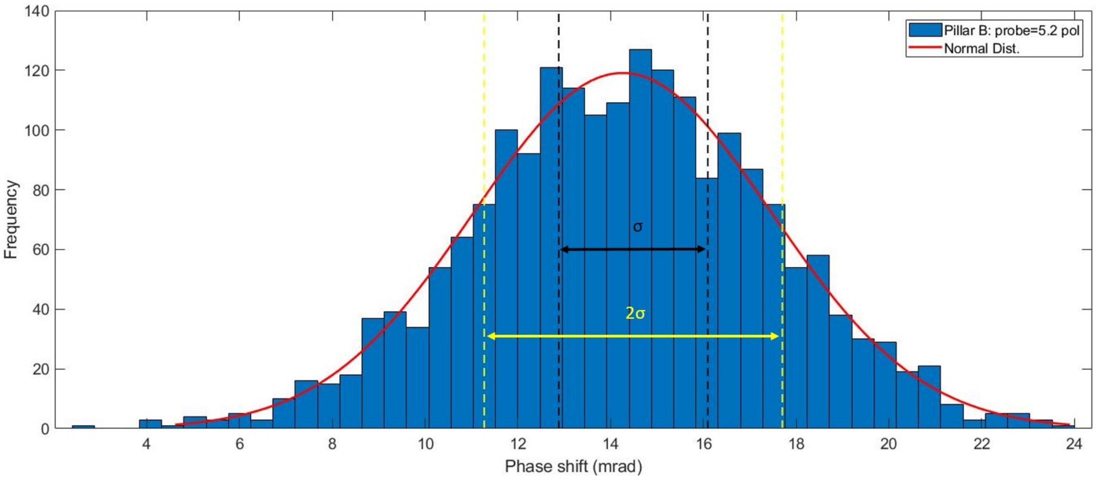

Figure 4.12: Histogram showing the distribution for all phase shift values.

The phase shift value was checked when no control beam was incident on the device, giving $\phi = 0$mrad. The signal and control were transmitted through the GaAs substrate, and we see no phase shift in the signal. A concern is a leakage from the control laser in the ON channels filtering into data processing. The slope of the background regions in the channels is checked to ensure there is no systematic background change across the integration window and subtracted.

Calibrating the 10kHz control beam by tuning the spectrometer grating allowed the laser wavelength to pass through the exit slit of the spectrometer. The counts in the ON and OFF channels are compared to ensure that the OFF channels are suppressed. When looking at the phase shift in the signal region, the spectrometer grating is tuned to allow the E_{12} mode through the exit slit. The APDs are balanced such that counts are approximately equal on each channel. A block is placed on the path of the control bream so that ON and OFF channels can be checked to ensure no difference between them.

So far, the data presented has shown that the CW control has imparted a phase shift on a signal state. The E_{11} mode population has changed the polarisation output from E_{12} mode. The control imparts the largest phase shift when the laser is circularly polarised.

4.4 Model for phase rotation in polariton micropillar

Dr. Paul Walker did the modelling and theoretical estimates for the phase shift in this system. The size of the nonlinear exciton and polariton frequency shifts with the system's energy scale. The transmission linewidth measurements are used for estimates. The signal laser has a pulse length longer than the decay rates of the E_{12} mode. The optical field inside the pillar approximately follows the incident pulses' temporal envelope. The signal laser has sufficient energy separation from the control (E_{11}) such that there is negligible coupling, so the two linewidths of the E_{11} and E_{12} do not overlap. E_{21} is ignored in the model since it is not excited due to having the wrong symmetry. The E_{12} state can be written as two orthogonal linear polarisation components, with the evolution given by:

$$i\frac{\partial u}{\partial t} = \mathcal{H}u + Pe^{-i\Delta_p t}, \tag{4.5a}$$

$$P = \begin{pmatrix} P_x \\ P_y \end{pmatrix}, \tag{4.5b}$$

$$u = \begin{pmatrix} u_x \\ u_y \end{pmatrix}, \tag{4.5c}$$

$$\mathcal{H} = \begin{pmatrix} w_{BS} + \frac{w_s}{2} - i\frac{\gamma}{2} & -i\frac{w_Z}{2} \\ i\frac{w_Z}{2} & w_{BS} - \frac{w_s}{2} - i\frac{\gamma}{2} \end{pmatrix}. \tag{4.5d}$$

Here, u_x and u_y are complex field amplitudes of the lower polariton states in two orthogonal polarisations. Since E_{12} has finite momentum in the y-direction, there will be TE-TM linear polarisation splitting parallel and perpendicular to the momentum, with w_s being the size of this splitting. γ is the linewidth of the E_{12} mode and Δ_p the signal detuning from the midpoint between the E_{12} polarisation splitting. In the case of pillars A and B, the splitting was not visible. P_x and P_y are the complex amplitudes of the signal laser polarisation.

The overall blueshift of both polarisation components and a frequency splitting in the E_{12} mode is given by w_Z, interpreted as an effective nonlinear magnetic field introduced by the number of circularly polarised control polaritons. w_{BS} is a frequency blueshift on all the states. The size of the blueshift and frequency splitting:

$$w_{BS} = 2|X_{11}|^2|X_{12}|^2\frac{(g_1+g_2)}{2A_{eff}}(n_+ + n_-), \tag{4.6a}$$

$$w_Z = 2|X_{11}|^2|X_{12}|^2\frac{(g_1-g_2)}{A_{eff}}(n_+ - n_-), \tag{4.6b}$$

$$\frac{1}{A_{eff}} = \frac{\int\int_{\infty}^{\infty} I_{11}I_{12}\cdot dxdy}{\int\int_{-\infty}^{\infty} I_{11}\cdot dxdy\cdot\int\int_{-\infty}^{\infty} I_{12}\cdot dxdy}. \tag{4.6c}$$

Where $|X_{11}|^2$ and $|X_{12}|^2$ are the exciton fractions of the E_{11} and E_{12} state. A_{eff} is the effective nonlinear area giving a measure of how much the two modes overlap each other in field intensity. The factor of 2 in the energy shifts is due to cross-modulation between modes of different frequencies [142]. Equation 4.5a can be solved to give the polarisation vectors and eigenvalues of the frequencies of $\mathcal{H}$:

$$u_x = \frac{P_x(w_{BS} - \Delta_p - i\gamma/2 - w_s/2) + iP_y w_Z/2}{(w_1 - \Delta_p)(w_2 - \Delta_p)}, \tag{4.7a}$$

$$u_y = \frac{P_y(w_{BS} - \Delta_p - i\gamma/2 + w_s/2) + iP_x w_Z/2}{(w_1 - \Delta_p)(w_2 - \Delta_p)}, \tag{4.7b}$$

$$w_1 = w_{BS} - i\gamma/2 + w_s\sec(\theta)/2, \tag{4.7c}$$

$$w_2 = w_{BS} - i\gamma/2 - w_s\sec(\theta)/2, \tag{4.7d}$$

$$\tan(\theta) = w_Z/w_s. \tag{4.7e}$$

Where w_1 and w_2 are eigenvalues of $\mathcal{H}$ giving the frequency of the modes split in polarisation. θ is a parameter that characterises the strength of the interaction induced by the circular polarisation splitting and the intrinsic pillar linear polarisation splitting. The nonlinear interaction changes the frequency and polarisation, making them slightly elliptical.

The light escaping from the pillar has the same polarisation as the internal micropillar polariton field. Therefore $(u_x,\, u_y)^T$ describes the polarisation state:

$$\begin{aligned}
S_1 &= \frac{\rho-1}{\rho+1}, && (4.8a)\\
S_2 &= \frac{2\sqrt{\rho}\cos(\phi_x-\phi_y)}{\rho+1}, && (4.8b)\\
S_3 &= \frac{2\sqrt{\rho}\sin(\phi_x-\phi_y)}{\rho+1}, && (4.8c)\\
u_x &= |u_x|e^{i\phi_x}, && (4.8d)\\
u_y &= |u_y|e^{i\phi_y}, && (4.8e)\\
\rho &= |u_x|^2/|u_y|^2. && (4.8f)
\end{aligned}$$

With the detectors measured in the $|D\rangle$ and $|A\rangle$ basis:

$$S_2 = \frac{|u_D|^2-|u_A|^2}{|u_D|^2+|u_A|^2} \tag{4.9}$$

The experimentally measured polarisation degree in terms of the state of the polariton is:

$$S_{expt} = \frac{2(w_Z)(\gamma/2)}{(w_{BS}-\Delta_p+w_S/2)^2+(\gamma/2)^2+(w_Z/2)^2} \tag{4.10}$$

Expressing the field in a circular polarisation basis, the relative phase between left and fight components is given by $\tan(\theta) = -S_2/S_1$:

$$\tan(\phi) = \frac{2(w_Z)(\gamma/2))}{(w_{BS}-\Delta_p+w_S/2)^2+(\gamma/2)^2-(w_Z/2)^2}. \tag{4.11}$$

Writing the control polaritons as $n_+ = n(1+\cos(2\theta_c))$ and $n_- = n(1-\cos(2\theta_c))$ for $0 \leq \theta_c \leq \pi/2$, then expanding S_{expt} and $\tan(\phi)$ to the first order in the total number of control polaritons n and considering small angles of ϕ we get:

$$\begin{aligned}
\Delta\phi &\approx S_{expt} \approx S_{max} f(\Delta_c,\theta_p), && (4.12a)\\
S_{max} &= \frac{2|X_{11}|^2|X_{12}|^2(g_1-g_2)n}{A_{eff}(\gamma/2)}, && (4.12b)\\
f(\Delta_p,\theta_c) &= \frac{(\gamma/2)^2}{\Delta_{eff}^2+(\gamma/2)^2}\cos(2\theta_c), && (4.12c)\\
\Delta_{eff} &= \Delta_p - w_S/2. && (4.12d)
\end{aligned}$$

The nonlinear phase shifts $\Delta\phi$ accumulated between circular components are given by the signal laser detuning from resonance, with a maximum value of S_{max}. It is proportional to the blueshift of one circularly polarised component of the E_{12} mode due to the circularly polarised E_{11} state. For more details of this derivation see the supplementary of Kuriakose et al. [2]

The trend in figure 4.8 and 4.9 going from negative to positive phase shift values, is explained by the θ_c, which physically represents the QWP angle. When $\theta_c = [0, \pi/4, \pi/2]$ are inserted $f(\Delta_p, \theta_p)$ takes a positive (σ^+) to negative (σ^-) value. With the phase shift value going to zero for linearly polarised control states.

The phase value saturates for pillars A and B remain constant over an extensive range of control polariton numbers. Further study is needed to identify the origin of this effect, but it could be due to thermal effects or exciton reservoir effects. Despite different excitonic fractions, the saturation in phase shift occurs at approximately the same N_C.

Finally, looking at equation 4.12b where we note that S_{max} is the maximum phase value ϕ. ϕ is measured in the power and circular dependence figures. When plotting the slope of $\phi(N_{pol})$ the $g_1 - g_2$ factor is found to be $11{\pm}4\mu eV\mu m^2$ and $10{\pm}4\mu eV\mu m^2$ for pillars A and B respectively [2]. These values are in agreement with established estimates in literature [35, 98].

4.5 Pulsed signal pulsed control measurement

In the previous set of phase shift measurements, a pulsed laser was used in the E_{12} mode (signal) while a CW laser excited the E_{11} mode (control). Under these conditions, the E_{11} mode is filled with N_C polaritons across the whole time of the ON condition. Using a pulsed laser as the control allowed us to measure the onset of the phase shift as a function of relative time between signal and control. $\phi(\tau)$ where τ is the signal time minus the control arrival time. To do this, we convert our CW laser into a pulsed laser by using the methods discussed in section 2.3.2.

We set the pulse length of the control to be 360ps, while the signal remains ∼100ps, though there is day-to-day fluctuation in signal pulse length. We test the pulse length of the control on a Streak camera, see figure 2.7, while an auto-correlator is used to check the signal pulse length.

In this study, the data acquisition is different to the previous experiment. The control laser takes the same form as discussed previously, the only difference being the removal of the linear polariser after the EOM. In this configuration, as shown in figure 4.13, a linearly polarised input it modulated between σ^+ and σ^-. We obtain the maximum phase rotation imparted on the signal state using this new configuration.

Mounting a retro-reflector on a stage where the optical path length can be increased or decreased, giving 1.1 ns of range. The lasers were transmitted through the GaAs substrate and filtered through the zero-order diffraction grating of the spectrometer. Measuring the arrival time difference between the control and signal. The 1.1ns range is insufficient to measure the behaviour before and after the signal arrives.

We use four different electronic cable delays between the laser reference signal

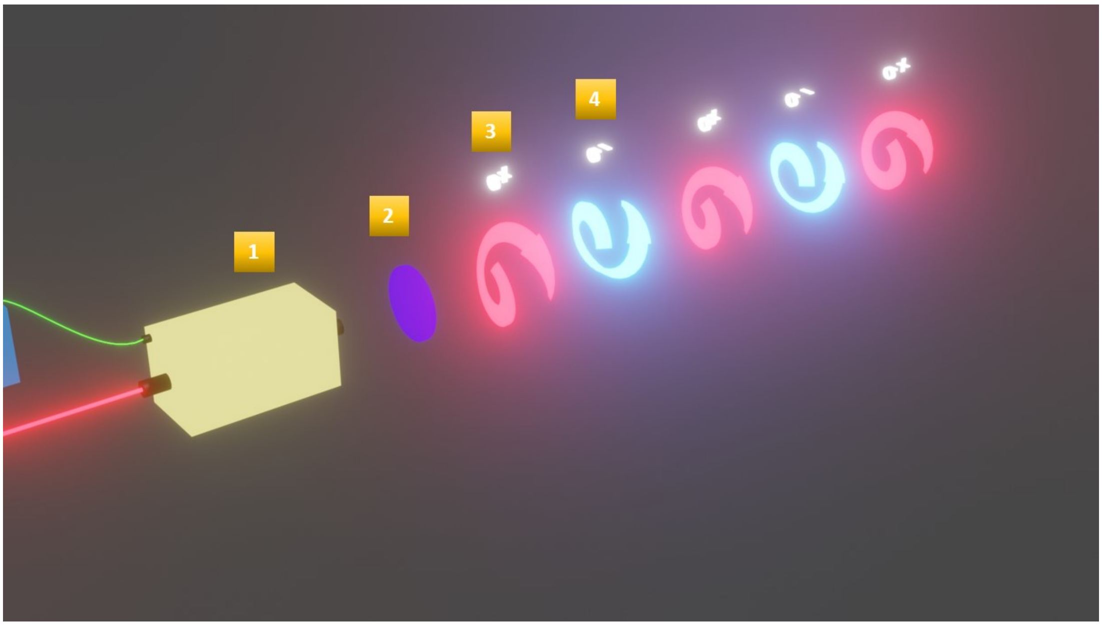

Figure 4.13: A schematic of the EOM and QWP. The control beam is modulated between σ^+ and σ^- light. (1) EOM. (2) QWP. (3) σ^+ light. (4) σ^- light.

and the EOM. The control laser is locked to the 80MHz repetition rate of the signal laser. By increasing the delay from this reference, the control laser arrival time gets closer or further from the signal arrival time. Pillar B is used for this study because the phase shift values were five times larger than pillar A.

4.5.1 Results

Using a peak control polariton number N_C ~5.7, the control to signal arrival time is tested between -1.4ns and +1.5ns. The signal mode is filtered through the spectrometer and collected on the two APDs with the $|D\rangle$ and $|A\rangle$ polarisation basis, with the signal excited with $|H\rangle$ polarisation. The measurements were done over two days with four different electronic delays used. Different colour indicates each set on figure 4.14. This data shows that when the control and signal beam arrive far away from each other ±800 ps, the phase shift value decreases. The most substantial phase shift value is within the central region, peaking between -100 ps to 350 ps. Each set of measurement configurations overlaps relative time between old and new measurements. The phase shift value should be approximately twice as strong as in these measurements since we modulate between right and left circular polarisation.

Taking the maximum absolute value of $|\phi(\tau)|$ gives a value of $\sim$6mrad. Compared to the CW measurement done in pillar B, figure 4.11b, the straight-line fit predicts a phase shift of $\sim$15.6mrad. When factoring in that we expect this phase shift to be double in size, the pulsed measurements have a phase shift 1/5th of the strength of the CW case.

There is more variance in the phase value point-to-point, where some values contradict the trend of rising to about $\tau \sim 0$ ns. This inconsistency may be due to the signal laser phase instability. This is caused by the change in the relative arrival time between the signal and control laser. Minor energy frequency drifting of the signal laser exacerbates the relative time and the actual phase value observed. If the signal laser red or blue detunes from the centre of the Zeeman splitting of the E_{12} mode, then we expect the value to reduce. With the experimental setup used, it is not possible to monitor the energy of the control laser while measuring on the APDs.

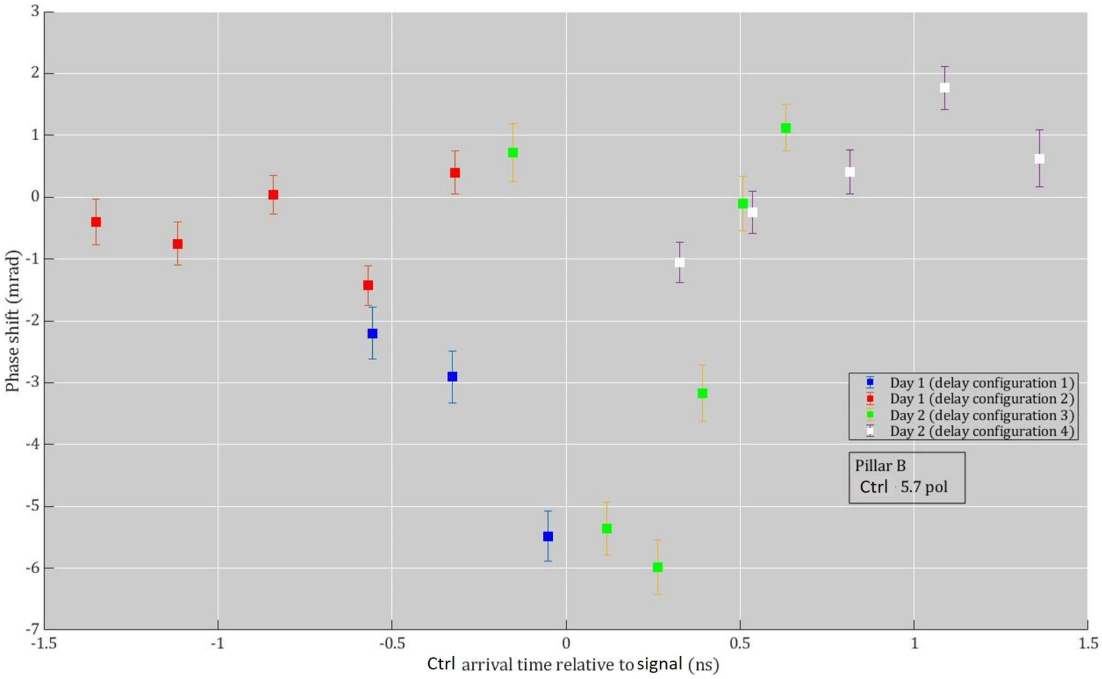

Figure 4.14: Control arrival time relative to the signal.

4.5.2 Analysis for delay signal-control result

Obtaining the phase value takes same form as the CW control measurement, we calculate the relative change in polarisation using the S_2 parameter. $\phi = arccos(S_{\sigma^-}) - arccos(S_{\sigma^+})$ is the new calculation. The quantities S_{σ^-} and S_{σ^+} are found by looking at the channel outputs for $|D_{\sigma^+}\rangle$, $|D_{\sigma^-}\rangle$, $|A_{\sigma^+}\rangle$ and $|A_{\sigma^-}\rangle$ are the new channels recorded, using equation:

$$S_{\sigma^{+,-}} = \frac{D_{\sigma^{+,-}} - A_{\sigma^{+,-}}}{D_{\sigma^{+,-}} + A_{\sigma^{+,-}}}. \tag{4.13}$$

To calculate the error on each phase shift value, we use the same method as before in section 4.3.5. We are using a sample size of ~ 500. The main difference is in the background subtraction for each collection channel. There is no longer a flat background contribution to each channel from the control on the APDs. Since this contribution is not equal across all the collection time bins, we can not do a simple straight line fit background subtraction.

Instead, we collect the control beam using the same collection time but with a block placed in the signal excitation path, collecting a sample size of $\sim$20. An average background for each time bin is then subtracted from the signal-control measurement to suppress the control contribution. The grating is tuned to zero-order with the control and signal measured and fitted with Gaussian functions to obtain the time difference.

4.6 Discussion

We have shown that even at less than one average polariton number in the control beam, $N_C = 0.13$ that $\phi = 0.13 \pm 0.07$mrad is possible. We demonstrated that the CW control could impart a phase shift on the signal on two separate devices. The polarisation of the control strongly affects the strength of the phase shift onto the linearly polarised signal. This result was explained in the model for XPM in our device.

Pillar A has a slope of 0.5mrad per polariton before the saturation occurs, while pillar B had a phase shift of 3mrad per polariton. Pillar B has 7.2x larger $|X_{11}|^2|X_{12}|^2$, which is why we see a larger phase shift imparted on the signal. The phase shift value saturation occurs in CW power dependences on both pillars. Further experiments are required to identify the mechanism behind this saturation. Even when the saturation of the phase has occurred, the polarisation dependence in figure 4.8ai is maintained. Updating table 4.1:

System	**ϕ per particle (mrad)**
Rydberg atoms in EIT [129]	500
Single Cs atom [137]	280
Strongly coupled quantum dot [131]	220
Single polariton micropillar[2]	**3**
Rb vapour in hollow core fibre [138]	0.3
Metastable Xe [139]	0.0003
Photonic crystal fibre [140]	0.0001

Table 4.2: Updated phase shift values in platforms reported in literature.

Our phase shift of 3mrad per polariton is an order of magnitude larger than the nearest competing system that does not use atom-like emitters. QDs grown by spontaneous nucleation have a random spatial and frequency distribution. Therefore, face scalability challenges for multiple identical phase shift sites at predetermined locations. Similar arguments could be made for energy tuning on devices shown in the micropillar system, as can be seen in the energy differences in the E_{11} and E_{12} modes in chapter 3.

Our result can be a stepping stone for other systems to attempt better phase shift values. Dipolar- [143] and trion-[21] polaritons have more considerable interaction strength, which make them an exciting platform for further research.

The second experiment shown in this chapter involved a pulsed signal and control laser; these are an initial set of measurements. More measurements are required to obtain a clear relationship between the phase shift onset and the temporal overlap between the signal and control, see figure 4 in Matsuda et al. [140]. Pulsed measurements avoid CW heating related effects and would allow further investigation into the saturation of the phase shift value at a higher control polariton number [144].

In the final chapter of this thesis, the outlook of our work is discussed, the CPHASE gate is introduced and an existing polariton platform that could improve on the results presented in this thesis. This is the fibre cavity system that produced weak anti-bunched light in an exciton-polariton system[31].

Chapter 5

Optical analogue of a Dresselhaus field in polariton graphene

5.1 Introduction

Spin-orbit (SO) interactions of electrons in a semiconductors are determined by their crystalline structure. In atomic physics, SO interaction leads to the splitting of atomic energy levels. In semiconductors SO interactions are felt by electrons within a lattice, it generates an effective magnetic field that is created by the electrons motion.

In semiconductors such as GaAs there are two types of SO interactions, called, Rashba and Dresselhaus. Rashba SO interactions occur when there is structural inversion asymmetry which is related to the growth process, while Dresselhaus SO interactions arise from inversion asymmetry that is present in the crystal lattice, related to the fact that there is no inversion centre in a cell. Both of these SO interactions give a different effective magnetic field experienced for electrons in a material such as GaAs, with the field textures shown in figure 5.1. By tuning the strengths of these interactions, persistent spin helix's have been observed [145], effects that look to manipulate the strengths of SO interactions in solids have applications in spintronics [146].

In suitably designed structures, the Hamiltonian of the system is engineered [147] to give particles without a magnetic moment the experience of a SO interaction, or an *effective SO coupling*. Photons were a primary candidate for this area of study, with an effective magnetic field produced by coupling a two-dimensional array of optical-ring resonators in a waveguide geometry [148]. In another proposal, introducing inhomogeneous strain on graphene produced similar effects to that of an external magnetic field [149]. The photonic analogue realised by Rechtsman et al. [150] and demonstrated highly degenerate levels of transverse optical confinement in *photonic Landau levels*.

Throughout this thesis, experiments have been concentrated on the study of

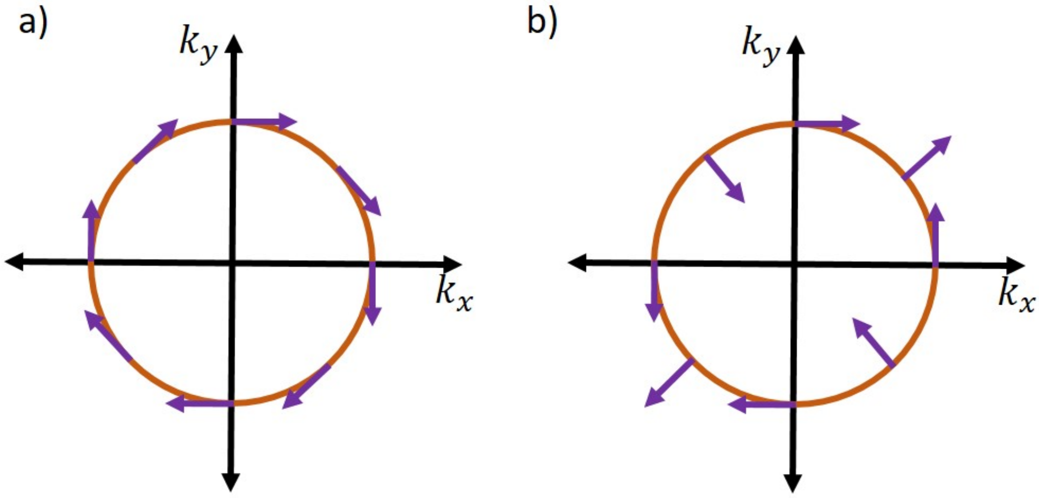

Figure 5.1: SO interactions experienced by an electron in GaAs. a) The direction of the effective magnetic field experienced by an electron for a given momentum for Rashba SO coupling. b) The direction of the effective magnetic field experienced by an electron for a given momentum for Dresselhaus SO coupling.

light leaving a single micropillar structure. Many different research groups have etched planar microcavities into single, dimerised [81], Kagome [83], Lieb [82] and honeycomb lattices [84] - figure 5.2.

Creating coupling between the photons' intrinsic spin (pseudospin) and strong spin-dependent polaritons interactions makes the simulation of many-body effects a potential [151]. This chapter presents the formation of polarisation patterns resulting from the coupling between the photon's spin and in-plane momentum. The polarisation pattern takes the form of an optical analogue of Dresselhaus SO coupling. This Dresselhaus-type field occurs at the Dirac points in the honeycomb lattice Brillouin zones. Pillars are joined together and partially overlapped to create the honeycomb lattice geometry.

In this chapter, the rich polarisation texture of the honeycomb lattice Brillouin zone is presented. Using the experimental techniques such as, tomographic scans, resolving in polarisation, non-resonant and resonant excitation the TE-TM field texture is analysed at the high symmetry points of the lattice. By resonantly exciting the lattice at the Γ point, we see the conventional TE-TM field texture for a planar microcavity. In planar cavity systems, the TE-TM effective field has a k^2 scaling and a double azimuthal dependence, as shown in section 1.5.2. At the K-K′ points of the Dirac cone dispersion, we observe a clear two domain splitting in circular polarisation for an initially linearly polarised state, which is a signature of the Dresselhaus symmetry predicted in Nalitov et al. [3].

The chapter is presented in a paper format, refer to reference [4] and its supplementary material for the version inserted in this thesis, ***Reproduced with permission from Springer Nature.***

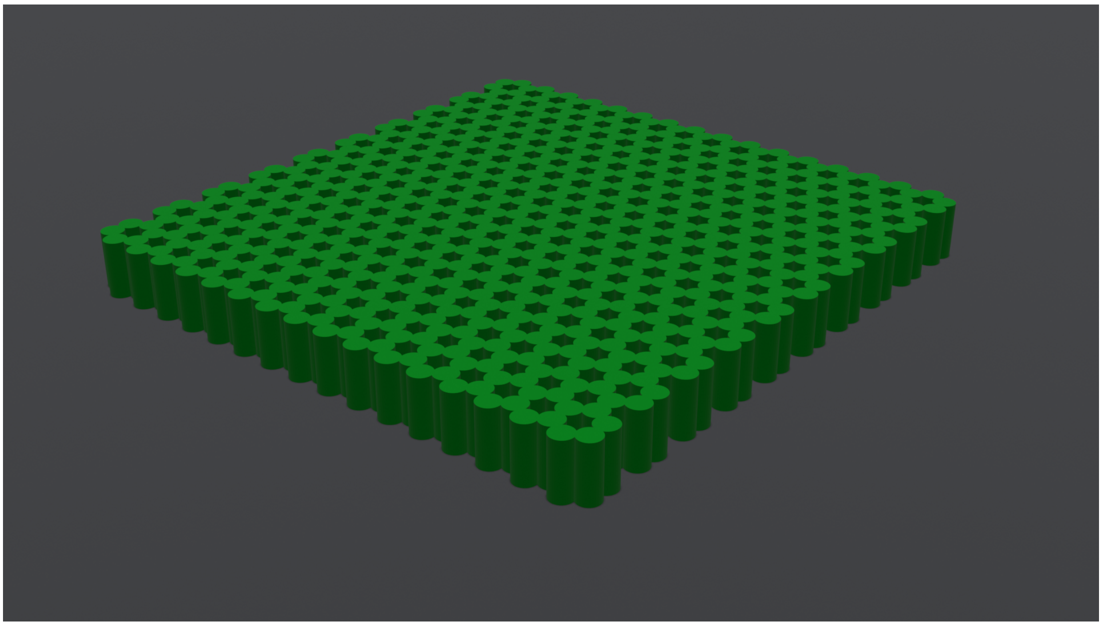

Figure 5.2: Honeycomb lattice.

5.2 Optical analogue of Dresselhaus spin-orbit interaction in photonic graphene

nature photonics
LETTERS
https://doi.org/10.1038/s41566-020-00729-z

Optical analogue of Dresselhaus spin–orbit interaction in photonic graphene

C. E. Whittaker[1] ✉, T. Dowling[1], A. V. Nalitov[2,3,4], A. V. Yulin[4], B. Royall[1], E. Clarke[5], M. S. Skolnick[1,4], I. A. Shelykh[3,4] and D. N. Krizhanovskii[1,4] ✉

The concept of gauge fields plays a significant role in many areas of physics, from particle physics and cosmology to condensed-matter systems, where gauge potentials are a natural consequence of electromagnetic fields acting on charged particles and are of central importance in topological states of matter[1]. Here, we report on the experimental realization of a synthetic non-Abelian gauge field for photons[2] in a honeycomb microcavity lattice[3]. We show that the effective magnetic field associated with transverse electric–transverse magnetic splitting has the symmetry of the Dresselhaus spin–orbit interaction around Dirac points in the dispersion, and can be regarded as an SU(2) gauge field[4]. The symmetry of the field is revealed in the optical spin Hall effect, where, under resonant excitation of the Dirac points, precession of the photon pseudospin around the field direction leads to the formation of two spin domains. Furthermore, we observe that the Dresselhaus-type field changes its sign in the same Dirac valley on switching from *s* to *p* bands, in good agreement with the tight-binding modelling. Our work demonstrating a non-Abelian gauge field for light on the microscale paves the way towards manipulation of photons via spin on a chip.

Gauge fields are central to the description of fundamental forces and can carry profound physical consequences. In the case of electromagnetism, for example, the significance of the magnetic vector potential $\mathbf{A}$ is revealed by a quantum-mechanical phase shift experienced by charged particles in the celebrated Aharonov–Bohm (AB) effect. Although this is a manifestation of a U(1) Abelian gauge field with scalar components, there also exist spin-dependent vector potentials with non-commuting components (first considered by Yang and Mills), that is, SU(2) non-Abelian gauge fields[5]. In condensed-matter physics, the non-Abelian framework is also highly relevant[6], in particular to the theory of spin–orbit coupling (SOC) in solids[7,8], which plays an indispensable role in the family of spin Hall effects[9], topological insulators and superconductors[1], as well as the operation of spintronic devices[10]. On the other hand, photons—neutral particles with zero magnetic moment—can also behave as if affected by both Abelian and non-Abelian gauge fields in suitably designed environments[11]. These allow the exploration of gauge field Hamiltonians in the optical domain, and a means of manipulating light trajectories and internal degrees of freedom such as spin (polarization) for spinoptronic signal processing applications[12]. Abelian gauge fields have been engineered in diverse platforms including silica waveguides[13], metamaterials[14], silicon ring resonators[15,16] and liquid-crystal optical cavities[17]. By contrast, the realization of non-Abelian gauge fields in photonic microstructures and thus enabling manipulation of light via spin on a chip remains a significant challenge.

One possible way to implement artificial non-Abelian gauge fields on the microscale in a monolithic structure is to use the reduced spatial symmetry of birefringent[18,19] or laterally patterned[4,20] semiconductor microcavities along with native transverse electric–transverse magnetic (TE–TM) splitting (photonic SOC). Honeycomb lattices are of particular interest, because they provide access to the physics of graphene and related materials, including the Dirac dispersion[3], edge states[21] and influence of strain[22], all in a controlled photonic environment in which some of the limitations of real graphene can be overcome. Importantly, although graphene itself suffers from small SOC, which prevents observation of the spin Hall effect, the photonic SOC can be enhanced in wavelength-scale photonic lattices[23,24], enabling the physics of non-Abelian gauge fields in graphene geometries to be explored.

In this Letter, we utilize a patterned GaAs-based microcavity with a honeycomb lattice geometry (Fig. 1a)—that is, photonic graphene—to study the influence of photonic SOC on the dispersion. In this setting (see Methods for sample details), which was previously considered theoretically in ref. [4], the interplay between the SOC and the reduced spatial symmetry imposed by the lattice transforms the double winding effective magnetic field associated with TE–TM splitting into a Dresselhaus-type field with a single winding locally around the Dirac points, which can be described in terms of a non-Abelian gauge field. Here, we visualize the field texture around these high symmetry points, and further confirm the Dresselhaus symmetry by the optical spin Hall effect (OSHE) revealing the formation of two cross-polarized spin domains. Our results are in good agreement with the theory presented in ref. [4] and demonstrate the potential for engineering artificial gauge fields for photons in different orbital bands using model two-dimensional (2D) lattice systems. Finally, we note that the non-Abelian AB effect has been observed recently by cascading non-reciprocal optical elements in a fibre-optic set-up (that is, not on the microscale and governed by physical mechanisms that are very different from those reported in the present manuscript)[25].

To measure the dispersion relation of our sample we use low-power incoherent excitation to populate all modes. The band structure features linear Dirac crossings at characteristic momenta, namely the K and K′ points at the Brillouin zone (BZ) corners (Fig. 1b), which are visible in the angle-resolved photoluminescence (PL) spectra shown for the fundamental *s* bands and higher-energy *p* bands plotted along high-symmetry directions in Fig. 1c,d (different slices of momentum space are selected for maximal

---

[1]Department of Physics and Astronomy, University of Sheffield, Sheffield, UK. [2]Faculty of Science and Engineering, University of Wolverhampton, Wolverhampton, UK. [3]Science Institute, University of Iceland, Reykjavik, Iceland. [4]ITMO University, St Petersburg, Russia. [5]EPSRC National Epitaxy Facility, University of Sheffield, Sheffield, UK. ✉e-mail: charles.whittaker@sheffield.ac.uk; d.krizhanovskii@sheffield.ac.uk

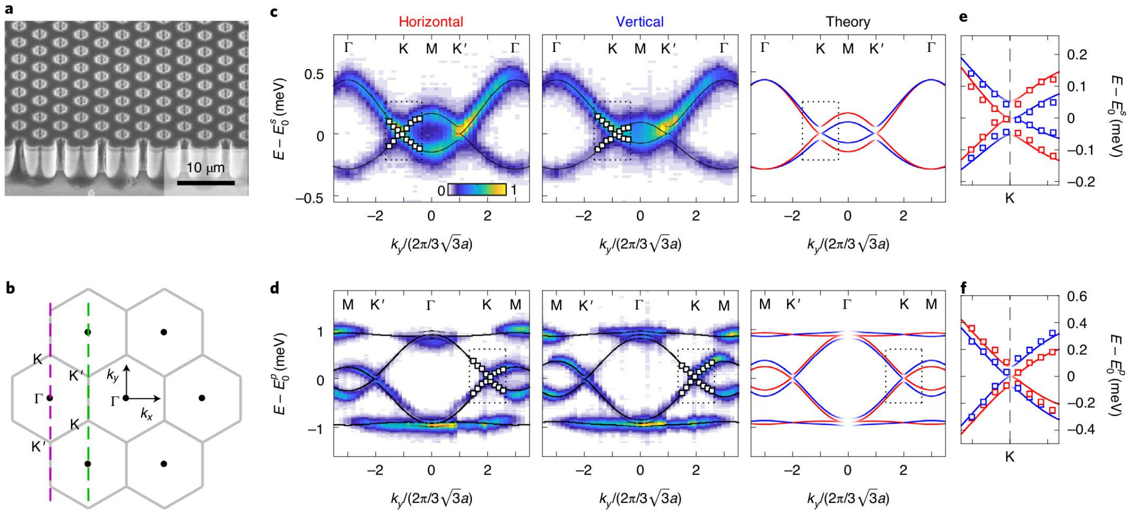

Fig. 1 | Photonic graphene sample and dispersion relations. a, Scanning electron microscope image of the honeycomb lattice. **b**, Schematic of the reciprocal space lattice. **c**, Polarization-resolved PL spectra showing *s* bands along the dashed green line in **b** with tight-binding (TB) calculations (solid curves). Left: horizontal polarization (H). Middle: vertical polarization (V). The white squares inside the dotted rectangles show the peak positions extracted from the experimental data. Right: corresponding polarization-resolved dispersion relation calculated by the TB model. E_0^s is 1.4551 eV. **e**, Zoom-in on the dotted rectangles in **c**. The red and blue squares (lines) show the experimental (theoretical) horizontal and vertical dispersions, respectively. **d**,**f**, Same as in **c** and **e** but for the *p* bands, shown along the purple dashed line in **b**. E_0^p is 1.4582 eV. *a* is the lattice constant.

signal intensity; Supplementary Section 5). By resolving the emission in linear polarization, the orientation of the TE–TM splitting effective magnetic field at each energy and momentum can be revealed, because it corresponds to the pseudospin of the eigenstate. Hence, to characterize the pseudospin texture and therefore the field orientation across momentum space, we measure the first two Stokes parameters S_1 and S_2 of the emission (Methods). For both *s* and *p* bands, a pronounced splitting between TE and TM modes (which have horizontal (H) and vertical (V) polarization for the directions plotted) is visible, which is well described using a TB formalism including SOC as in refs. [4,26] (Methods). Importantly, the pseudospin changes sign as the *k* vector passes through a Dirac point, as we show using a zoom on the K point. This suggests that, locally, around a K or K′ point the dependence of TE–TM splitting on momentum differs from that found in a planar cavity around $\mathbf{k} = 0$. To study this polarization behaviour in more detail, we constructed 2D energy-resolved polarization maps using tomographic imaging (Methods).

First we will focus on the *s* bands. In Fig. 2, we see 2D maps of the linear polarization angle ϕ in momentum space, calculated as $2\phi = \arctan(S_2/S_1)$. For the Γ point, which corresponds to the emission around $\mathbf{k} = 0$ at the energy minimum of the dispersion, a quadrupole pattern can be seen (Fig. 2a). Arrows showing the pseudospin texture (orientation of the effective magnetic field) reveal the familiar dipolar field associated with TE–TM splitting in microcavities. Figure 2c,e shows the corresponding maps at the energy of the Dirac points. In contrast to the Γ point, the local symmetry around K and K′ no longer has a double azimuthal dependence. Rather, there is a single winding of the pseudospin with the characteristic texture of a Dresselhaus-type field[27]. We note that the local effective magnetic fields have opposite sign around the K and K′ points, although the direction of field rotation is the same (counter-rotating with the azimuthal angle). These features can also be seen clearly in calculations using the TB model of ref. [4] (Fig. 2b,d,f), where there is excellent agreement with the experiment. As we show in the Methods, using a suitable minimal coupling transformation the observed effective field around the Dirac points can be described in terms of a non-Abelian gauge field with non-commuting components. By contrast, around the Γ point, the SOC has the same form as for unpatterned microcavities and cannot be described in terms of a synthetic gauge field.

One of the clearest manifestations of the effective magnetic field acting on photons is the formation of spin currents in the OSHE, caused by pseudospin precession around the *k*-dependent effective magnetic field[28]. At a given energy, the wavevector and polarization of the injected light can be used to control the spin texture of the emission, because the pseudospin rotation depends on the relative angle between its initial direction and the effective field. We use this knowledge to unveil the different symmetries shown in Fig. 2 by imaging the time-integrated real space emission of our sample under continuous optical excitation at the Γ, K and K′ points with a linearly polarized pump. We vary the energy and angle of the incoming laser to excite these points in the dispersion and measure the resulting emission intensity in right and left circular polarizations to determine the Stokes parameter S_3 (Methods). In Fig. 3a we show how resonant excitation at the Γ point under H-polarized excitation indeed leads to the observation of four domains with alternating circular polarization, confirming that at the energy minimum of the dispersion, at the centre of the BZ, the effective magnetic field in Fig. 2a has the same form as that of conventional planar microcavities[4,29]. In contrast, under H-polarized pumping at the K point (Fig. 3c), only two domains are seen, formed to the left and right of the pump spot and with opposite circular polarizations as expected from the Dresselhaus symmetry surrounding the Dirac points (Fig. 2c,e). This is expected, because the injected pseudospin vector lies parallel/anti-parallel to the field direction along the k_y axis in the locally excited region of momentum space, so there should be no evolution of the pseudospin along *y*.

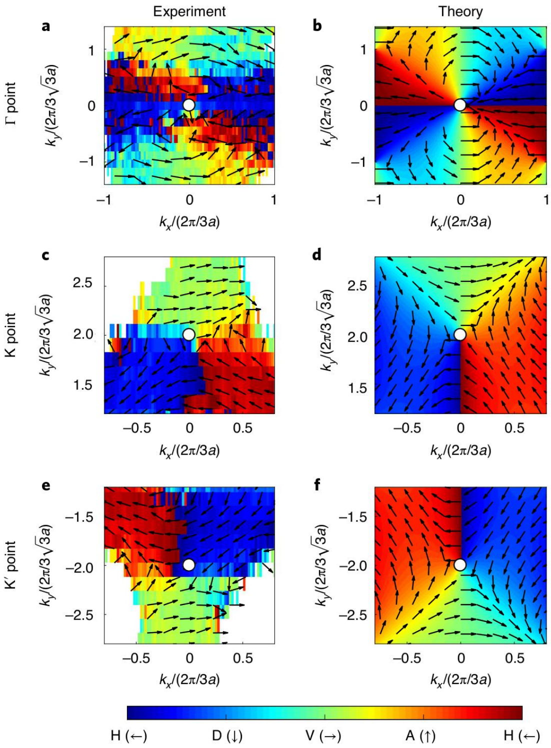

Fig. 2 | Texture of the effective magnetic fields surrounding Γ, K and K′ points. **a**,**c**,**e**, Experimental momentum space maps of ϕ at the energy of the Γ point (1.4547 eV) and K and K′ points (1.4551 eV), respectively, with arrows representing the pseudospin vector. White regions correspond to low signal intensity (<5% of maximum). **b**,**d**,**f**, Corresponding calculated momentum space maps of ϕ at the energy of the Γ, K and K′ points, respectively, with arrows representing the pseudospin vector. D and A denote diagonal and anti-diagonal polarizations, respectively. Note that the lowest and highest values on the colour scale correspond to the same polarization.

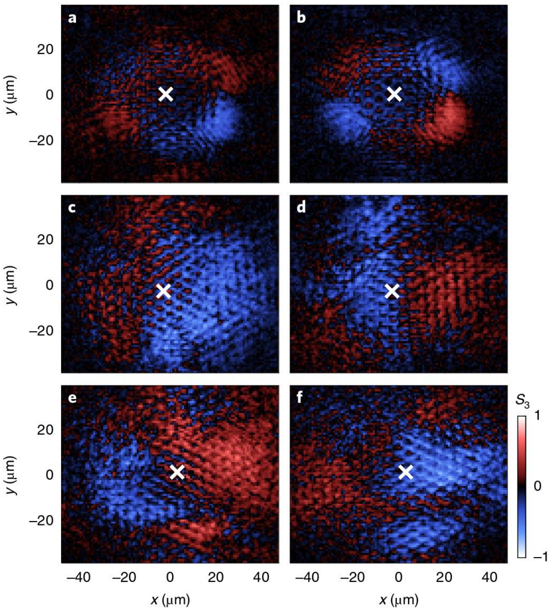

Fig. 3 | Observation of the OSHE. **a**,**c**,**e**, Measured real-space circular polarization degree S_3 under resonant excitation at the Γ (**a**), K (**c**) and K′ (**e**) points with H-polarized pump. **b**,**d**,**f**, Corresponding results for a V-polarized pump. The energies used for excitation of the Γ and K/K′ points are 1.4547 eV and 1.4551 eV, respectively. The cross in each panel marks the position of the pump spot.

When the excitation angle is changed to excite the K′ point instead (Fig. 3e), the pattern is reversed, as expected, because the sign of the Dresselhaus-type field is opposite. Our results are in strong qualitative agreement with theoretical spin patterns calculated using the gauge-field Hamiltonian (Supplementary Section 1) as well as the numerical simulations of ref. [4]. In Fig. 3b,d,f we demonstrate that, upon changing to V-polarized excitation, the patterns shown in Fig. 3a,c,e are all reversed because the initial pseudospin vector points in the opposite direction[28], which confirms that the observed spin patterns result from precession of the pseudospin vector in the OSHE regime.

Now we turn our attention to the p bands. Using the same procedure as that of Fig. 2, we determine the texture of the effective magnetic field across momentum space at the energy of the Dirac points to reveal the local symmetry surrounding the K and K′ points. The full momentum space linear polarization map (Supplementary Section 5) confirms that the local symmetry around these points has the form of Dresselhaus SOC (with opposite sign for K and K′), as is the case for the s bands. We show the field surrounding a K point in Fig. 4a, where a clear single winding of the Dresselhaus type is visible. Note that the sign of the field for a given valley (K or K′) is opposite to the case of the s bands (as seen also in Fig. 1). Our finding is supported by the TB model developed for the p orbitals[26], where the calculated field texture shows excellent agreement (Fig. 4b). To further confirm the Dresselhaus-type fields, we performed OSHE measurements by coherently exciting the p bands. In Fig. 4c–f we show results for resonant excitation of the K and K′ points at $k_y/(2\pi/3\sqrt{3}a) = \pm 2$ (Fig. 4c,e respectively). Clear two-fold circular polarization patterns can be seen, which rotate when the excitation polarization is changed from H to V (Fig. 4d,f). These findings are in good agreement with theoretical calculations (Supplementary Section 1).

In summary, we have experimentally demonstrated the existence of local Dresselhaus-type fields surrounding the Dirac points in photonic graphene, confirmed by the generation of two-fold circular polarization patterns in the OSHE. Our findings constitute the realization of a synthetic SU(2) non-Abelian gauge field induced by the presence of the honeycomb periodic potential, which leads to a TE–TM effective magnetic field with a modified texture at specific points in momentum space. We note that although such fields may be engineered in other lattices featuring Dirac cones, such as Kagome lattices[30], it is not possible in other geometries such as Lieb lattices due to the square symmetry. Practically speaking, our findings offer a means of separating and routing spins, where the single-winding effective magnetic field (odd in k) analogous to electronic systems is highly advantageous because it leads to counter-propagation of opposite spins. Further fundamental consequences of the non-Abelian gauge field on the motion of wavepackets may be studied using the zitterbewegung effect (Supplementary Section 3). This field is also responsible for the emergence of topologically nontrivial

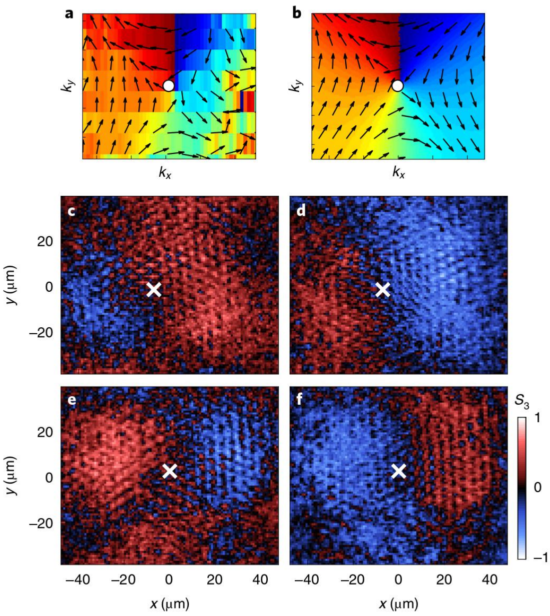

Fig. 4 | Effective magnetic field texture and OSHE for *p* bands. **a**, Experimentally obtained effective magnetic field texture surrounding a K point. **b**, Corresponding calculated effective magnetic field texture surrounding a K point. **c**,**e**, Measured real-space circular polarization degree S_3 under resonant excitation at the K (**c**) and K′ (**e**) points with an H-polarized pump. **d**,**f**, Corresponding results for a V-polarized pump. The energy used for excitation is 1.4582 eV. The crosses in **c**–**f** mark the position of the pump spot.

gaps in the polariton spectrum in the presence of external magnetic fields breaking time-reversal symmetry (which is not broken in our system)[31,32]. In microcavities with a small exciton–photon detuning, the addition of spin-anisotropic polariton–polariton interactions to the present system opens up new possibilities, including spin-dependent Klein tunnelling[20], interaction-induced topological phase transitions[33] and potentially a nonlinear modification of the spin domains[34]. We also anticipate that, in principle, the gauge field realized in our system may be engineered in other platforms such as photonic crystals based on thick slab waveguides with small TE–TM splitting[35] or plasmonic lattices[36]. The study of the non-Abelian gauge fields acting on photon spin in topological lattices with special symmetries would also be an interesting research direction[37].

Online content

Any methods, additional references, Nature Research reporting summaries, source data, extended data, supplementary information, acknowledgements, peer review information; details of author contributions and competing interests; and statements of data and code availability are available at https://doi.org/10.1038/s41566-020-00729-z.

Received: 26 February 2020; Accepted: 20 October 2020;
Published online: 30 November 2020

References

1. Qi, X.-L. & Zhang, S.-C. Topological insulators and superconductors. *Rev. Mod. Phys.* **83**, 1057–1110 (2011).
2. Chen, Y. et al. Non-Abelian gauge field optics. *Nat. Commun.* **10**, 3125 (2019).
3. Jacqmin, T. et al. Direct observation of Dirac cones and a flatband in a honeycomb lattice for polaritons. *Phys. Rev. Lett.* **112**, 116402 (2014).
4. Nalitov, A. V., Malpuech, G., Terças, H. & Solnyshkov, D. D. Spin–orbit coupling and the optical spin Hall effect in photonic graphene. *Phys. Rev. Lett.* **114**, 026803 (2015).
5. Yang, C. N. & Mills, R. L. Conservation of isotopic spin and isotopic gauge invariance. *Phys. Rev.* **96**, 191–195 (1954).
6. Wilczek, F. & Zee, A. Appearance of gauge structure in simple dynamical systems. *Phys. Rev. Lett.* **52**, 2111–2114 (1984).
7. Fröhlich, J. & Studer, U. M. Gauge invariance and current algebra in nonrelativistic many-body theory. *Rev. Mod. Phys.* **65**, 733–802 (1993).
8. Jin, P.-Q., Li, Y.-Q. & Zhang, F.-C. SU(2)×U(1) unified theory for charge, orbit and spin currents. *J. Phys. A* **39**, 7115–7123 (2006).
9. Sinova, J., Valenzuela, S. O., Wunderlich, J., Back, C. H. & Jungwirth, T. Spin Hall effects. *Rev. Mod. Phys.* **87**, 1213–1260 (2015).
10. Ohno, H., Stiles, M. D. & Dieny, B. Spintronics. *Proc. IEEE. Inst. Electr. Electron. Eng.* **104**, 1782–1786 (2016).
11. Aidelsburger, M., Nascimbene, S. & Goldman, N. Artificial gauge fields in materials and engineered systems. *Comptes Rendus Phys.* **19**, 394–432 (2018).
12. Shelykh, I. A., Kavokin, A. V. & Malpuech, G. in *Spin Dynamics of Exciton Polaritons in Microcavities* Ch. 9, 187–210 (Wiley, 2007).
13. Rechtsman, M. C. et al. Strain-induced pseudomagnetic field and photonic Landau levels in dielectric structures. *Nat. Photon.* **7**, 153–158 (2013).
14. Liu, F., Xu, T., Wang, S., Hang, Z. H. & Li, J. Polarization beam splitting with gauge field metamaterials. *Adv. Opt. Mater.* **7**, 1801582 (2019).
15. Hafezi, M., Mittal, S., Fan, J., Migdall, A. & Taylor, J. M. Imaging topological edge states in silicon photonics. *Nat. Photon.* **7**, 1001–1005 (2013).
16. Mittal, S. et al. Topologically robust transport of photons in a synthetic gauge field. *Phys. Rev. Lett.* **113**, 087403 (2014).
17. Rechcińska, K. et al. Engineering spin–orbit synthetic Hamiltonians in liquid–crystal optical cavities. *Science* **366**, 727–730 (2019).
18. Gianfrate, A. et al. Measurement of the quantum geometric tensor and of the anomalous Hall drift. *Nature* **578**, 381–385 (2020).
19. Fieramosca, A. et al. Chromodynamics of photons in an artificial non-Abelian magnetic Yang–Mills field. Preprint at https://arxiv.org/abs/1912.09684 (2019).
20. Solnyshkov, D., Nalitov, A., Teklu, B., Franck, L. & Malpuech, G. Spin-dependent Klein tunneling in polariton graphene with photonic spin–orbit interaction. *Phys. Rev. B* **93**, 085404 (2016).
21. Milićević, M. et al. Edge states in polariton honeycomb lattices. *2D Mater.* **2**, 034012 (2015).
22. Milićević, M. et al. Type-III and tilted Dirac cones emerging from flat bands in photonic orbital graphene. *Phys. Rev. X* **9**, 031010 (2019).
23. Sala, V. G. et al. Spin–orbit coupling for photons and polaritons in microstructures. *Phys. Rev. X* **5**, 011034 (2015).
24. Whittaker, C. E. et al. Exciton polaritons in a two-dimensional Lieb lattice with spin–orbit coupling. *Phys. Rev. Lett.* **120**, 097401 (2018).
25. Yang, Y. et al. Synthesis and observation of non-Abelian gauge fields in real space. *Science* **365**, 1021–1025 (2019).
26. Zhang, C., Wang, Y. & Zhang, W. Topological phase transition with *p* orbitals in the exciton–polariton honeycomb lattice. *J. Phys. Condens. Matter* **31**, 335403 (2019).
27. Dresselhaus, G. Spin–orbit coupling effects in zinc blende structures. *Phys. Rev.* **100**, 580–586 (1955).
28. Kavokin, A., Malpuech, G. & Glazov, M. Optical spin Hall effect. *Phys. Rev. Lett.* **95**, 136601 (2005).
29. Leyder, C. et al. Observation of the optical spin Hall effect. *Nat. Phys.* **3**, 628–631 (2007).
30. Gulevich, D. R., Yudin, D., Iorsh, I. V. & Shelykh, I. A. Kagome lattice from an exciton–polariton perspective. *Phys. Rev. B* **94**, 115437 (2016).
31. Nalitov, A. V., Solnyshkov, D. D. & Malpuech, G. Polariton ℤ topological insulator. *Phys. Rev. Lett.* **114**, 116401 (2015).
32. Klembt, S. et al. Exciton–polariton topological insulator. *Nature* **562**, 552–556 (2018).
33. Bleu, O., Solnyshkov, D. D. & Malpuech, G. Interacting quantum fluid in a polariton Chern insulator. *Phys. Rev. B* **93**, 085438 (2016).
34. Flayac, H., Solnyshkov, D. D., Shelykh, I. A. & Malpuech, G. Transmutation of skyrmions to half-solitons driven by the nonlinear optical spin Hall effect. *Phys. Rev. Lett.* **110**, 016404 (2013).
35. Shapochkin, P. Y. et al. Polarization-resolved strong light-matter coupling in planar GaAs/AlGaAs waveguides. *Opt. Lett.* **43**, 4526–4529 (2018).
36. Bliokh, K. Y., Rodríguez-Fortuño, F. J., Nori, F. & Zayats, A. V. Spin–orbit interactions of light. *Nat. Photon.* **9**, 796–808 (2015).
37. Khanikaev, A. B. & Shvets, G. Two-dimensional topological photonics. *Nat. Photon.* **11**, 763–773 (2017).

Methods

Sample description. Our sample is a GaAs microcavity with 23 (26) top (bottom) GaAs/$Al_{0.85}Ga_{0.15}As$ distributed Bragg reflector pairs and six $In_{0.04}Ga_{0.96}As$ quantum wells, as previously described in ref. [38]. The sample was processed using electron-beam lithography and plasma dry etching to pattern arrays of micropillars with 3-µm diameters and an etch depth on the order of 8 µm. We studied a honeycomb lattice with a pillar-to-pillar separation of 2.8 µm and dimensions of ~$120\times100\,\mu m^2$. The cavity–exciton detuning was approximately −23 meV. The Q factor of the structure was determined to be ~16,000 from the linewidth of 0.09 meV. The size of the TE–TM splitting was ~0.12 meV at $k=1\,\mu m^{-1}$.

Excitation scheme. To characterize the dispersion relation of the honeycomb lattice, a low-power non-resonant diode laser was used in reflection geometry to incoherently populate all of the lattice modes. To study the formation of pseudospin domains, we excited the lattice in transmission geometry with a continuous-wave Ti:sapphire laser tuned to be resonant with the honeycomb lattice dispersion. Different states can be excited by varying the energy and angle of incidence θ of the Gaussian laser beam, the latter of which is changed using a translation stage to move the lateral position of the beam before the excitation objective. This allowed us to accurately control the in-plane wavevector of the injected wavepacket because $k=\left(\frac{\omega}{c}\right)\sin\theta$, where ω is the laser frequency. The linear polarization of the injected wavepacket can also be controlled through the use of a linear polarizer and half wave plate in the excitation path. The excitation beam has a full-width at half-maximum of ~15 µm.

Detection scheme. To characterize the pseudospin texture around the Γ, K and K′ points, we measured the polariton PL emission under non-resonant excitation (in the low-density regime far below the condensation threshold) by employing a half wave plate and linear polarizer in the detection path to measure the first two Stokes parameters. These are given by $S_1=(I_H-I_V)/(I_H+I_V)$ and $S_2=(I_D-I_A)/(I_D+I_A)$, where I_H, I_V, I_D and I_A give the intensity of emitted light in the horizontal, vertical, diagonal and anti-diagonal polarizations, respectively. By scanning the final lens across the spectrometer slit, multiple E versus k slices were recorded (corresponding to different wavevectors in the direction orthogonal to the spectrometer slit), allowing 2D energy-resolved polarization maps to be constructed. Each map shows a small spectral window of ~20 µeV around the energy of the Γ or Dirac points. Because polariton modes have finite linewidth, there is non-zero PL intensity at k vectors away from these points (for example, $|k-K|>0$). This PL emission arises from the tail of polariton modes with maxima at energies tens or hundreds of µeV above (or below) the specific energy of interest due to polariton dispersion. The lower intensity of the tails leads to decreased signal-to-noise ratio for further away k vectors, as seen in Figs. 2 and 4.

For the resonant transmission measurements the half wave plate was replaced by a quarter wave plate to measure the third Stokes parameter, which is given by $S_3=(I_{\sigma^+}-I_{\sigma^-})/(I_{\sigma^+}+I_{\sigma^-})$, where I_{σ^+} and I_{σ^-} correspond to the emission intensity in the right and left circular polarizations, respectively.

Gauge field representation. The pseudospin patterns in Fig. 2 correspond to the eigenstates of the polariton graphene effective Hamiltonian, which has the following form in the vicinity of the Dirac points[4]:

$$H^{D}(\mathbf{q})=\hbar v_F\left(\tau_z q_x\sigma_x+q_y\sigma_y\right)+\Delta\left(\tau_z\sigma_y\otimes s_y-\sigma_x\otimes s_x\right)\qquad(1)$$

where $\mathbf{q}$ is the wavevector deviation from the corresponding Dirac point set by the valley index $\tau_z=\pm1$, v_F is the effective Fermi velocity, σ and s are the sublattice and polarization pseudospin operators, and Δ is the effective photonic SOC strength[23]. Prefactors of both terms in Hamiltonian (1) may be expressed in the TB model parameters: $\hbar v_F=3Ja/2$, $\Delta=3\delta J/2$ (see next section in Methods for additional details). The spin–orbit term may be included in the low-energy graphene Hamiltonian, represented by the first term in equation (1), with minimal coupling transformation $\mathbf{q}\rightarrow\mathbf{q}-\mathbf{A}$ with the gauge field components given by

$$A_x=-\frac{\Delta}{\hbar v_F}\tau_z s_x,\;\; A_y=\frac{\Delta}{\hbar v_F}\tau_z s_y\qquad(2)$$

The artificial gauge field (2) is non-Abelian because the components do not commute[20]. This field is responsible for the suppression of Klein tunnelling[20] and emergence of topologically nontrivial bandgaps of the polariton spectrum in the presence of external magnetic fields[31,32]. Polarization spectral splitting may be also attributed to the effective magnetic field, acting on polariton pseudospin. In the range of energies $\Delta\ll|E|\ll\hbar v_F/a$ this effective SOC is given by the Hamiltonian term $H^{D}_{SOC}(\mathbf{q})=\pm\Delta\left(q_x s_x-q_y s_y\right)/q$, sharing the same angular dependence with the Dresselhaus spin–orbit term in electron systems[27], but constant in the wavevector absolute value q. Note that the sign of the splitting inverts with both valley index τ_z and the sign corresponding to upper and lower Dirac cones.

The Hamiltonian (1) close to Dirac points thus drastically differs from its counterpart in the vicinity of the Γ point

$$H^{\Gamma}(\mathbf{k})=\hbar^2k^2/(2m)+\beta\left[s_x(k_x^2-k_y^2)+2s_yk_xk_y\right]\qquad(3)$$

where the first term corresponds to a free particle with effective mass $m=\hbar^2/(3Ja^2)$ and the second term describes the action of TE–TM splitting, corresponding to the effective magnetic field with components $\Omega_x=\beta a^2(k_x^2-k_y^2)$ and $\Omega_y=2\beta k_xk_y$ with $\beta=3\delta Ja^2/8$, related to the TB model parameters (see next section in Methods for details). Note that the quadratic dependence of the effective magnetic field on the components of $\mathbf{k}$, fully similar to those reported for the case of an unpatterned cavity, precludes its description in terms of the minimal coupling to a synthetic gauge field and leads to the difference of the effective masses of the longitudinal and transverse polariton modes, $m_{l,t}=m(1\pm2m\beta/\hbar^2)$[39].

Effective field derivation near the Dirac point. The effective magnetic field acting on the polariton pseudospin near the Dirac point is obtained by development of the TB Hamiltonian[4]:

$$H_{\mathbf{k}}=-J\sigma_+-\delta J\sigma_+\otimes\left(f_{\mathbf{k}}^{+}s_++f_{\mathbf{k}}^{-}s_-\right)+\text{h.c.}\qquad(4)$$

Although the local gauge fields in the vicinities of Dirac points K and K′ were studied in ref. [4], the effective field given by formula (3) near the Γ point, reproducing the symmetry and quadratic k dependence of the TE–TM field in planar microcavities, is also inherent to Hamiltonian (4). In the latter case, the splitting is due to the second-order terms in the complex coefficients:

$$f_{\mathbf{k}}=3\left(1-\frac{k^2a^2}{4}\right),\; f_{\mathbf{k}}^{\pm}=-\frac{3i}{2}k_\pm a-\frac{3}{8}k_\pm^2a^2\qquad(5)$$

where $k_\pm=k_x\pm ik_y$. The energy dispersion near the ground state in the corresponding order then reads

$$E_k^{\pm}=-3J\left[1-\frac{k^2a^2}{8}\left(1-\frac{\delta J^2}{J^2}\pm\frac{\delta J}{J}\right)\right]\qquad(6)$$

and the Hamiltonian has the form of interaction with the effective TE–TM field (3) of strength given by $\beta=3\delta Ja^2/8$.

TB parameters used to fit experimental data. To fit the experimental dispersion relations in Fig. 1, for the s bands we use $J=0.12$ meV and $\delta J=0.018$ meV. To account for a small asymmetry of the dispersion about the Dirac energy (visible at the Γ point), we add a next-nearest-neighbour correction of −0.008 meV (ref. [3]). For the p bands we used the TB model of ref. [26] with $J=-0.6$ meV and $\delta J=0.05$ meV, which describes tunnelling of p orbitals with lobes oriented along the link connecting micropillars. In our notation J and δJ corresponds to t and Δt in ref. [26].

Data availability

The data that support the findings of this study are openly available from the University of Sheffield repository at https://doi.org/10.15131/shef.data.13060610.

References

38. Whittaker, C. E. et al. Effect of photonic spin–orbit coupling on the topological edge modes of a Su–Schrieffer–Heeger chain. *Phys. Rev. B* **99**, 081402 (2019).
39. Shelykh, I. A., Nalitov, A. V. & Iorsh, I. V. Optical analog of Rashba spin–orbit interaction in asymmetric polariton waveguides. *Phys. Rev. B* **98**, 155428 (2018).

Acknowledgements

The work was supported by UK EPSRC grants nos. EP/N031776/1 and EP/R04385X/1 and by the Russian Science Foundation (project no. 19-72-20120). I.A.S. acknowledges support from the Icelandic Science Foundation, project 'Hybrid Polaritonics'. A.V.N. acknowledges support from the European Union's Horizon 2020 research and innovation programme under the Marie Skłodowska-Curie grant agreement no. 846353.

Author contributions

C.E.W. and T.D. performed the experiments and analysed the data. E.C. grew the sample. B.R. performed post-growth fabrication. A.V.N. and I.A.S. provided theoretical input. C.E.W., A.V.N. and A.V.Y. performed theory calculations. C.E.W. and D.N.K. designed the experiment. C.E.W., A.V.N., I.A.S., M.S.S. and D.N.K. wrote the manuscript.

Competing interests

The authors declare no competing interests.

Additional information

Supplementary information is available for this paper at https://doi.org/10.1038/s41566-020-00729-z.

Correspondence and requests for materials should be addressed to C.E.W. or D.N.K.

Peer review information *Nature Photonics* thanks Yi Yang and the other, anonymous, reviewer(s) for their contribution to the peer review of this work.

Reprints and permissions information is available at www.nature.com/reprints.

natureresearch https://doi.org/10.1038/s41566-020-00729-z

Supplementary information

Optical analogue of Dresselhaus spin–orbit interaction in photonic graphene

In the format provided by the
authors and unedited

Supplementary material for "Optical analogue of Dresselhaus spin-orbit interaction in photonic graphene"

C. E. Whittaker,[1] T. Dowling,[1] A. V. Nalitov,[2, 3, 4] A. V. Yulin,[4] B. Royall,[1]
E. Clarke,[5] M. S. Skolnick,[1, 4] I. A. Shelykh,[3, 4] and D. N. Krizhanovskii[1, 4]
[1]Department of Physics and Astronomy, University of Sheffield, Sheffield S3 7RH, United Kingdom
[2]Faculty of Science and Engineering, University of Wolverhampton,
Wulfruna Street, Wolverhampton WV1 1LY, UK
[3]Science Institute, University of Iceland, Dunhagi-3, IS-107 Reykjavik, Iceland
[4]ITMO University, St. Petersburg 197101, Russia
[5]EPSRC National Epitaxy Facility, University of Sheffield, Sheffield S1 3JD, United Kingdom

Contents

I. CALCULATED SPIN PATTERNS

The spin patterns observed in the experiment are determined by the Dresselhaus-type structure of the part of the Hamiltonian describing TE-TM splitting in the system. Before presenting the results of full numerical analysis, let us show this explicitly.

The 4x4 Hamiltonian (1) of the main text of the article can be represented in the following block form, with 2x2 non zero blocks standing off diagonal:

$$H^D = \begin{pmatrix} 0 & \hbar v_F \tau_z q_x - \Delta s_x - i(\hbar v_F q_y + \Delta \tau_z s_y) \\ \hbar v_F \tau_z q_x - \Delta s_x - i(\hbar v_F q_y + \Delta \tau_z s_y) & 0 \end{pmatrix}. \tag{S1}$$

By use of the unitary transformation, corresponding to the diagonalization in sublattice pseudospin, but not in the polarization space, i.e. going to the representation of upper and lower Dirac cones, one can transform this Hamiltonian into block diagonal form:

$$H^D = \begin{pmatrix} +H^{(2)} & 0 \\ 0 & -H^{(2)} \end{pmatrix} \tag{S2}$$

where the upper block corresponds to a pair of upper Dirac cones with two orthogonal polarizations, and the lower block to a pair of lower Dirac cones, and 2x2 blocks $H^{(2)}$ are:

$$H^{(2)} = \sqrt{\hbar^2 v_F^2 q^2 + 2\hbar v_F \tau_z \Delta (q_y s_y - q_x s_x) + 2\Delta^2 (1 - s_z)}. \tag{S3}$$

In the limit $\hbar v_F q \gg \Delta$, corresponding to the asymptotically linear dispersion branches, one can use Taylor decomposition in the above equation to obtain:

$$H^{(2)} = \hbar v_F q + \tau_z \Delta \frac{q_y s_y - q_x s_x}{q} \tag{S4}$$

The two terms in the above representation may be interpreted as the standard linear Dirac part $\hbar v_F q$, supplemented with the effective spin-orbit coupling term $\pm\Delta(q_y s_y - q_x s_x)/q$, where the $\pm$ sign is defined by the product of the valley index τ_z and the index of the Dirac cone (plus for upper, minus for lower cone). This effective spin-orbit coupling fully reproduces the angular dependence of the Dresselhaus Hamiltonian for 2D electron systems, while being independent on the momentum absolute value q, in contrast to the linear momentum dependence of the Dresselhaus term.

Now, let us describe the procedure which can be used to numerically reproduce the spin patterns generated in the optical spin Hall effect (OSHE). In the case of quasi-resonant pumping of the Dirac points the polariton wavefunction obeys the generalized Schrödinger equation:

$$i\hbar\dot{\Psi} = \left[H^D - i\hbar\Gamma\right]\Psi + P_0 e^{-q^2L^2/4} e^{-i\omega t}, \tag{S5}$$

where H^D is the effective Hamiltonian close to the Dirac points (see Eq. (1) in Methods section of main text) and Γ is the polariton linewidth. The second term on the right hand side describes in-phase excitation of both sublattices by a pump of size L with energy ω and amplitude and polarization given by P_0. $P_0 = (1,1,1,1)^T$ for horizontal polarization and $P_0 = (1,-1,1,-1)^T$ for vertical polarization. q is the wave vector deviation from the Dirac point. The stationary solution then reads

$$\Psi_0 = P_0 e^{-q^2L^2/4}\left[\hbar(\omega + i\Gamma) - H^D\right]^{-1}. \tag{S6}$$

The corresponding real space wavefunction, which is what we observe in experiment, is then obtained using an inverse Fourier transform. In Figs. S1 and S2 we plot the calculated real space spin distribution corresponding to the excitation conditions of Figs. 3 and 4 of the main text.

We note that the same procedure can be used for H^Γ (i.e. excitation near the Γ point) to produce four-fold spin patterns as observed in the conventional OSHE[1].

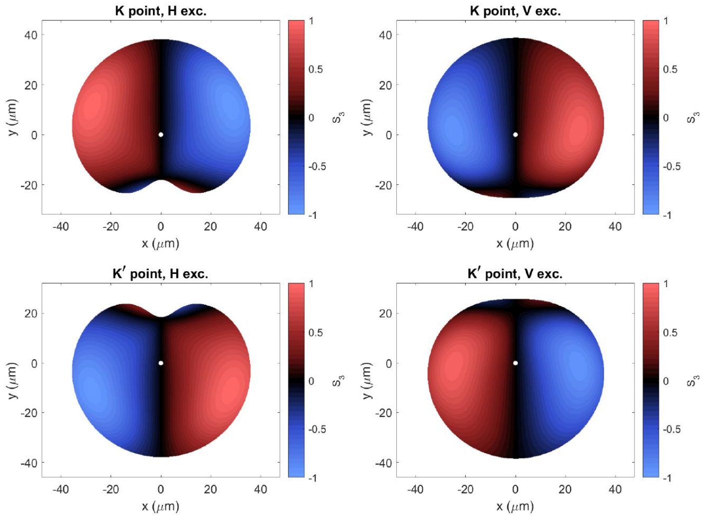

FIG. S1: Calculated spin patterns for quasi-resonant excitation of the s-band Dirac points. The following parameters, based on experimental values, are used: $J = 0.12$ meV, $\delta J = 0.018$ meV, $\omega = 0.03$ meV, $\Gamma = 0.04$ meV and $L = 15$ μm. The images are cropped where the intensity drops to 1% of the maximum value, which is the approximate noise level in experiment. The white marker shows the position of the excitation spot.

Note, that in the simulated real space spin patterns there are weak traces of a four-leaf pattern visible in the peripheral area where the field intensity drops down to 1% of the peak maxima (weakly visible in the experimental Fig. 3 also). Generally, the spin patterns in the OSHE can be viewed as the interference between polariton modes

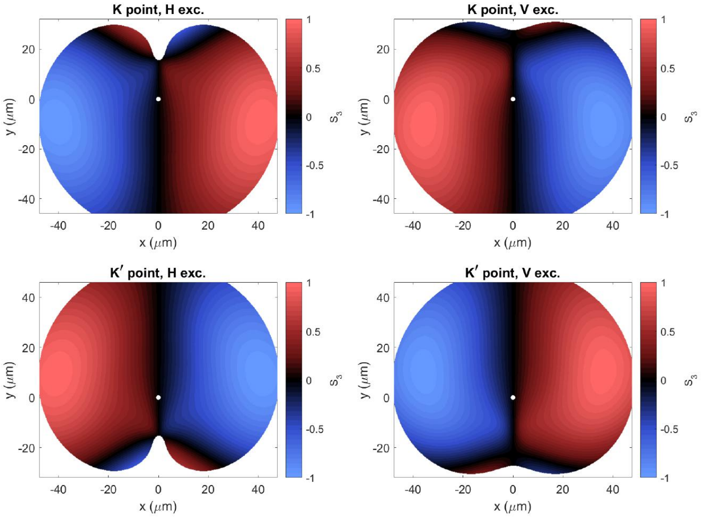

FIG. S2: Calculated spin patterns for quasi-resonant excitation of the p-band Dirac points. The tunnelling energies are based on experimental parameters corresponding to $J = -0.6$ meV, $\delta J = 0.05$ meV, with additional parameters $\omega = 0.03$ meV, $\Gamma = 0.06$ meV and $L = 15$ μm. The images are cropped where the intensity drops to 1% of the maximum value, which is the approximate noise level in experiment. The white marker shows the position of the excitation spot.

of different linear polarization, which are resonantly excited at various k-vectors by the CW pump focused into a finite spot. In a realistic scenario not all modes are excited equally however, since the excitation efficiency at a particular k close to the Dirac point depends on a combination of the pump frequency, polariton linewidth (losses Γ), pump polarization and valley index. Slightly different weights of the resonantly excited interfering polariton branches can make the interference pattern more complicated than an ideal two-leaf structure. In simulations the purity of the two-leaf structure can be increased significantly by the appropriate adjustment of the excitation parameters, for example, by increase in polariton losses or the frequency of the pump. A detailed analysis of this effect is beyond the scope of the present manuscript.

II. CANONICAL INTRODUCTION OF SU(2) GAUGE FIELD FOR POLARITON GRAPHENE

Gauge fields appear in the Standard Model of elementary particle interactions via canonical substitution

$$\partial_\mu \rightarrow D_\mu = \partial_\mu - iA_\mu, \tag{S7}$$

A_μ can be simple scalar functions of the coordinates in the Minkowsky space, or square matrices of the dimensionality 2 or 3. In the former case one deals with Abelian gauge fields, and in the latter with non-Abelian, or Yang-Mills, gauge fields, for which $[A_\mu; A_\nu] \neq 0$. The necessity of the introduction of the substitution S7 is dictated by the demand to keep the field Lagrangian invariant under the certain class of the transformations, known as gauge transformations.

In non-relativistic quantum mechanics and condensed matter physics synthetic gauge fields can be introduced in the similar way, by imposing the condition of the gauge invariance of the non-relativistic Hamiltonian density of the considered system. Let us show explicitly, how this allows to introduce the SU(2) gauge field for the considered case of the polariton graphene.

Let us start from the case, when TE-TM splitting of the photonic mode can be neglected. The dispersion of the hexagonally patterned microcavity in this case around K and K' points of the Brillouin zone consists of the degenerated pair of the Dirac cones, corresponding to the two orthogonal polarizations. Introducing the wavefunction of a spinor polariton as $\Psi^T = (\Psi_+, \Psi_-)^T$, where ± signs correspond to polarization degree of freedom, one can write the Hamiltonian density as:

$$\mathcal{H} = \Psi^\dagger \hat{H}_0 \Psi = -i\hbar v_F (\psi_+^*, \psi_-^*) \begin{pmatrix} \tau_z \sigma_x \partial_x + \sigma_y \partial_y & 0 \\ 0 & \tau_z \sigma_x \partial_x + \sigma_y \partial_y \end{pmatrix} \begin{pmatrix} \psi_+ \\ \psi_- \end{pmatrix}. \tag{S8}$$

Note, that as components of the orthogonal polarizations correspond to the individual Dirac dispersions, the functions $\psi_\pm$ are themselves 2-spinors in the pseudospin space corresponding to the upper and lower Dirac cones, where the Pauli operators $\sigma_{x,y}$ act.

This Hamiltonian is invariant under the *global* SU(2) transformation of the type

$$\tilde{\psi} = \omega\psi, \tag{S9}$$

where constant matrix $\hat{\omega}$ belongs to the SU(2) Lie group. This transformation is nothing more but standard rotation in the polarization space. Note, however, that Hamiltonian density S8 is *not* invariant under *local* SU(2) gauge transformation, when the components of the matrix $\hat{\omega} = \hat{\omega}(\mathbf{r})$ depend on the coordinates, as in this case

$$\tilde{\mathcal{H}} = \tilde{\Psi}^\dagger \hat{H}_0 \tilde{\Psi} = \mathcal{H} - i\hbar v_F (\psi_+^*, \psi_-^*) \left(\tau_z\sigma_x \otimes \partial_x\hat{\omega} + \sigma_y \otimes \partial_y\hat{\omega}\right) \begin{pmatrix} \psi_+ \\ \psi_- \end{pmatrix} \neq \mathcal{H} \tag{S10}$$

where the sign of direct product $\otimes$ indicates that Pauli matrices $\sigma_{x,y}$ and transformation matrix $\hat{\omega}$ act in different spaces (pseudospin space corresponding to upper and lower Dirac cones and polarization space, respectively). We can, however, restore the invariance, if we make the canonical replacement, performing the substitution S7, where $\mu = x, y$, and 2×2 matrices $i\hat{A}_\mu$ belong to the Lie algebra of SU(2) group (i.e. matrices $A_{x,y}$ themselves are Hermitian) and obey the following gauge transformation:

$$\tilde{\hat{A}}_\mu = \hat{\omega}\hat{A}_\mu\hat{\omega}^{-1} - i\hat{\omega}\partial_\mu\hat{\omega}^{-1}. \tag{S11}$$

The total SU(2) gauge invariant Hamiltonian then reads:

$$\hat{H} = \hbar v_F \left[\tau_z\sigma_x \otimes \left(\hat{q}_x - \hat{A}_x\right) + \sigma_y \otimes \left(\hat{q}_y - \hat{A}_y\right)\right]. \tag{S12}$$

The details of the components of SU(2) gauge potential depend on the choice of the polarization basis, which corresponds to the fixing of the gauge. In particular, in the basis of circular polarizations, the components $\hat{A}_{x,y}$ are given by equations (2) of the main text. Note, that they do not depend on the coordinates, and thus gauge transformation for them coincides with unitary transformation, as it follows from Eq. S11. The Hamiltonian S12 coincides with those given by equation 1 of the main text.

III. ZITTERBEWEGUNG IN POLARITON GRAPHENE

Although the components of the SU(2) gauge field given by equations 2 of the main text are coordinate independent, they have non-trivial impact on the dynamics of the system, including those, corresponding to the spatial variables. This is in striking contrast with the case of a constant Abelian U(1) potential, which can be straightforwardly gauged out by trivial phase transformation. This difference stems from the fact, that components of the field tensor for non-Abelian fields, defined as

$$\hat{F}_{\mu,\nu} = \partial_\mu\hat{A}_\nu - \partial_\nu\hat{A}_\mu + [\hat{A}_\mu; \hat{A}_\nu] \tag{S13}$$

are, due to the presence of the last term, vanishing for Abelian fields, non zero even if $\hat{A}_\mu = const.$

Let us see, how Dresselhaus-type terms affect the spatial dynamics of wavepackets in polariton graphene. We will use Heisenberg representation of the Hamiltonian (1) of the main text

$$\hat{H}^D(t) = \hbar v_F \left[\tau_z \hat{q}_x \hat{\sigma_x}(t) + \hat{q}_y \hat{\sigma_y}(t)\right] + \Delta \left[\tau_z \hat{\sigma_y}(t) \otimes \hat{s}_y(t) - \hat{\sigma}_x(t) \otimes \hat{s}_x(t)\right], \tag{S14}$$

where the operators $\hat{q}_{x,y}$ do not depend on time, as they commute with the Hamiltonian.

Let us consider a wavepacket described by some 4-spinor $\Psi(\mathbf{r})$. The time evolution of the operators of the coordinates is given by the following Heisenberg equations of motion:

$$\frac{d\hat{x}}{dt} = \frac{1}{i\hbar}\left[\hat{x}; \hat{H}^D\right] = v_F \tau_z \hat{\sigma}_x(t), \tag{S15}$$

$$\frac{d\hat{y}}{dt} = \frac{1}{i\hbar}\left[\hat{y}; \hat{H}^D\right] = v_F \hat{\sigma}_y(t), \tag{S16}$$

and the dynamics of the spin operators corresponding to pseudospin and polarization is given by:

$$\frac{d\hat{\sigma}_x}{dt} = \frac{1}{i\hbar}\left[\hat{\sigma}_x; \hat{H}^D\right] = 2v_F\hat{q}_y\hat{\sigma}_z(t) + \frac{2\Delta\tau_z}{\hbar}\hat{s}_y(t)\otimes\hat{\sigma}_z(t), \tag{S17}$$

$$\frac{d\hat{\sigma}_y}{dt} = \frac{1}{i\hbar}\left[\hat{\sigma}_y; \hat{H}^D\right] = -2v_F\tau_z\hat{q}_x\hat{\sigma}_z(t) + \frac{2\Delta}{\hbar}\hat{s}_x(t)\otimes\hat{\sigma}_z(t), \tag{S18}$$

$$\frac{d\hat{\sigma}_z}{dt} = \frac{1}{i\hbar}\left[\hat{\sigma}_z; \hat{H}^D\right] = 2v_F\left[\tau_z\hat{q}_x\hat{\sigma}_y(t) - \hat{q}_y\hat{\sigma}_x(t)\right] - \frac{2\Delta}{\hbar}\left[\tau_z\hat{s}_y(t)\otimes\hat{\sigma}_x(t) + \hat{s}_x(t)\otimes\hat{\sigma}_x(t)\right], \tag{S19}$$

$$\frac{d\hat{s}_x}{dt} = \frac{1}{i\hbar}\left[\hat{s}_x; \hat{H}^D\right] = \frac{2\Delta\tau_z}{\hbar}\hat{\sigma}_y(t)\otimes\hat{s}_z(t), \tag{S20}$$

$$\frac{d\hat{s}_y}{dt} = \frac{1}{i\hbar}\left[\hat{s}_y; \hat{H}^D\right] = \frac{2\Delta}{\hbar}\hat{\sigma}_x(t)\otimes\hat{s}_z(t), \tag{S21}$$

$$\frac{d\hat{s}_z}{dt} = \frac{1}{i\hbar}\left[\hat{\sigma}_z; \hat{H}^D\right] = -\frac{2\Delta}{\hbar}\left[\tau_z\hat{\sigma}_y(t)\otimes\hat{s}_x(t) + \hat{\sigma}_x(t)\otimes\hat{s}_y(t)\right]. \tag{S22}$$

Let us start our analysis from the simplest case $\Delta = 0$. In this regime, the closed set of the linear equations for $\hat{\sigma}_x(t), \hat{\sigma}_y(t), \hat{\sigma}_z(t)$ describes the precession of the pseudospin around an effective magnetic field $\vec{\Omega} = v_F(\tau_z\vec{e}_x + \vec{e}_y)$, and thus allows analytical solution:

$$\hat{\vec{\sigma}}(t) = e^{-i\hat{\Omega}t}\hat{\vec{\sigma}}(0), \tag{S23}$$

where $\hat{\vec{\sigma}}(t) = (\hat{\sigma}_x(t), \hat{\sigma}_y(t), \hat{\sigma}_y(t))^T$, and

$$\hat{\Omega} = 2v_F\begin{pmatrix} 0 & 0 & i\hat{q}_y \\ 0 & 0 & -i\tau_z\hat{q}_x \\ -i\hat{q}_y & i\tau_z\hat{q}_x & 0 \end{pmatrix}. \tag{S24}$$

Consider the particular case of the wavepacket localized around certain value of $\hat{q}_x \approx \langle q_x\rangle$, for which we can put approximately $\hat{q}_y \approx 0$. Choose the initial value of the pseudospin operator as: $\hat{\vec{\sigma}}(0) = (\hat{\sigma}_x(0), 0, \hat{\sigma}_z(0))^T$. Then, according to the equations S23, we get: $\hat{\sigma}_x(t) = \hat{\sigma}_x(0), \hat{\sigma}_y(t) = \hat{\sigma}_z(0)\sin(v_F\tau_z\hat{q}_xt)$, and mean values of x and y coordinated, describing the motion of the center of the wavepacket, can be found as:

$$x(t) = \langle\hat{x}(t)\rangle = x(0) + v_F\tau_z\langle\hat{\sigma}_x(0)\rangle t, \tag{S25}$$

$$y(t) = \langle\hat{y}(t)\rangle = y(0) + v_F\int_0^t\langle\hat{\sigma}_y(t')\rangle dt' = y(0) + v_F\int_0^t\langle\hat{\sigma}_z(0)\sin(v_F\tau_z\hat{q}_xt)\rangle dt' \approx \tag{S26}$$

$$\approx y(0) + \frac{\tau_z\langle\hat{\sigma}_z(0)\rangle}{\langle q_x\rangle}\left[1 - \sin(v_F\tau_z\langle q_x\rangle t)\right].$$

One sees, that the considered wavepacket is steadily displacing along x-axis, but undergoes periodic oscillations along y-axis, which correspond to the well known zitterbewegung effect for relativistic particles.

Now, let us return back to the case where Dresselhaus term is present and $\Delta \neq 0$. In this regime, the Hamiltonian S14 formally corresponds to those of the two interacting spins, placed into external magnetic field acting on only one of them. Clearly, in this case solution for pseudospin operators strongly differs from those, given by Eq. S23, which, according to Eqs. S15,S16 have strong effect on the orbital motion as well.

IV. FURTHER EXPERIMENTAL DETAILS

Here we present further details of the sample and experimental setup. The honeycomb lattice was fabricated from a planar semiconductor microcavity, which was grown on a double-side polished substrate to allow operation in transmission geometry. The sample was patterned to form arrays of overlapping micropillars by etching through the top and bottom DBR stacks (Fig. S3).

The sample was mounted in a continuous-flow cryostat and held at low temperature (< 10 K) for all measurements. For the momentum space images, nonresonant excitation provided by a 637 nm laser was used in a reflection geometry (Fig. S4a). The energy-resolved emission was detected with a 0.75 m spectrometer (1200 gr/mm) and Peltier cooled CCD and recorded in sections by translating the imaging lens. For the real space images, resonant excitation provided by a Ti:sapphire laser was used in a transmission geometry (Fig. S4b). For these measurements the spectrometer grating was set to zero order and the slit opened.

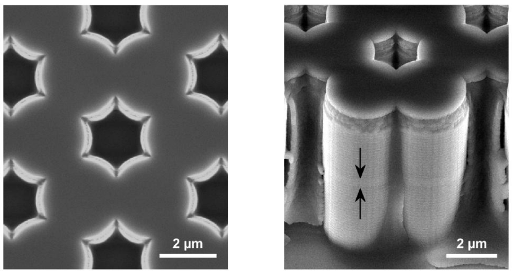

FIG. S3: Left, Overhead view of a honeycomb lattice. Right, Side view showing the top/bottom DBR stacks and cavity layer (shown by black arrows).

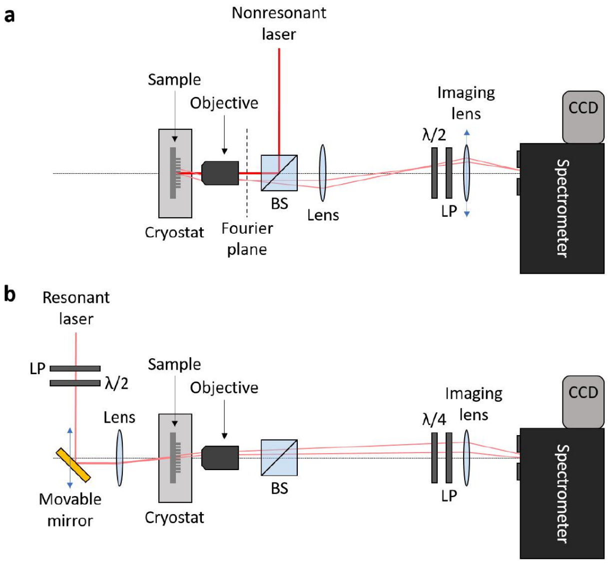

FIG. S4: Schematic diagrams of the reflection (a) and transmission (b) setups.

V. EXPERIMENTAL DETERMINATION OF EFFECTIVE MAGNETIC FIELD TEXTURES

In order to extract the effective magnetic field textures in momentum space, we resolve the emission in horizontal (H), diagonal (D), vertical (V) and anti-diagonal (A) polarizations corresponding to detection angles of 0°, 45°, 90° and 135° respectively. The detection angle, which we denote as α, is defined with respect to the x axis, shown along with the real space orientation of the honeycomb lattice in Fig. S5. Tomographic measurements in the H-V and D-A bases allow us to construct the Stokes parameters $S_1 = (I_H - I_V)/(I_H + I_V)$ and $S_2 = (I_D - I_A)/(I_D + I_A)$ respectively, allowing a complete characterization of the linear polarization state of the emission across momentum space. This is sufficient to determine the effective magnetic field texture since it is entirely in-plane (it has no circular component) in the absence of a real Zeeman field.

In Fig. S6 we show the polarization-resolved momentum space emission in the s bands (corresponding to Fig. 2 of the main text), at the energy of the Γ point at 1.4547 eV (a–d) and the Dirac points at 1.4551 eV (e–h). The total intensity S_0 reveals emission from the centre of the Brillouin zone (BZ) at $k = 0$ in the former case and from the six corners of the BZ forming a hexagon in the latter case. Replicas in the second BZs can also be seen. The

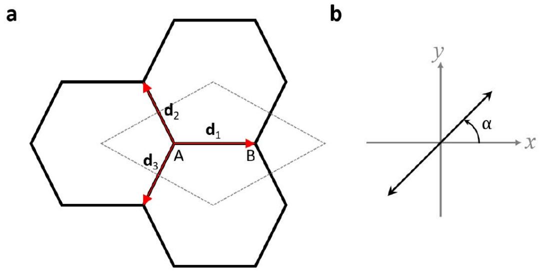

FIG. S5: (a) Real space orientation of the honeycomb lattice, labelled with A and B sublattices and nearest neighbour vectors $\mathbf{d}_1$, $\mathbf{d}_2$ and $\mathbf{d}_3$. The dashed diamond delimits a unit cell. (b) Definition of linear polarization detection angle α.

S_1 and S_2 maps shown allow the linear polarization angle ϕ of the emission to be calculated at each point using $2\phi = \arctan(S_2/S_1)$. Note the factor of two which represents the fact that one only has to rotate a polarization by 180° in real space to return to the same polarization, whilst the Stokes vector has undergone a full 360° rotation.

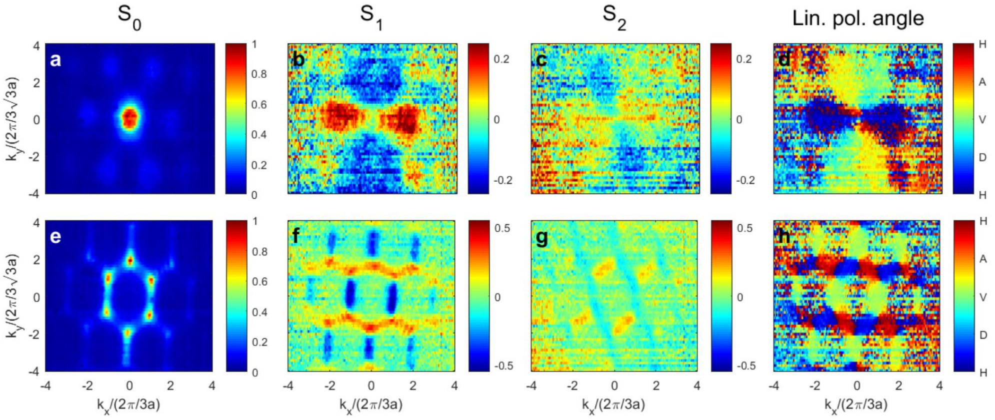

FIG. S6: (a–d) Tomographic images of the momentum space emission at the energy of the Γ point, showing the Stokes parameters S_0 (a), S_1 (b) and S_2 (c), along with the linear polarization angle ϕ (d). (e–h) Tomographic images of the momentum space emission at the energy of the Dirac points, showing the Stokes parameters S_0 (e), S_1 (f) and S_2 (g), along with the linear polarization angle ϕ (h).

In Fig. S7 we show the corresponding momentum space maps for the energy of the Dirac points in the p bands. Since the photoluminescence (PL) intensity is much weaker in the p bands, as can be seen in Fig. S8, the emission is integrated over a small spectral window of ~ 0.2 meV between 1.4581 eV and 1.4583 eV to increase the signal. From the total intensity S_0 we note that the emission pattern is the same as for the energy of the Dirac points in the s bands, with the difference that the brightest points are no longer found at the corners of the first BZ but at the outer corners of the second BZs. This reflects the larger leakage emission intensity (probably of escaping the cavity) for higher k vectors at higher energy. The rectangle in each panel corresponds to the K point for which the linear polarization angle is shown in Fig. 4 of the main text, which is taken from the second BZ due to the higher PL intensity.

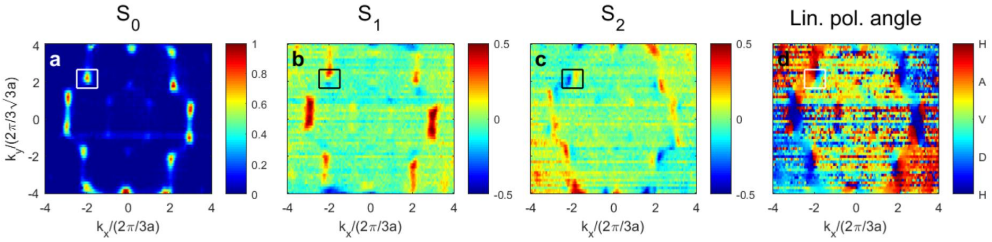

FIG. S7: (a–d) Tomographic images of the momentum space emission at the energy of the Dirac points in the p bands, showing the Stokes parameters S_0 (a), S_1 (b) and S_2 (c), along with the linear polarization angle ϕ (d).

VI. RESONANT EXCITATION MEASUREMENTS

To resonantly excite specific states in the dispersion relation of our honeycomb lattice we control both the energy and incoming angle of the excitation laser. The excitation energy and k vector corresponding to the results shown in Fig. 3 and 4 of the main text are shown in relation to the band structure by black markers in Fig. S8. The three lower energy points correspond to s band excitation [Fig. 3] and the two upper energy points correspond to p band excitation [Fig. 4]. The Γ, K and K' points are excited with angles of 0°, +6.7° and −6.7° respectively.

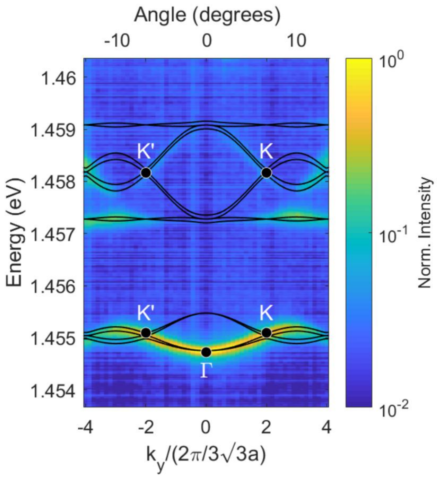

FIG. S8: Dispersion relation measured under low-power non-resonant excitation along $k_x = 0$ ($K' - \Gamma - K$ direction). The black dots show the excitation energy and k vector corresponding to the results shown in Figs. 3 and 4 of the main text. The solid curves show the band structure calculated using the developed tight binding models.

Examples of the real space emission, corresponding to Fig. 3 of the main text (for H polarization) are shown in Fig. S9, which shows the total intensity ($S_0 = I_{\sigma+} + I_{\sigma-}$) overlaid with outlines of the experimental structure. The black cross marks the position of the pump spot.

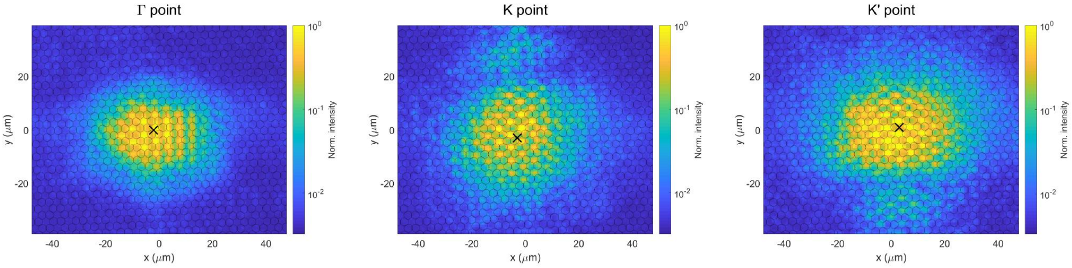

FIG. S9: Measured real space total intensity S_0 under resonant s band excitation for a horizontally polarized pump.

---

[1] C. Leyder, M. Romanelli, J. Ph Karr, E. Giacobino, T. C. H. Liew, M. M. Glazov, A. V. Kavokin, G. Malpuech, and A. Bramati. Observation of the optical spin hall effect. *Nature Physics*, 3:628, 2007.

Chapter 6

Summary and Outlook

6.1 Summary

This thesis has explored effects in single and coupled micropillar devices.

In chapter 3 stimulated scattering into the idler mode was observed in a square micropillar device, when a seeding pulse was used in the signal mode. A Hanbury-Brown and Twiss interferometer was used to analyse the central pump mode (E_{12}) emission. Several improvements can be made; firstly, using a circularly polarised pump laser on the E_{12} mode will increase the interaction strength compared to a linear input, second, better temperature control on the sample would allow for larger mode spacings to be used, meaning a stronger signal (E_{11}) excitation could be used, finally, using a device with more QWs which has been shown in literature to produce more efficient parametric scattering.

In chapter 4, a nonlinear polarisation rotation on the E_{12} mode was observed on two square micropillar devices. The mechanism responsible for this is XPM between the E_{12} signal and E_{11} control mode. Two experiments showed how the control population can modify the polarisation of the signal, with the size of the polarisation rotation influenced by the; polariton exciton fractions, linewidths and control polariton number. The fibre cavity system has the potential to produce phase shifts two orders of magnitude larger, given the parameters discussed. For polaritonic devices the ability to inject a nonlinearity at the single polariton level is a crucial element for many QIP protocols. The QW polariton scheme balances scalability and interaction strength for many applications.

In chapter 5 using polariton graphene, we were able to demonstrate the emergence of a TE-TM field that resembles Dresselhaus spin-orbit coupling. The pseudospin of linearly polarised polaritons injected at the $\mathbf{K}$-$\mathbf{K}'$ points, point in opposite directions and is revealed through the real-space images of the OSHE. A future goal of this work is to reproduce the topological insulator in two dimensions, introducing a strong magnetic field to open a topologically protected edge mode in the Dirac points. Another direction could be to use a similar experiment to study nonlinear effects in the lattice. To do this, a sample with a smaller negative detuning and using stronger excitation to see condensation in the S or P band Dirac points and record the polarisation patterns.

6.2 Outlook

6.2.1 Polariton anti-bunched light

In chapter 3 the goal was to exploit the weak nonlinearity present in polariton micropillars to generate anti-bunched light. Other platforms platforms look to use polaritons as a single-photon source. The fibre-cavity system [152] used by Imamoğlu and Volz have produced the best polariton anti-bunching results. These experiments involved red-detuning a laser with respect to the polariton resonance. Both are resonant excitation measurements. As discussed before, QDs have a strong nonlinearity which produces a strong splitting between the bi-exciton and neutral exciton transition. The photons produce anti-bunched light when filtering the PL to allow the neutral exciton only. Using non-resonant excitation, anti-bunched light can be produced in this manner. In the case of polaritons in fibre cavities, the nonlinear energy shift is less than the linewidth. Perhaps a narrow band filter insert in the collection path could allow for correlations to be observed, similar to the resonant excitation case.

6.2.2 CPHASE Gate using exciton-polaritons

In chapter 4, an all-optical phase rotation of a control mode onto a signal mode was demonstrated in a single polariton micropillar. The experimental results show a phase shift in the E_{12} mode due to a cross-Kerr effect introduced by the presence of the E_{11} mode. This kind of result is analogous is a conditional quantum operation in quantum information processing. It was shown that cascaded systems where the nonlinearity is distributed between several cavities could overcome mode entanglement in the frequency domain[132, 153]. The controlled phase (CPHASE) gate operates in a 2 (or greater) qubit system where a control qubit acts on a target qubit introducing a rotation of π. A basic schematic is shown below in figure 6.1 with the transformation matrix S.

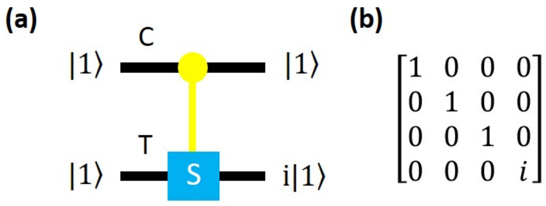

$$\begin{bmatrix} 1 & 0 & 0 & 0 \\ 0 & 1 & 0 & 0 \\ 0 & 0 & 1 & 0 \\ 0 & 0 & 0 & i \end{bmatrix}$$

Figure 6.1: Schematic of a two qubit CPHASE gate. a) 'C' is the control qubit, 'T' the target qubit and S the transformation matrix. b) The transformation matrix S.

Polariton micropillars can be arranged in geometries with high precision [4]. With the demonstration of a single micropillar phase shift, the natural progression is to move to coupled devices. The details for cascading several emitters can be found in the supplementary of Kuriakose et al. [2]. Achieving conditional phase shift at a single photon level in a scalable micropillar system is a stepping stone to quantum phase gates.

6.2.3 Phase Shift in fiber cavity

In chapter 4, the phase shift in our system is limited by the linewidth of E_{12} and exciton fractions $|X_{11}|^2 \times |X_{12}|^2$. Another factor is the micropillar's transverse mode area. We anticipate that in a system such as in reference [31], a high-quality fiber microcavity will produce much larger phase shifts of ∼320mrad. They observed weak photon anti-bunching using polaritons, yielding a value of $g^2_{exp}(0)$ =0.95. The ratio of single polariton interaction energy compared to the linewidth U_{pp}/γ =0.088. With some minor adaptations made, using interactions between co-circularly polarised polaritons instead of linear states, the relative interaction strength is given by:

$$\frac{g_{XX,circ}}{g_{XX,lin}} = 2\frac{g_1 - g_2}{g_1 + g_2} \tag{6.1}$$

where g_1 is the co-circular and g_2 is the cross-circular polariton interaction strengths. Using the assumption of $g_2 = -0.1g_1$ [32], $\frac{g_{XX,circ}}{g_{XX,lin}} \sim 2.44$. Using the quoted linewidth and exciton fraction of $60\mu eV$ and 0.6 respectively for the signal mode. Next given that we require ~1meV separation between signal and control mode, the control mode will have an estimated 0.34 exciton fraction. We can expect a XPM phase shift $2U_{pp}/(\gamma/2) = 320$mrad, two orders of magnitude larger than our 3mrad per particle phase shift. With the differences being a smaller modal area, higher exciton fractions and smaller linewidths [2].

Bibliography

1. Kyriienko, O. & Liew, T. C. H. Triggered single-photon emitters based on stimulated parametric scattering in weakly nonlinear systems. *Phys. Rev. A* **90,** 063805. `https://link.aps.org/doi/10.1103/PhysRevA.90.063805` (6 Dec. 2014).
2. Kuriakose, T. *et al.* Few-photon all-optical phase rotation in a quantum-well micropillar cavity. *Nature Photonics,* 1–4 (2022).
3. Nalitov, A., Malpuech, G., Terças, H. & Solnyshkov, D. Spin-orbit coupling and the optical spin hall effect in photonic graphene. *Physical review letters* **114,** 026803 (2015).
4. Whittaker, C. *et al.* Optical analogue of Dresselhaus spin–orbit interaction in photonic graphene. *Nature Photonics* **15,** 193–196 (2021).
5. Kittel, C. *Introduction to Solid State Physics* ISBN: 9780471415268. `https://books.google.co.uk/books?id=kym4QgAACAAJ` (Wiley, 2004).
6. Fox, M. & Ispasoiu, R. in *Springer Handbook of Electronic and Photonic Materials* (eds Kasap, S. & Capper, P.) 1 (Springer International Publishing, 2017). ISBN: 978-3-319-48933-9. `https://doi.org/10.1007/978-3-319-48933-9%7B%5C_%7D40`.
7. Masselink, W. T. *et al.* Absorption coefficients and exciton oscillator strengths in AlGaAs-GaAs superlattices. *Phys. Rev. B* **32,** 8027–8034. `https://link.aps.org/doi/10.1103/PhysRevB.32.8027` (12 Dec. 1985).

8. Shinada, M. & Sugano, S. Interband optical transitions in extremely anisotropic semiconductors. I. Bound and unbound exciton absorption. *Journal of the Physical Society of Japan* **21,** 1936–1946 (1966).

9. Kavokin, A., Baumberg, J. J., Malpuech, G. & Laussy, F. P. *Microcavities* ISBN: 0199228949 (Oxford University Press, Inc., USA, 2008).

10. Liu, F. *et al.* High Purcell factor generation of indistinguishable on-chip single photons. *Nature nanotechnology* **13,** 835–840 (2018).

11. Krauss, T. F. Why do we need slow light? *Nature photonics* **2,** 448–450 (2008).

12. Weisbuch, C., Nishioka, M., Ishikawa, A. & Arakawa, Y. Observation of the coupled exciton-photon mode splitting in a semiconductor quantum microcavity. *Phys. Rev. Lett.* **69,** 3314–3317. `https://link.aps.org/doi/10.1103/PhysRevLett.69.3314` (23 Dec. 1992).

13. Houdré, R. *et al.* Measurement of Cavity-Polariton Dispersion Curve from Angle-Resolved Photoluminescence Experiments. *Phys. Rev. Lett.* **73,** 2043–2046. `https://link.aps.org/doi/10.1103/PhysRevLett.73.2043` (15 Oct. 1994).

14. Savona, V., Quattropani, A., Andreani, L. C. & Schwendimann, P. *Quantum well excitons in semiconductor microcavities: uniied treatment of weak and strong coupling regimes* tech. rep. (1997).

15. Malpuech, G. *et al.* Room-temperature polariton lasers based on GaN microcavities. *Applied physics letters* **81,** 412–414 (2002).

16. Antoine-Vincent, N. *et al.* Observation of Rabi splitting in a bulk GaN microcavity grown on silicon. *Phys. Rev. B* **68,** 153313. `https://link.aps.org/doi/10.1103/PhysRevB.68.153313` (15 Oct. 2003).

17. Christopoulos, S. *et al.* Room-temperature polariton lasing in semiconductor microcavities. *Physical review letters* **98,** 126405 (2007).

18. Bhattacharya, P. *et al.* Room temperature electrically injected polariton laser. *Physical review letters* **112,** 236802 (2014).
19. Schneider, C., Glazov, M. M., Korn, T., Höfling, S. & Urbaszek, B. Two-dimensional semiconductors in the regime of strong light-matter coupling. *Nature communications* **9,** 1–9 (2018).
20. Mak, K. F., Lee, C., Hone, J., Shan, J. & Heinz, T. F. Atomically thin MoS 2: a new direct-gap semiconductor. *Physical review letters* **105,** 136805 (2010).
21. Emmanuele, R. *et al.* Highly nonlinear trion-polaritons in a monolayer semiconductor. *Nature communications* **11,** 1–7 (2020).
22. Lidzey, D. G. *et al.* Strong exciton–photon coupling in an organic semiconductor microcavity. *Nature* **395,** 53–55 (1998).
23. Zambon, N. C. *et al.* Parametric instability in coupled nonlinear microcavities. *Physical Review A* **102,** 023526 (2020).
24. Kéna-Cohen, S. & Forrest, S. Room-temperature polariton lasing in an organic single-crystal microcavity. *Nature Photonics* **4,** 371 (2010).
25. Zasedatelev, A. V. *et al.* A room-temperature organic polariton transistor. *Nature Photonics* **13,** 378–383 (2019).
26. Kasprzak, J. *et al.* Bose–Einstein condensation of exciton polaritons. *Nature* **443,** 409–414 (2006).
27. Amo, A. *et al.* Superfluidity of polaritons in semiconductor microcavities. *Nature Physics* **5,** 805–810 (2009).
28. Sich, M. *et al.* Observation of bright polariton solitons in a semiconductor microcavity. *Nature photonics* **6,** 50–55 (2012).
29. St-Jean, P. *et al.* Lasing in topological edge states of a one-dimensional lattice. *Nature Photonics* **11,** 651–656 (2017).

30. Klembt, S. *et al.* Exciton-polariton topological insulator. *Nature* **562,** 552–556 (2018).
31. Delteil, A. *et al.* Towards polariton blockade of confined exciton–polaritons. *Nature materials* **18,** 219–222 (2019).
32. Renucci, P. *et al.* Microcavity polariton spin quantum beats without a magnetic field: A manifestation of Coulomb exchange in dense and polarized polariton systems. *Physical Review B* **72,** 075317 (2005).
33. Ciuti, C., Savona, V., Piermarocchi, C., Quattropani, A. & Schwendimann, P. Role of the exchange of carriers in elastic exciton-exciton scattering in quantum wells. *Phys. Rev. B* **58,** 7926–7933. `https://link.aps.org/doi/10.1103/PhysRevB.58.7926` (12 Sept. 1998).
34. Tassone, F. & Yamamoto, Y. Exciton-exciton scattering dynamics in a semiconductor microcavity and stimulated scattering into polaritons. *Phys. Rev. B* **59,** 10830–10842. `https://link.aps.org/doi/10.1103/PhysRevB.59.10830` (16 Apr. 1999).
35. Estrecho, E. *et al.* Direct measurement of polariton-polariton interaction strength in the Thomas-Fermi regime of exciton-polariton condensation. *Physical Review B* **100,** 035306 (2019).
36. Sun, Y. *et al.* Direct measurement of polariton–polariton interaction strength. *Nature Physics* **13,** 870–875 (2017).
37. Munkhbat, B. *et al.* Transition metal dichalcogenide metamaterials with atomic precision. *Nature communications* **11,** 1–8 (2020).
38. Vladimirova, M. *et al.* Polariton-polariton interaction constants in microcavities. *Physical Review B* **82,** 075301 (2010).
39. Tartakovskii, A. *et al.* Nonlinearities in emission from the lower polariton branch of semiconductor microcavities. *Physical Review B* **60,** R11293 (1999).

40. Muñoz-Matutano, G. *et al.* Emergence of quantum correlations from interacting fibre-cavity polaritons. *Nature materials* **18,** 213–218 (2019).
41. Stevenson, R. *et al.* Continuous wave observation of massive polariton redistribution by stimulated scattering in semiconductor microcavities. *Physical Review Letters* **85,** 3680 (2000).
42. Savvidis, P. *et al.* Angle-resonant stimulated polariton amplifier. *Physical review letters* **84,** 1547 (2000).
43. Carusotto, I. & Ciuti, C. Spontaneous microcavity-polariton coherence across the parametric threshold: Quantum Monte Carlo studies. *Physical Review B* **72,** 125335 (2005).
44. Krizhanovskii, D. *et al.* Dominant effect of polariton-polariton interactions on the coherence of the microcavity optical parametric oscillator. *Physical review letters* **97,** 097402 (2006).
45. Krizhanovskii, D. *et al.* Self-organization of multiple polariton-polariton scattering in semiconductor microcavities. *Physical Review B* **77,** 115336 (2008).
46. Tredicucci, A., Chen, Y., Pellegrini, V., Börger, M. & Bassani, F. Optical bistability of semiconductor microcavities in the strong-coupling regime. *Physical Review A* **54,** 3493 (1996).
47. Baas, A., Karr, J. P., Eleuch, H. & Giacobino, E. Optical bistability in semiconductor microcavities. *Physical Review A* **69,** 023809 (2004).
48. Peyghambarian, N. & Gibbs, H. Optical bistability for optical signal processing and computing. *Optical Engineering* **24,** 68–73 (1985).
49. Ballarini, D. *et al.* All-optical polariton transistor. *Nature communications* **4,** 1–8 (2013).
50. Panzarini, G. *et al.* Cavity-polariton dispersion and polarization splitting in single and coupled semiconductor microcavities. *Physics of the Solid State* **41,** 1223–1238 (1999).

51. Solnyshkov, D. & Malpuech, G. Chirality in photonic systems. *Comptes Rendus Physique* **17,** 920–933 (2016).

52. Leyder, C. *et al.* Observation of the optical spin Hall effect. *Nature Physics* **3,** 628–631 (2007).

53. Wertz, E. *et al.* Spontaneous formation and optical manipulation of extended polariton condensates. *Nature physics* **6,** 860–864 (2010).

54. Tassone, F., Piermarocchi, C., Savona, V., Quattropani, A. & Schwendimann, P. Bottleneck effects in the relaxation and photoluminescence of microcavity polaritons. *Physical Review B* **56,** 7554 (1997).

55. Tartakovskii, A. *et al.* Relaxation bottleneck and its suppression in semiconductor microcavities. *Physical Review B* **62,** R2283 (2000).

56. Anderson, M. H., Ensher, J. R., Matthews, M. R., Wieman, C. E. & Cornell, E. A. Observation of Bose-Einstein condensation in a dilute atomic vapor. *science* **269,** 198–201 (1995).

57. Davis, K. B. *et al.* Bose-Einstein condensation in a gas of sodium atoms. *Physical review letters* **75,** 3969 (1995).

58. Imamog, A., Ram, R., Pau, S., Yamamoto, Y., *et al.* Nonequilibrium condensates and lasers without inversion: Exciton-polariton lasers. *Physical Review A* **53,** 4250 (1996).

59. Deng, H. *et al.* Quantum degenerate exciton-polaritons in thermal equilibrium. *Physical review letters* **97,** 146402 (2006).

60. Lu, T.-C. *et al.* Room temperature polariton lasing vs. photon lasing in a ZnO-based hybrid microcavity. *Optics express* **20,** 5530–5537 (2012).

61. Wertz, E. *et al.* Spontaneous formation of a polariton condensate in a planar GaAs microcavity. *Applied Physics Letters* **95,** 051108 (2009).

62. Kasprzak, J., Solnyshkov, D. D., André, R., Dang, L. S. & Malpuech, G. Formation of an Exciton Polariton Condensate: Thermodynamic versus Kinetic Regimes. *Phys. Rev. Lett.* **101,** 146404. `https://link.aps.org/doi/10.1103/PhysRevLett.101.146404` (14 Oct. 2008).

63. Christmann, G., Butté, R., Feltin, E., Carlin, J.-F. & Grandjean, N. Room temperature polariton lasing in a GaN/ AlGaN multiple quantum well microcavity. *Applied Physics Letters* **93,** 051102 (2008).

64. Guillet, T. *et al.* Polariton lasing in a hybrid bulk ZnO microcavity. *Applied Physics Letters* **99,** 161104 (2011).

65. Liew, T., Kavokin, A. & Shelykh, I. Optical circuits based on polariton neurons in semiconductor microcavities. *Physical Review Letters* **101,** 016402 (2008).

66. Kapitza, P. Viscosity of liquid helium below the λ-point. *Nature* **141,** 74–74 (1938).

67. Allen, J. F. & Misener, A. Flow of liquid helium II. *Nature* **141,** 75–75 (1938).

68. Lagoudakis, K. G. *et al.* Quantized vortices in an exciton–polariton condensate. *Nature physics* **4,** 706–710 (2008).

69. Ciuti, C. & Carusotto, I. Quantum fluid effects and parametric instabilities in microcavities. *physica status solidi (b)* **242,** 2224–2245 (2005).

70. Lerario, G. *et al.* Room-temperature superfluidity in a polariton condensate. *Nature Physics* **13,** 837–841 (2017).

71. Ozawa, T. *et al.* Topological photonics. *Reviews of Modern Physics* **91,** 015006 (2019).

72. Klitzing, K. v., Dorda, G. & Pepper, M. New method for high-accuracy determination of the fine-structure constant based on quantized Hall resistance. *Physical review letters* **45,** 494 (1980).

73. Thouless, D. J., Kohmoto, M., Nightingale, M. P. & den Nijs, M. Quantized Hall conductance in a two-dimensional periodic potential. *Physical review letters* **49,** 405 (1982).

74. Klitzing, K. v., Dorda, G. & Pepper, M. New Method for High-Accuracy Determination of the Fine-Structure Constant Based on Quantized Hall Resistance. *Phys. Rev. Lett.* **45,** 494–497. `https://link.aps.org/doi/10.1103/PhysRevLett.45.494` (6 Aug. 1980).

75. Laughlin, R. B. Quantized Hall conductivity in two dimensions. *Physical Review B* **23,** 5632 (1981).

76. Jalali Mehrabad, M. *Integrated topological quantum optics* PhD thesis (University of Sheffield, 2021).

77. Kane, C. L. & Mele, E. J. Quantum spin Hall effect in graphene. *Physical review letters* **95,** 226801 (2005).

78. Kim, M., Jacob, Z. & Rho, J. Recent advances in 2D, 3D and higher-order topological photonics. *Light: Science & Applications* **9,** 1–30 (2020).

79. Jalali Mehrabad, M. *et al.* A semiconductor topological photonic ring resonator. *Applied Physics Letters* **116,** 061102 (2020).

80. Su, W., Schrieffer, J. & Heeger, A. J. Solitons in polyacetylene. *Physical review letters* **42,** 1698 (1979).

81. Abbarchi, M. *et al.* Macroscopic quantum self-trapping and Josephson oscillations of exciton polaritons. *Nature Physics* **9,** 275–279 (2013).

82. Whittaker, C. *et al.* Exciton polaritons in a two-dimensional lieb lattice with spin-orbit coupling. *Physical review letters* **120,** 097401 (2018).

83. Masumoto, N. *et al.* Exciton-polariton condensates with flat bands in a two-dimensional kagome lattice. *New Journal of Physics* **14,** 065002 (2012).

84. Milićević, M. *et al.* Edge states in polariton honeycomb lattices. *2D Materials* **2,** 034012 (2015).

85. Parto, M. *et al.* Edge-Mode Lasing in 1D Topological Active Arrays. *Phys. Rev. Lett.* **120,** 113901. `https://link.aps.org/doi/10.1103/PhysRevLett.120.113901` (11 Mar. 2018).

86. Dikopoltsev, A. *et al.* Topological insulator vertical-cavity laser array. *Science* **373,** 1514–1517 (2021).

87. Bandres, M. A. *et al.* Topological insulator laser: Experiments. *Science* **359** (2018).

88. Gulevich, D. R., Yudin, D., Skryabin, D. V., Iorsh, I. V. & Shelykh, I. A. Exploring nonlinear topological states of matter with exciton-polaritons: Edge solitons in kagome lattice. *Scientific reports* **7,** 1–8 (2017).

89. Li, C. *et al.* Lieb polariton topological insulators. *Physical Review B* **97,** 081103 (2018).

90. He, X.-T. *et al.* A silicon-on-insulator slab for topological valley transport. *Nature communications* **10,** 1–9 (2019).

91. Mehrabad, M. J. *et al.* A chiral topological add-drop filter for integrated quantum photonic circuits. *arXiv preprint arXiv:2110.07277* (2021).

92. Mehrabad, M. J. *et al.* Chiral topological photonics with an embedded quantum emitter. *Optica* **7,** 1690–1696 (2020).

93. Karzig, T., Bardyn, C.-E., Lindner, N. H. & Refael, G. Topological polaritons. *Physical Review X* **5,** 031001 (2015).

94. Imamoḡlu, A., Schmidt, H., Woods, G. & Deutsch, M. Strongly interacting photons in a nonlinear cavity. *Physical Review Letters* **79,** 1467 (1997).

95. Birnbaum, K. M. *et al.* Photon blockade in an optical cavity with one trapped atom. *Nature* **436,** 87–90 (2005).

96. Gerace, D., Laussy, F. & Sanvitto, D. Quantum nonlinearities at the single-particle level. *Nature Materials* **18,** 200–201 (2019).

97. Verger, A., Ciuti, C. & Carusotto, I. Polariton quantum blockade in a photonic dot. *Physical Review B* **73,** 193306 (2006).

98. Walker, P. *et al.* Ultra-low-power hybrid light–matter solitons. *Nature communications* **6,** 1–7 (2015).

99. Liew, T. & Savona, V. Single photons from coupled quantum modes. *Physical review letters* **104,** 183601 (2010).

100. Kimble, H. J., Dagenais, M. & Mandel, L. Photon antibunching in resonance fluorescence. *Physical Review Letters* **39,** 691 (1977).

101. Kuhn, A., Hennrich, M. & Rempe, G. Deterministic single-photon source for distributed quantum networking. *Physical review letters* **89,** 067901 (2002).

102. Aharonovich, I., Englund, D. & Toth, M. Solid-state single-photon emitters. *Nature Photonics* **10,** 631–641 (2016).

103. Howell, J. C., Bennink, R. S., Bentley, S. J. & Boyd, R. W. Realization of the Einstein-Podolsky-Rosen paradox using momentum-and position-entangled photons from spontaneous parametric down conversion. *Physical Review Letters* **92,** 210403 (2004).

104. He, Y.-M. *et al.* Single quantum emitters in monolayer semiconductors. *Nature nanotechnology* **10,** 497–502 (2015).

105. Tran, T. T., Bray, K., Ford, M. J., Toth, M. & Aharonovich, I. Quantum emission from hexagonal boron nitride monolayers. *Nature nanotechnology* **11,** 37–41 (2016).

106. Aharonovich, I. & Neu, E. Diamond nanophotonics. *Advanced Optical Materials* **2,** 911–928 (2014).

107. Santori, C., Pelton, M., Solomon, G., Dale, Y. & Yamamoto, Y. Triggered single photons from a quantum dot. *Physical Review Letters* **86,** 1502 (2001).

108. Müller, M., Bounouar, S., Jöns, K. D., Glässl, M. & Michler, P. On-demand generation of indistinguishable polarization-entangled photon pairs. *Nature Photonics* **8,** 224–228 (2014).

109. Bajoni, D. *et al.* Polariton parametric luminescence in a single micropillar. *Applied Physics Letters* **90,** 051107 (2007).

110. Tartakovskii, A. I. *et al.* Stimulated polariton scattering in semiconductor microcavities: New physics and potential applications. *Advanced Materials* **13,** 1725–1730 (2001).

111. Cerda-Méndez, E. *et al.* Polariton condensation in dynamic acoustic lattices. *Physical review letters* **105,** 116402 (2010).

112. Kim, N. Y. *et al.* GaAs microcavity exciton-polaritons in a trap. *physica status solidi (b)* **245,** 1076–1080 (2008).

113. Lai, C. *et al.* Coherent zero-state and π-state in an exciton–polariton condensate array. *Nature* **450,** 529–532 (2007).

114. Kuther, A. *et al.* Confined optical modes in photonic wires. *Physical Review B* **58,** 15744 (1998).

115. El Daif, O. *et al.* Polariton quantum boxes in semiconductor microcavities. *Applied Physics Letters* **88,** 061105 (2006).

116. Paraso, T. e. a. Enhancement of microcavity polariton relaxation under confinement. *Physical Review B* **79,** 045319 (2009).

117. Gutbrod, T. *et al.* Weak and strong coupling of photons and excitons in photonic dots. *Phys. Rev. B* **57,** 9950–9956. `https://link.aps.org/doi/10.1103/PhysRevB.57.9950` (16 Apr. 1998).

118. Tartakovskii, A. *et al.* Polariton parametric scattering processes in semiconductor microcavities observed in continuous wave experiments. *Physical Review B* **65,** 081308 (2002).

119. Whittaker, C. *et al.* Polariton pattern formation and photon statistics of the associated emission. *Physical Review X* **7,** 031033 (2017).

120. Schwendimann, P. & Quattropani, A. Statistics of the polariton condensate. *Phys. Rev. B* **77,** 085317. `https://link.aps.org/doi/10.1103/PhysRevB.77.085317` (8 Feb. 2008).

121. Romanelli, M., Leyder, C., Karr, J. P., Giacobino, E. & Bramati, A. Four wave mixing oscillation in a semiconductor microcavity: generation of two correlated polariton populations. *Physical review letters* **98,** 106401 (2007).

122. Gisin, N., Ribordy, G., Tittel, W. & Zbinden, H. Quantum cryptography. *Rev. Mod. Phys.* **74,** 145–195. `https://link.aps.org/doi/10.1103/RevModPhys.74.145` (1 Mar. 2002).

123. Kwiat, P., Mattle, K., Weinfurter, H. & Zeilinger, A. AV Sergienko, and Y. Shih. *Phys. Rev. Lett* **75,** 4337 (1995).

124. Monroe, C. Quantum information processing with atoms and photons. *Nature* **416,** 238–246 (2002).

125. Stolen, R. H. & Lin, C. Self-phase-modulation in silica optical fibers. *Physical Review A* **17,** 1448 (1978).

126. Islam, M. N., Mollenauer, L. F., Stolen, R. H., Simpson, J. R. & Shang, H.-T. Cross-phase modulation in optical fibers. *Optics letters* **12,** 625–627 (1987).

127. Vitali, D., Fortunato, M. & Tombesi, P. Complete quantum teleportation with a Kerr nonlinearity. *Physical review letters* **85,** 445 (2000).

128. Brod, D. J., Combes, J. & Gea-Banacloche, J. Two photons co-and counterpropagating through N cross-Kerr sites. *Physical Review A* **94,** 023833 (2016).

129. Firstenberg, O. *et al.* Attractive photons in a quantum nonlinear medium. *Nature* **502,** 71–75 (2013).

130. Tiarks, D., Schmidt-Eberle, S., Stolz, T., Rempe, G. & Dürr, S. A photon–photon quantum gate based on Rydberg interactions. *Nature Physics* **15,** 124–126 (2019).

131. Fushman, I. *et al.* Controlled phase shifts with a single quantum dot. *science* **320,** 769–772 (2008).

132. Shapiro, J. H. Single-photon Kerr nonlinearities do not help quantum computation. *Phys. Rev. A* **73,** 062305. `https://link.aps.org/doi/10.1103/PhysRevA.73.062305` (6 June 2006).

133. Gea-Banacloche, J. Impossibility of large phase shifts via the giant Kerr effect with single-photon wave packets. *Phys. Rev. A* **81,** 043823. `https://link.aps.org/doi/10.1103/PhysRevA.81.043823` (4 Apr. 2010).

134. Munro, W. J., Nemoto, K. & Spiller, T. P. Weak nonlinearities: a new route to optical quantum computation. *New Journal of Physics* **7,** 137 (2005).

135. Heuck, M., Jacobs, K. & Englund, D. R. Controlled-phase gate using dynamically coupled cavities and optical nonlinearities. *Physical review letters* **124,** 160501 (2020).

136. Feizpour, A., Hallaji, M., Dmochowski, G. & Steinberg, A. M. Observation of the nonlinear phase shift due to single post-selected photons. *Nature Physics* **11,** 905–909 (2015).

137. Turchette, Q. A., Hood, C. J., Lange, W., Mabuchi, H. & Kimble, H. J. Measurement of conditional phase shifts for quantum logic. *Physical Review Letters* **75,** 4710 (1995).

138. Venkataraman, V., Saha, K. & Gaeta, A. L. Phase modulation at the few-photon level for weak-nonlinearity-based quantum computing. *Nature Photonics* **7,** 138–141 (2013).

139. Hickman, G., Pittman, T. & Franson, J. Low-power cross-phase modulation in a metastable xenon-filled cavity for quantum-information applications. *Physical Review A* **92,** 053808 (2015).

140. Matsuda, N., Shimizu, R., Mitsumori, Y., Kosaka, H. & Edamatsu, K. Observation of optical-fibre Kerr nonlinearity at the single-photon level. *Nature photonics* **3,** 95–98 (2009).

141. Walker, P. *et al.* Dark solitons in high velocity waveguide polariton fluids. *Physical Review Letters* **119,** 097403 (2017).

142. Whittaker, D. Classical treatment of parametric processes in a strong-coupling planar microcavity. *Physical Review B* **63,** 193305 (2001).

143. Rosenberg, I. *et al.* Strongly interacting dipolar-polaritons. *Science advances* **4,** eaat8880 (2018).

144. Sekretenko, A., Gavrilov, S. & Kulakovskii, V. Polariton-polariton interactions in microcavities under a resonant 10 to 100 picosecond pulse excitation. *Physical Review B* **88,** 195302 (2013).

145. Koralek, J. D. *et al.* Emergence of the persistent spin helix in semiconductor quantum wells. *Nature* **458,** 610–613 (2009).

146. Awschalom, D., Loss, D. & Samarth, N. *Semiconductor spintronics and quantum computation* (Springer Science & Business Media, 2002).

147. Christodoulides, D. N., Lederer, F. & Silberberg, Y. Discretizing light behaviour in linear and nonlinear waveguide lattices. *Nature* **424,** 817–823 (2003).

148. Hafezi, M., Mittal, S., Fan, J., Migdall, A. & Taylor, J. Imaging topological edge states in silicon photonics. *Nature Photonics* **7,** 1001–1005 (2013).

149. Kane, C. L. & Mele, E. Size, shape, and low energy electronic structure of carbon nanotubes. *Physical Review Letters* **78,** 1932 (1997).

150. Rechtsman, M. C. *et al.* Strain-induced pseudomagnetic field and photonic Landau levels in dielectric structures. *Nature Photonics* **7,** 153–158 (2013).

151. Carusotto, I. & Ciuti, C. Quantum fluids of light. *Reviews of Modern Physics* **85,** 299 (2013).

152. Besga, B. *et al.* Polariton boxes in a tunable fiber cavity. *Physical Review Applied* **3,** 014008 (2015).

153. Gea-Banacloche, J. Impossibility of large phase shifts via the giant Kerr effect with single-photon wave packets. *Physical Review A* **81,** 043823 (2010).